PRODUCTION CORRELATIONS OF HADRONICALLY PRODUCED CHARMED PARTICLES

A DISSERTATION

SUBMITTED TO THE DEPARTMENT OF PHYSICS

AND THE COMMITTEE ON GRADUATE STUDIES

OF CARNEGIE MELLON UNIVERSITY

IN PARTIAL FULFILLMENT OF THE REQUIREMENTS

FOR THE DEGREE OF

DOCTOR OF PHILOSOPHY

By

Arne P. Freyberger

August 1990

FERMILAB LIBRARY

Production Correlations of Hadronically Produced Charmed Particles

Abstract

Charm pair production results are presented on the 37 charm pairs collected during the 1985 run of experiment E653 at Fermilab. The pair differential cross section is fitted the functional form $\frac{d\sigma}{dX_f dP_t^2} \sim (1- \mid X_f \mid)^n e^{-bP_t^2}$. The maximum likelihood fit yields n=5.0±1.5 and b=$0.65^{+0.10}_{-0.08}$ $(\mathrm{GeV/c})^{-2}$. The charm pair mass distribution is fitted to an exponential, $e^{-aM(D\bar{D})}$, with a=0.75±0.15 $(\mathrm{GeV/c^2})^{-1}$. The charm pair X_f, P_t^2, rapidity gap, mass and azimuthal opening angle distributions are presented and compared with distributions from previously published results. The azimuthal opening angle and rapidity gap of the charm pair exhibit correlations when compared to charm pairs produced uncorrelated by a Monte Carlo. The P_t^2 distribution has an excess of events at $P_t^2 \gtrsim 3.0$ $(\mathrm{GeV/c})^2$. Comparisons are made to previously published results on Drell-Yan di-lepton production. The data show similarities to the di-lepton results in the pair $<P_t^2>$ and pair mass distributions. The analysis method is described in detail, including the development and performance of a momentum estimator used for the charm parent momentum.

In memory of Mom and Dad ...

Contents

1 Introduction **1**

2 Hadro-Production of Charm: A Review **5**

2.1 Introduction 5

2.2 Theoretical Review 6

2.2.1 Total Charm Cross Section 6

2.2.2 Charm Correlations 9

2.3 Hadronic Charm Production Results to Date 10

2.3.1 Total Charm Cross Section 12

2.3.2 A Dependence 12

2.3.3 Differential Cross Section 13

2.3.4 Charm Pair Results 15

2.4 Drell-Yan Di-Lepton Production 20

2.4.1 Introduction 20

2.4.2 The Drell-Yan – Charm connection 20

2.4.3 Drell-Yan Scaling 22

2.4.4 Structure Functions 24

3 The Hardware **26**

3.1 Introduction 26

3.2 Beam Line 32

3.3 Beam System 32

3.4 Emulsion Target 34

3.4.1 Vertical Emulsion Module 37

3.4.2 Horizontal Emulsion Module 37

3.4.3 Emulsion Alignment 40

3.5 Charged Particle Spectrometer 41

3.5.1 Vertex Silicon Strip Detectors (VSSD's) 41

3.5.2 Analyzing Magnet 42

3.5.3 Spectrometer Drift Chambers 46

3.5.4 Momentum 49

3.6 Muon System 49

3.6.1 Muon Spectrometer 51

3.6.2 The Toroid 53

3.6.3 Muon Hodoscope 54

3.7 The Trigger 55

3.8 Data Acquisition 56

3.8.1 Fastbus Hardware 59

3.9 The 1985 Run and Overall Performance 61

4 Charm Selection **65**

4.1 E653 Trigger 65

4.2 Event Reconstruction and Emulsion Predictions 66

4.3 Emulsion Scanning 69

4.3.1 Automated Scanning 70

4.3.2 Graphic Analysis 72

4.3.3 Decay Search 72

4.3.4 Interaction Background 73

4.4 Emulsion Charm Selection 73

4.4.1 Decay Topologies 74

4.5 Refitting 75

4.6 Final Charm Pair Sample 76

4.6.1 Level 1: A Muonic Vertex 77

4.6.2 Level 2: Two or more decay vertices 77

4.6.3 Level 3: Complete tracking 78

4.6.4 Level 4: M_{min} Cuts 78

4.6.5 Level 5: Multiprong-Multiprong Charm pairs 84

5 Backgrounds **87**

5.1 Introduction 87

5.2 Diffractive Background 88

5.3 Wrong Sign Charged Background 90

5.3.1 Hadronic Kinks (C-1's) 90

5.3.2 Hadronic Tridents (C-3's) 93

5.3.3 Muonic Tridents (C-3μ's) 94

5.4 Wrong charge vertices 95

5.5 Final Background Determination 97

6 Momentum Estimation **98**

6.1 Introduction 98

6.2 Kinematics 99

6.2.1 Mass Assignments 99

6.3 The Resolution Function and Monte Carlo Studies 103

6.4 The 0-C Analogy 106

6.5 Other Charm Decay Modes 108

7 Maximum Likelihood Technique and Efficiencies **119**

7.1 Introduction 119

7.2 Probabilistic Motivation 120

7.2.1 Variable Efficiencies 121

7.2.2 Resolution Functions 121

7.2.3 Maximum Likelihood Implementation in E653 123

7.3 Topological Efficiencies 123

7.3.1 Single Charm Efficiencies 124

7.4 Charm Pair Efficiencies 125

7.5 Validity of the Maximum Likelihood Technique 132

8 Charm Pair Production and Correlation Results **136**

8.1 Introduction 136

8.2 Charm Pair Monte Carlo 137

8.3 Pair X_f Distribution 138

8.4 Pair P_t^2 Distribution 140

8.5 Pair Azimuthal Opening Angle (Φ_t) 142

8.6 Charm Pair Mass 142

8.7 Charm Pair Rapidity Gap (ΔY) 145

8.8 Comparison to previous results 145

9 Conclusions **149**

A The Lund Monte Carlo **153**

B Event listings **160**

List of Tables

1 List of fixed target charm experiments with hadron beams. 11

2 Measured values for α from different fixed target experiments. 13

3 References for the E653 spectrometer and its components. 31

4 Chemical composition of Fuji ET-7B nuclear emulsion. The value for <A> was calculated assuming a linear dependence on A. 36

5 The individual detector resolutions for the E653 spectrometer. 64

6 Listing of the four different classes of cuts used in selecting events for emulsion scanning. 69

7 Typical emulsion scanning predictions for a vertical emulsion module. . . . 70

8 Event through put for the different emulsion scanning stages. 73

9 Allowed range for $M_{\pi\pi}$ of neutral V-2 decays. 84

10 M_{min} cut values for the different topologies. The sigma is the measured error on the M_{min} for the decay. 85

11 Succession of cuts appli d to the charm candidate sample. 85

12 Emulsion-emulsion charm pair topologies in the final charm pair sample. . 86

13 Emulsion-counter charm pair topologies in the final charm pair sample. . . 86

14 The number of non-diffractive vertices with all light shower tracks match to the spectrometer, scaled to yield an estimate of the diffractive background in the complete data set. 88

15 Diffractive background estimates in the complete data set and the charm pair data set at the last two stages of charm pair selection. 89

16 Sign correlations in hadronic kinks with respect to the μ in the event. Right sign kinks had the opposite sign of the muon sign in the event. 94

17 Sign correlation for hadronic tridents (C-3's) with respect to the μ in the event. Right sign tridents have the opposite charge sum of the muon charge in the event. 94

18 Sign correlations for muonic tridents. Right sign means the sign of the muon equals the charge sum of the vertex. 95

19 Wrong charge vertices in the complete data set. 95

20 Wrong charge vertices in the Level 4 charm pairs. 96

21 Wrong charge vertices in the Level 5 charm pairs. 96

22 Total Background for the charm pairs. The diffractive interaction background is lower than measured due to additional emulsion measurements. 97

23 Branching Ratios used in the Monte Carlo development of the momentum estimator and charm selection. 104

24 Comparison of weighted average values measured in two previous charm pair experiments and the values presented in this thesis. 147

25 Event listings for the 37 charm pairs. 163

26 Event listings for the 37 charm pairs continued from the previous page. . . 164

27 Event listings for the 37 charm pairs continued from the previous page. . . 165

28 Event listings for the 37 charm pairs continued from the previous page. . . 166

List of Figures

1 The quark (left) and lepton (right) families and their measured masses[1]. . 2

2 Leading order parton diagrams for heavy quark production. 7

3 Next to leading order parton diagrams for heavy quark production. 8

4 K-factor for the total charm cross section as a function of beam energy. . . 9

5 Total charm cross section measurements from different fixed target charm experiments as a function of center of mass energy. 12

6 The measured values for the exponent n for the different fixed target experiments. 15

7 The measured values for the $<P_t^2>$ from the different fixed target experiments. 16

8 The Φ_t distribution measured by LEBC-PP. There are 107 geometrically reconstructed pairs in the plot. 18

9 The weighted X_f, mass, P_t^2 and ΔY distributions for the 17 LEBC-PP charm pairs. The dashed curve is from the LUND MC with a δ fragmentation function and the solid curve is the LUND MC with LUND fragmentation. . 19

10 Leading order production diagram for di-lepton production in hadronic interactions. 21

11 Plan view of the compact E653 spectrometer. 28

12 The E653 coordinate system. 29

13 The Fermilab accelerator complex with the fix target beam lines. 33

14 The integrated beam spot of the 800 GeV proton beam measured by the beam system. 35

15 The configuration of a vertical emulsion module. 38

16 Horizontal emulsion target module configuration. 39

17 Read out pattern for the vertex silicon strip detectors. 43

18 Residuals in the vertex silicon strip detectors. 44

19 The poles of the analyzing magnet, SCM-104. 45

20 Wiring diagram for the fine and coarse cells in the spectrometer drift chambers. 47

21 Position residuals for the spectrometer drift chambers. 48

22 Plan view of the muon system. 50

23 Position residuals for four of the cells in the muon drift chambers. 52

24 The beam and interactions counters of the E653 trigger system. 57

25 Logical schematic of the E653 trigger. 58

26 The event data path from the the FASTBUS crates to the magnetic tape. 62

27 The integrated number of data triggers written to tape during the 1985 run of E653. 63

28 Cut variables applied the muon track to select events for emulsion scanning. 67

29 Impact paramter for tracks coming from the primary vertex. 71

30 M_{min} distributions for muonic decays of D^o and D^+ mesons. The solid curve is for Monte Carlo and the dashed represents the data before any cuts. The arrows point to the upper and lower bounds on M_{min} required for a decay to be considered charm. 80

31 M_{min} distributions for non-muonic decays of D^o and D^+ mesons. The solid curve is for Monte Carlo and the dashed represents the data before any cuts. The arrows point to the upper and lower bounds on M_{min} required for a decay to be considered charm. 81

32 Wrong sign μ events used to estimate charge background. 91

33 P_t distribution for right sign C-1's found in the emulsion. 92

34 P_t distribution for wrong sign C-1's found in the emulsion. 93

35 Momentum vectors in the laboratory frame for a neutral decay. 100

36 Momentum vectors in the center-of-mass (COM) frame for a neutral decay. Note that the only momentum in the center-of-mass frame in perpendicular to the parent direction in the LAB frame. 100

37 Mass assignments for decays with a tagged muon. 101

38 Mass assignments for decays without a tagged muon. 102

39 The momentum solutions for the 0-C equation as a function of parent mass. 108

40 $P_{min}/P_{generated}$ versus M_{min} for two prong muonic D^o decays. 109

41 $P_{min}/P_{generated}$ projections in $100MeV/c^2$ slices of M_{min} for two prong muonic D^o decays. 110

42 $P_{min}/P_{generated}$ versus M_{min} for two prong hadronic D^o decays. 111

43 $P_{min}/P_{generated}$ projections $100MeV/c^2$ slices of M_{min} for two prong hadronic D^o decays. 112

44 $P_{min}/P_{generated}$ versus M_{min} for three prong muonic D^+ decays. 113

45 $P_{min}/P_{generated}$ projections in $100MeV/c^2$ slices of M_{min} for three prong muonic D^+ decays. 114

46 $P_{min}/P_{generated}$ versus M_{min} for three prong hadronic D^+ decays. 115

47 $P_{min}/P_{generated}$ projections in $100MeV/c^2$ slices of M_{min} for three prong hadronic D^+ decays. 116

48 $P_{min}/P_{generated}$ versus M_{min} for four prong hadronic D^o decays. 117

49 $P_{min}/P_{generated}$ projections in $100MeV/c^2$ slices of M_{min} for four prong hadronic D^o decays. 118

50 Generic resolution function $R(x_i, x_g)$ as function of x_g 122

51 X_f efficiencies for muonic decays in the emulsion block. 126

52 X_f efficiencies for hadronic decays in the emulsion block. 127

53 P_t^2 efficiencies for muonic decays in the emulsion block. 128

54 P_t^2 efficiencies for hadronic decays in the emulsion block. 129

55 Average efficiency as a function of X_f for the 37 charm pairs. 130

56 Average efficiency as a function of P_t^2 for the 37 charm pairs. 131

57 Average efficiency distribution as a function of charm pair mass. 133

58 Average efficiency distribution as a function of charm pair rapidity gap. . . 133

59 Comparison of the input Monte Carlo n value with that returned by the maximum likelihood method for charm pairs. 135

60 Comparison of the input Monte Carlo b value with that returned by the maximum likelihood method for charm pairs. 135

61 The X_f distribution for the 37 charm pairs. The solid line is the result of a maximum likelihood fit to $(1\text{-}X_f)^n$. The dashed histogram is from MC Φ_t correlated charm pairs. 139

62 The weighted P_t^2 distribution for the charm pairs. The solid line is the result of a maximum likelihood fit to $e^{-bP_t^2}$. The dashed histogram is for Φ_t correlated charm pairs. 141

63 The $<P_t^2>$ versus s for E653 and LEBC-PP charm pairs. The curve is a least squares fit to $<P_t^2> = k_t^2 + s\cdot\text{constant}$. 141

64 Φ_t (Azimuthal opening angle of the charm pair) distribution for the 37 charm pairs. 143

65 Charm pair mass distribution. The solid line is the result of a fit to e^{-aM}. The dotted histogram is the mass distribution obtained from the Φ_t correlated MC. 144

66 The rapidity gap distribution of the charm pairs. The solid histogram is for the data. The dashed histogram is for Φ_t correlated MC charm pairs. 146

67 The Φ_t distribution for the 37 charm pairs (solid) and the LUND MC (dots). 155

68 The weighted X_f distribution for the 37 charm pairs (solid) and the LUND MC (dots). 156

69 The weighted charm pair mass distribution. Data (solid). LUND MC (dots). 157

70 The weighted rapidity gap distribution for the 37 charm pairs (solid) and that obtained from the LUND MC (dots). 158

71 The weighted $P_t^{2\prime}$ distribution for the 37 charm pairs (solid) and the LUND MC charm pairs (dots). 159

Chapter 1

Introduction

The last decade has seen some remarkable achievements in particle physics. The discovery of the intermediate vector boson, $W^{\pm}$ [1,2], in 1983 unified the electromagnetic and weak forces. This unification continues the tradition of representing what appear to be different interactions by one encompassing interaction. The subsequent discovery of the Z^{O}, partner to the $W^{\pm}$, and the detailed study of its mass and width have restricted the number of lepton families to three [3,4,6,7].

The constituents within the standard model are divided into two distinct groups. Figure 1 depicts the three generations of quarks and leptons. Lepton masses and limits are from [38], d, u, s, c and b quark masses are from [5] and the t quark mass limit is from [8]. The Z^{o} mass and width only limit the lepton sector. However, symmetry suggests that the numbers of lepton and quark generations are the same. The discovery of the tau neutrino and top quark would complete the constituents needed within the standard model framework. Exhaustive searches at $p\bar{p}$ colliders have yielded no clear evidence for the top quark.

$$\begin{pmatrix} u & c & t \\ (\sim 0.350) & (\sim 1.5) & (> 77) \\ d & s & b \\ (\sim 0.350) & (\sim 0.55) & (\sim 4.5) \end{pmatrix} \begin{pmatrix} e & \mu & \tau \\ (0.000511) & (0.1056) & (1.870) \\ \nu_e & \nu_\mu & \nu_\tau \\ (< 18ev) & (< 0.25MeV) & (< 35MeV) \end{pmatrix}$$

Figure 1: The quark (left) and lepton (right) families and their measured masses[1].

If it exists its mass must be greater than 77 GeV/c^2 [8].

The quarks interact via the strong, electroweak and gravitational forces. The leptons interact via the electroweak and gravitational forces. The strong force is described by the theory of quantum chromodynamics (QCD). QCD is an extension of the highly successful theory of the electromagnetic force, quantum electrodynamics (QED), to the strong force. The electric field of QED is analogous to the color field of QCD, with the photon mediator of QED replaced by the mediator of the strong force, the gluon. QED has been tested to less than one part per billion by studying the electron magnetic moment. QCD has not undergone such strenuous testing. One of the processes described by QCD is heavy quark (charm,bottom or top) production in hadronic interactions.

The study of charm production provides a test of QCD and aids in understanding bottom and top production within the QCD framework. QCD calculations of charm production have been restricted by the questionable validity of the perturbation expansion of the calculation. Experimental results of charm production provide crucial information linking the

[1]Charge conjugate particles are implied throughout this thesis, unless stated otherwise.

perturbative regime of QCD to the non-perturbative regime.

As the search for the top quark intensifies, the understanding of heavy quark production becomes important. Charm and bottom decays contribute background leptons to the top signal and this background must be accurately subtracted in order to reveal new signals. Knowledge of the production characteristics, kinematic and dynamic, of the top quark will aid in its discovery.

Fermilab experiment E653 was proposed in 1981 [63] to study the production and decay properties of particles containing heavy quarks (c, b). E653 used an 800 GeV proton beam incident on an emulsion target followed by 18 planes of 50μ pitch silicon strip detectors. This unique combination of a high resolution electronic spectrometer and the even higher resolution of the target emulsion provided E653 with a large acceptance for charm and beauty pairs. The visual technique of the emulsion allowed charm decays to be identified topologically with a low background. This topological identification in addition to a momentum estimate of the parent charm momentum allowed inclusive production studies of single charm and charm pair distributions to be performed.

The goal of this thesis is present a complete analysis on the production properties of 37 charm pair events. The charm pairs were collected during the 1985 run of experiment E653 at the Fermi National Accelerator Laboratory (Fermilab).

Chapter Two of this thesis will briefly review the current theoretical status of charm production, followed by a review of the experimental measurements. The apparatus and its performance will be described in Chapter Three. The process of selecting charm, with minimal particle identification, will be discussed in Chapter Four. Chapter Five will present

the background determinations. Chapter Six will describe the momentum estimator used in E653 production analysis and Chapter Seven will incorporate the momentum estimator into the Maximum Likelihood Fitting procedure used in this analysis. The final results are presented in Chapter Eight; followed by some concluding remarks in Chapter Nine.

Chapter 2

Hadro-Production of Charm: A Review

2.1 Introduction

Theoretical and experimental results on hadro-production of charmed particles have been converging on the same parton description of the fundamental interaction responsible for heavy quark production in hadronic interactions. This chapter will present a brief review of the theoretical aspects of heavy quark production with an emphasis on charmed particles. Following the theory will be a review of previous fixed target charm production results with an emphasis on charm pair results. More extensive reviews of heavy quark production, with an emphasis on charm production, can be found elsewhere [39,40,41].

2.2 Theoretical Review

2.2.1 Total Charm Cross Section

Heavy quarks produced in hadronic collisions are created by an interaction between the partons inside the interacting hadrons. The heavy quark cross section is modeled within the parton framework and is written as follows:

$$\sigma(P_1, P_2) = \sum_{ij} \int dx_i dx_j \sigma_{ij}(\alpha_s(\mu), x_1 P_1, x_2 P_2) f_i(x_1, \mu) f_j(x_2, \mu) \tag{1}$$

where σ_{ij} represents the parton cross section and $f_j(x_1, \mu)$ represents the probability distribution of the jth parton at momentum fraction x_1. By using the factorization theorem unwanted singularities can be "factored" away [11]. The short order cross section is calculated through a perturbative expansion of σ_{ij} in powers of $\alpha_s(\mu)$. Nason, Dawson and Ellis [9] have used this method to calculate the charm cross section. The calculation was carried out to the next to leading order ($\alpha_s^3(\mu)$). The leading order parton level diagrams are shown in Figure 2 and the next to leading order diagrams are shown in Figure 3. Berger has compared the next to leading order cross section to the leading order cross section by defining the K factor as [13]:

$$K = \frac{\sigma(\alpha_s^2(\mu) + \alpha_s^3(\mu))}{\sigma(\alpha_s^2(\mu)).} \tag{2}$$

The graph obtained from this calculation is shown in Figure 4. Previous leading order calculations had returned charm cross sections that were consistently lower than the measured values. This next to leading order calculation yields total cross section values that

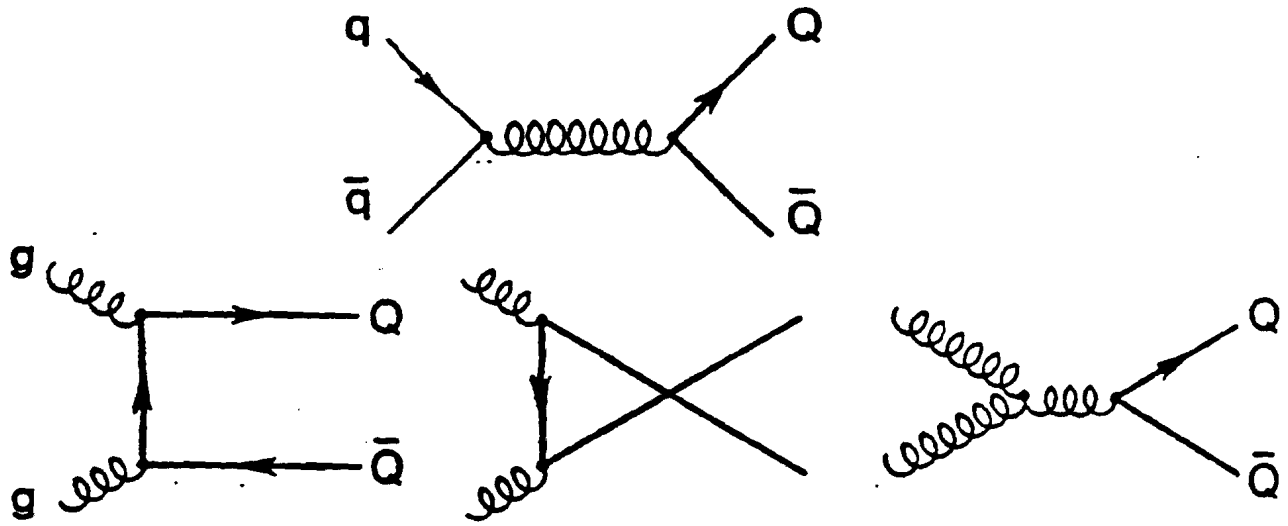

Figure 2: Leading order parton diagrams for heavy quark production.

are consistent with the measured cross sections without invoking a low charm quark mass or intrinsic charm component of the hadrons. Charm cross sections calculated through leading order diagrams required a very low charm mass or an intrinsic charm component in the incident hadrons.

The fact that the next to leading order diagram contribute heavily to the total cross section came as a surprise. However, Nason, Dawson and Ellis showed that some of the next to leading order diagrams can contribute to the cross section at the same level as leading order diagrams. For example the cross section for $gg \rightarrow gg$ is approximately two orders of magnitude greater than the cross section for $gg \rightarrow q\bar{q}$. This $gg \rightarrow gg$ process produces a heavy quark pair through gluon splitting (Figure 3c).

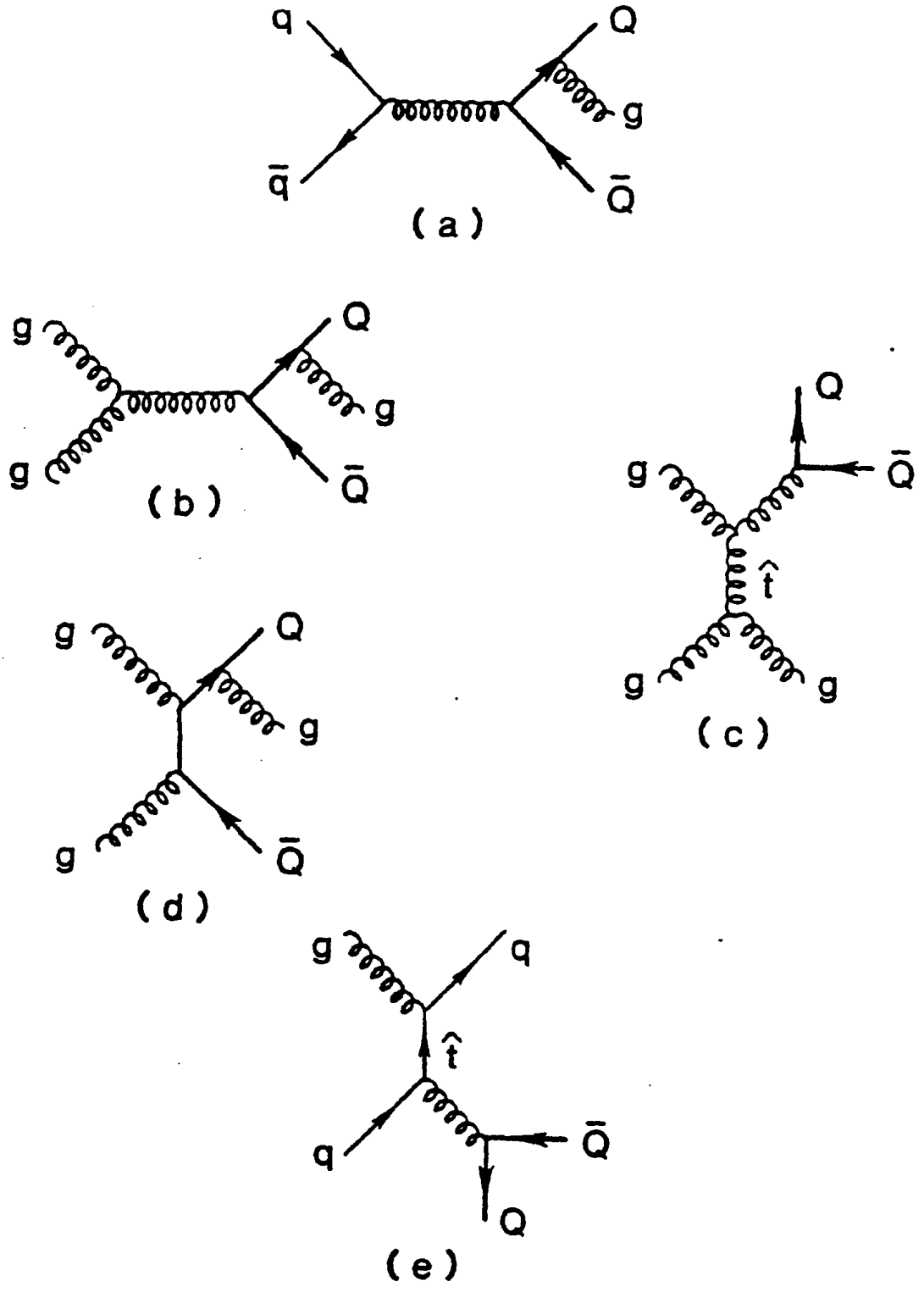

Figure 3: Next to leading order parton diagrams for heavy quark production.

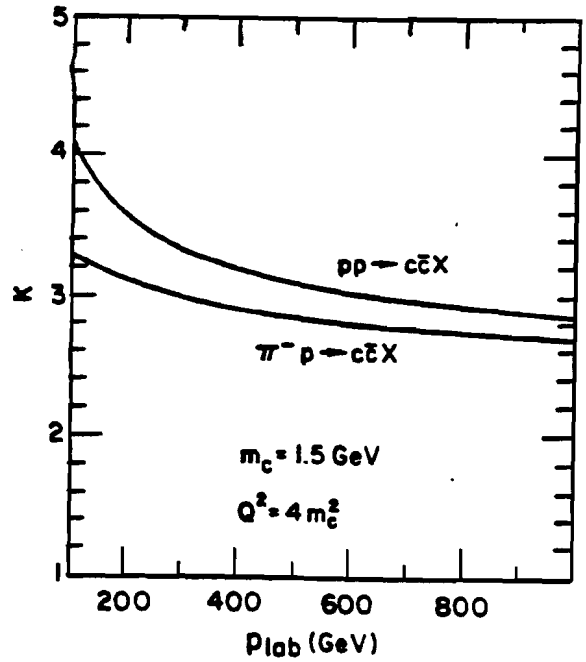

Figure 4: K-factor for the total charm cross section as a function of beam energy.

2.2.2 Charm Correlations

The cross section calculation provides a fundamental check of the theoretical basis of the parton model. In addition to the cross section there have also been predictions involving correlations between the q and $\bar{q}$ produced in the interaction. Berger has shown that for quarks at least as massive of the beauty quark the rapidity gap [1] (ΔY) of the quark pair has two distinct distributions depending on which diagram is contributing to the cross section [12]. For $q\bar{q} \rightarrow Q\bar{Q}$ the rapidity gap, ($|\Delta Y|$), should be very small (full width at half maximum 1.3 for $|\Delta Y|$). whereas for $gg \rightarrow Q\bar{Q}$ will be broad (full width at half maximum of 3.0). Although these predictions are for beauty quarks they point out that the rapidity gap reflects the parton process responsible for heavy quark production. The

[1] Definition of rapidity is: $y = \frac{1}{2}\ln\frac{E+p_z}{E-p_z}$ and rapidity gap in the charm pair system is defined as: $\Delta Y = |y_{\bar{D}} - y_D|$.

differential heavy quark pair cross section was also shown to depend only on ΔY and not on the individual heavy quark rapidities, y_b or $y_{\bar{b}}$.

Another important charm pair variable is the square of the average charm pair momentum perpendicular to the beam direction, $< P_t^2 >$ [11]. Collins, Soper and Sterman predict that the measured value of $< P_t^2 >$ for charm pairs should be the same as that measured in Drell-Yan di-lepton production at the equivalent di-lepton mass. It would also be interesting to see if the same type of $< P_t^2 >$ scaling that occurs in Drell-Yan production holds for charm pairs. The average P_t^2 scaling seen in Drell-Yan di-lepton production is:

$$< P_t^2 >= k_t^2 + s \cdot constant \tag{3}$$

The k_t^2 is a measure of the intrinsic transverse momentum of the partons involved in the process. Thus as Drell-Yan di-lepton production analysis was able to measure the intrinsic transverse momentum of the quarks involved in di-lepton production, charm pair $< P_t^2 >$ will reflect the intrinsic transverse momentum of the gluons responsible for charm production.

2.3 Hadronic Charm Production Results to Date

Hadronic charm production experiments have been done with different beam and target particles, at different center of mass energies, and with different experimental techniques. This review will concentrate on fixed target hadro production charm experiments that have vertex resolution capabilities necessary to reconstruct charm decays. Table 1 lists the

Experiment	Beam Momentum (GeV/c)	Beam Particle	Target Particle	Vertex Detector
NA-32	200	π^-,K,P	Si	CCD's and silicon strips
E769	250	π^-,K,P	Be,Al,Cu,W	Silicon strips
WA-82	340	π^-	Si,W	Silicon Strips
NA-27	360	π^-	Proton	Bubble Chamber
NA-27	400	Proton	Proton	Bubble Chamber
E743	800	Proton	Proton	Bubble Chamber
E653	800	Proton	Emulsion	Emulsion and silicon strips

Table 1: List of fixed target charm experiments with hadron beams.

experiments in this review.

There are two experimental techniques used to obtain a sample of charm particles for production studies:

- Bubble chamber and nuclear emulsion experiments where the event topology can be determined through visual methods [36,49,50,53].
- High resolution silicon strip detectors that have sufficient resolution to reconstruct the decay vertices [36,47,46].

The visual technique of the bubble chamber and emulsion yield small samples of charm decays with low backgrounds. The electronic experiments obtain large samples of charm decays with large combinatoric backgrounds that must be properly subtracted.

The production results from these experiments can be divided into four measurements, total charm cross section measurements, nuclear dependence of the charm cross section, differential cross section distributions and charm pair distributions. The current status of these four measurements is presented in the following sections.

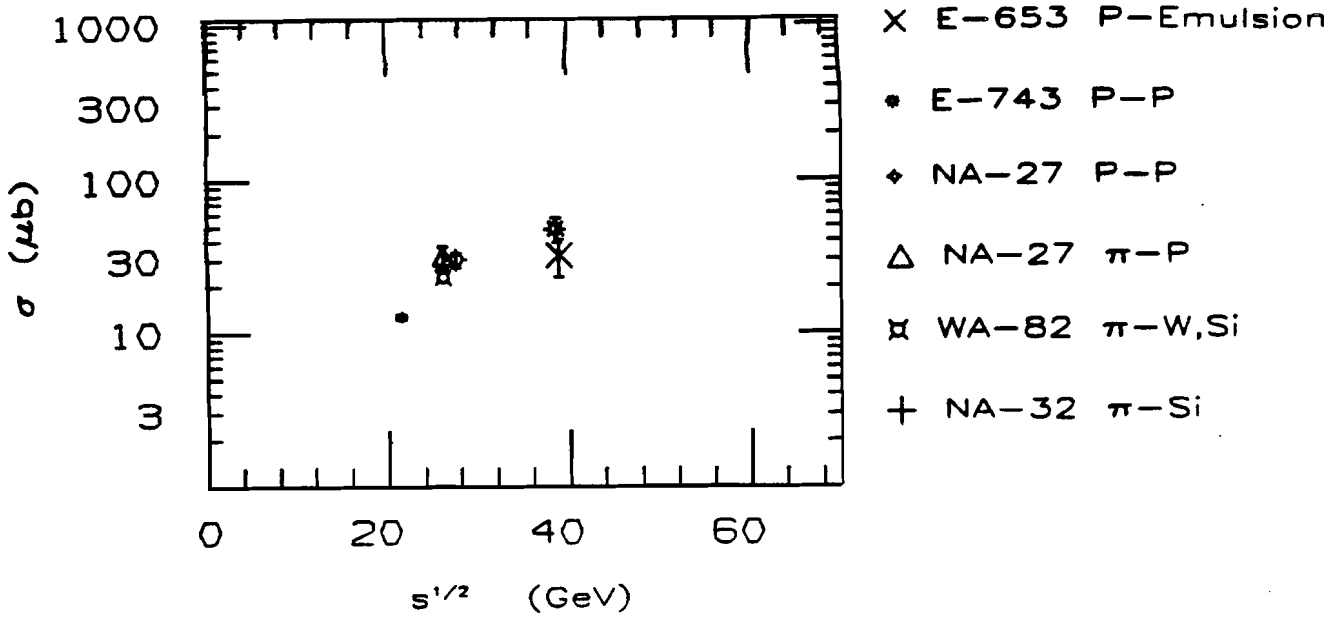

Figure 5: Total charm cross section measurements from different fixed target charm experiments as a function of center of mass energy.

2.3.1 Total Charm Cross Section

Until the theoretical calculation of the total cross section by Nason, Dawson and Ellis [9] the experimental cross sections did not agree with those predicted by the leading order calculations. The measured cross sections are plotted in Figure 5 as a function of the center of mass energy ($\sqrt{s}$) [35,47,49,50,53,58]. Cross sections for non-hydrogen targets were calculated assuming a linear A dependence of the cross section (see Section 2.3.2). The rise of the charm cross section with $\sqrt{s}$ agrees with the calculation of Nason, Dawson and Ellis, assuming a reasonable value for the charm quark mass (m_c=1.5 GeV/c^2).

2.3.2 A Dependence

The factorization of the total cross section requires that the charm production process be described at the parton level and that the cross section be independent of the target nuclei.

Experiments	Beam	Targets	α	Technique
E613	Proton	Be,Cu,W	0.75±0.05	Beam Dump
WA78	π^-	Al,Fe,U	0.80±0.05	Beam Dump
WA78	Proton	Al,Fe,U	0.78±0.09	Beam Dump
WA82	π^-	Si,W	0.89±0.05±0.05	Reconstructed charm
E769	π^-	W,Cu,Si	0.95±0.05	Reconstructed charm

Table 2: Measured values for α from different fixed target experiments.

This dependence on the target nuclei is usually parameterized as:

$$\sigma = \sigma_o A^{\alpha}. \tag{4}$$

Early measurements of α done by studying the lepton spectrum from different beam dump targets, reported an α that was inconsistent with a parton description [55,56,57]. Recent results from fixed target experiments with fully reconstructed charm decays are consistent with $\alpha \sim 1.0$ [46,58]. Table 2 list the measured values of α. The A-dependence controversy will be settled when one experiment measures the parameter α for different regions of X_f, since the beam dump experiments had acceptance only at large X_f and the reconstructed charm experiments are dominated by low X_f events.

2.3.3 Differential Cross Section

The charm differential cross section is parameterized by:

$$\frac{d\sigma}{dX_f dP_t^2} \sim (1- \mid X_f \mid)^n e^{-bP_t^2} \tag{5}$$

where:

$$X_f = P_{\|}/P_{\|max} \quad [48] \tag{6}$$

with:

$$P_{\|max} = \sqrt{\left(\frac{M_i^2 - M_r^2 + s}{2 \cdot \sqrt{s}}\right)^2 - M_i^2} \tag{7}$$

and:

- $P_{\|}$ = momentum of the charmed particle parallel to the beam direction
- P_t = momentum of the charmed particle transverse to the beam direction
- M_i = mass of the particle the for which X_f is being calculated
- M_r = mass of the recoil particles in the reaction

Experiments quote results for n and b from their fits to the differential cross section. Figure 6 plots the measured value of n versus the center mass energy for the fixed target experiments. The results from experiments with π beams are all consistent with each other [46,47,53]. The X_f distribution from the LEBC-PP data is much flatter than the extremely central X_f distribution observed by E743 and E653 at higher $\sqrt{s}$. The measured value for the exponent n shows an increase in value at larger values of $\sqrt{s}$. As the energy of the incident proton beam increases a larger fraction of the gluon structure function is used in heavy quark production. The distribution observed by LEBC-PP is not as central as seen at higher $\sqrt{s}$ because only gluons with a large fraction of the proton momentum had enough energy to produce a charm pair. Comparing the π beam data to the proton beam data shows that

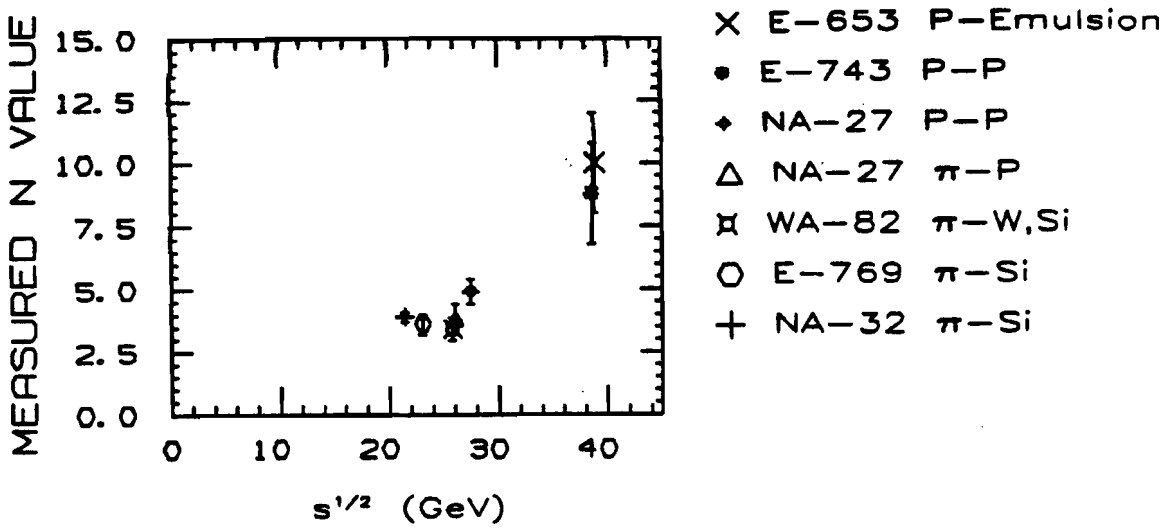

Figure 6: The measured values for the exponent n for the different fixed target experiments.

the X_f distribution is not as central for the π data than for the proton data. This is due to the larger fractional momentum carried by the gluons distribution found in the π compared to that found in the proton.

Theoretically the measured $<P_t^2>$ of the charmed particles should be approximately equal to the charm quark mass (m_c^2). This prediction is borne out by the fixed target measurements. The $<P_t^2>$ from the different fixed target experiments is shown in Figure 7. The measured values are all consistent with $\sim$ (1.0 GeV/c)^2, and do not show any trend with $\sqrt{s}$ or incident beam type.

2.3.4 Charm Pair Results

Single charm production studies have yielded important results on the A-dependence and the total charm production cross section, but it is difficult to determine the details of

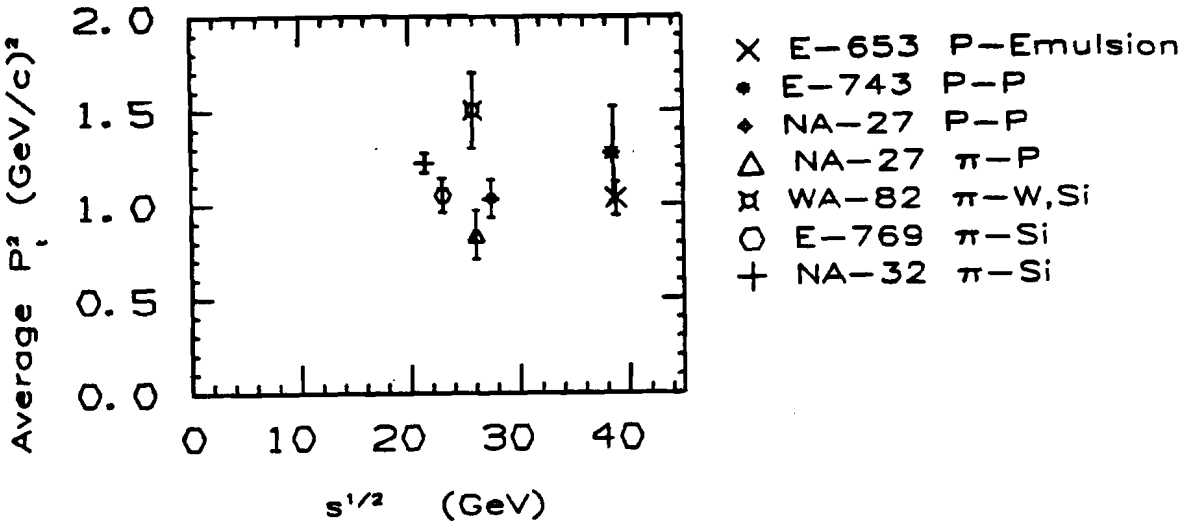

Figure 7: The measured values for the $<P_t^2>$ from the different fixed target experiments.

charm production from single charm production distributions. It is hoped that by studying the kinematics and dynamics within the charm pair system the parton (gluon) structure functions, fragmentation effects and contributions from specific production diagrams can be determined. The analysis would follow the Drell-Yan analysis of di-lepton production in hadron interactions. The Drell-Yan di-lepton analysis and results will be discussed in the next section, but let me remind the reader that the quark and anti-quark structure functions for protons and π's, and the intrinsic transverse momentum (k_t) of the quarks was determined through Drell-Yan analysis. A sample of charm pairs with sufficient statistics and momentum resolution is required for this analysis and the two published samples of charm pairs do not have enough events for such elaborate analysis.

The LEBC experiment collected two sets of charm pairs [51,52]. One set of 12 charm pairs was collected using a 360 GeV/c π^- beam incident on the bubble chamber filled with

liquid hydrogen. (These results will be referred to as LEBC-πP throughout this thesis.) A second run with a 400 GeV/c proton beam collected 17 charm pair events. (Referred to hereafter as LEBC-PP.)

The LEBC-πP and LEBC-PP analyses compared the weighted charm pair X_f, P_t^2, mass, azimuthal opening angle (Φ_t) and rapidity gap (ΔY) distributions with the distributions from charm pairs generated by the LUND Monte Carlo (LUND MC). The LUND MC is a Monte Carlo of high P_t physics in various interactions. The program allows the user to define the incident particles and energies, structure functions of hadrons and the fragmentation functions used to add light quarks to the bare charm quarks to make charmed mesons and baryons. The LUND MC, however, only produces charm pairs via the leading order diagrams.

The LEBC-πP and LEBC-PP pairs distributions agreed quite well with the pairs generated via the LUND MC. The LEBC results agreed best when the intrinsic transverse parton momentum was parameterized by;

$$\frac{dN}{dk_t^2} = e^{-k_t^2/<k_t^2>} \tag{8}$$

with:

$$< k_t^2 >= 0.64(GeV/c)^2 \tag{9}$$

This value for $< k_t^2 >$ was taken from Drell-Yan studies [21]. The parton structure functions of Duke and Owens and the LUND fragmentation scheme were seen by the LEBC collaboration to be superior to other sets of structure functions and fragmentation schemes

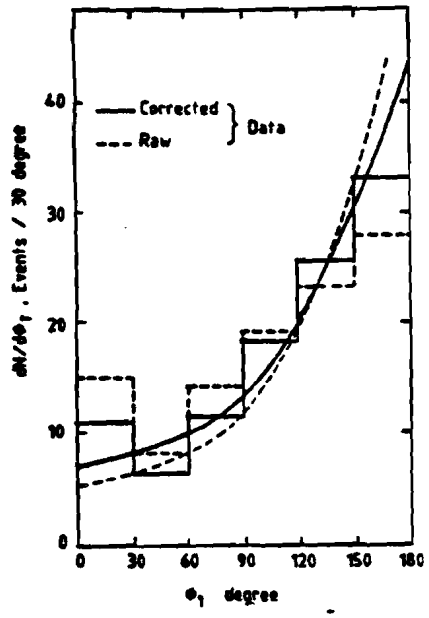

Figure 8: The Φ_t distribution measured by LEBC-PP. There are 107 geometrically reconstructed pairs in the plot.

[15,51].

The LEBC-PP results are shown in Figures 8 and 9. The agreement between the data and the LUND MC charm pairs is quite good. The azimuthal opening angle, Φ_t, of the charm pairs shows the expected peaking at 180°. This peaking reflects the back-to-back nature of the leading order production diagrams. For the LUND MC Φ_t distribution to agree with their data the $< k_t^2 >$ of the partons was set to the maximum value consistent with Drell-Yan di-lepton results. The charm pair mass, X_f and ΔY distributions agree quite well with the distributions generated by the LUND MC. The P_t^2 distribution shows a slight tail that is not reproduced by the LUND MC.

The agreement between LUND MC and the LEBC-PP data is hard to resolve in light of the Nason, Dawson and Ellis cross section calculation. The theoretical charm cross section did not reproduce the measured cross sections until the next-to-leading order production

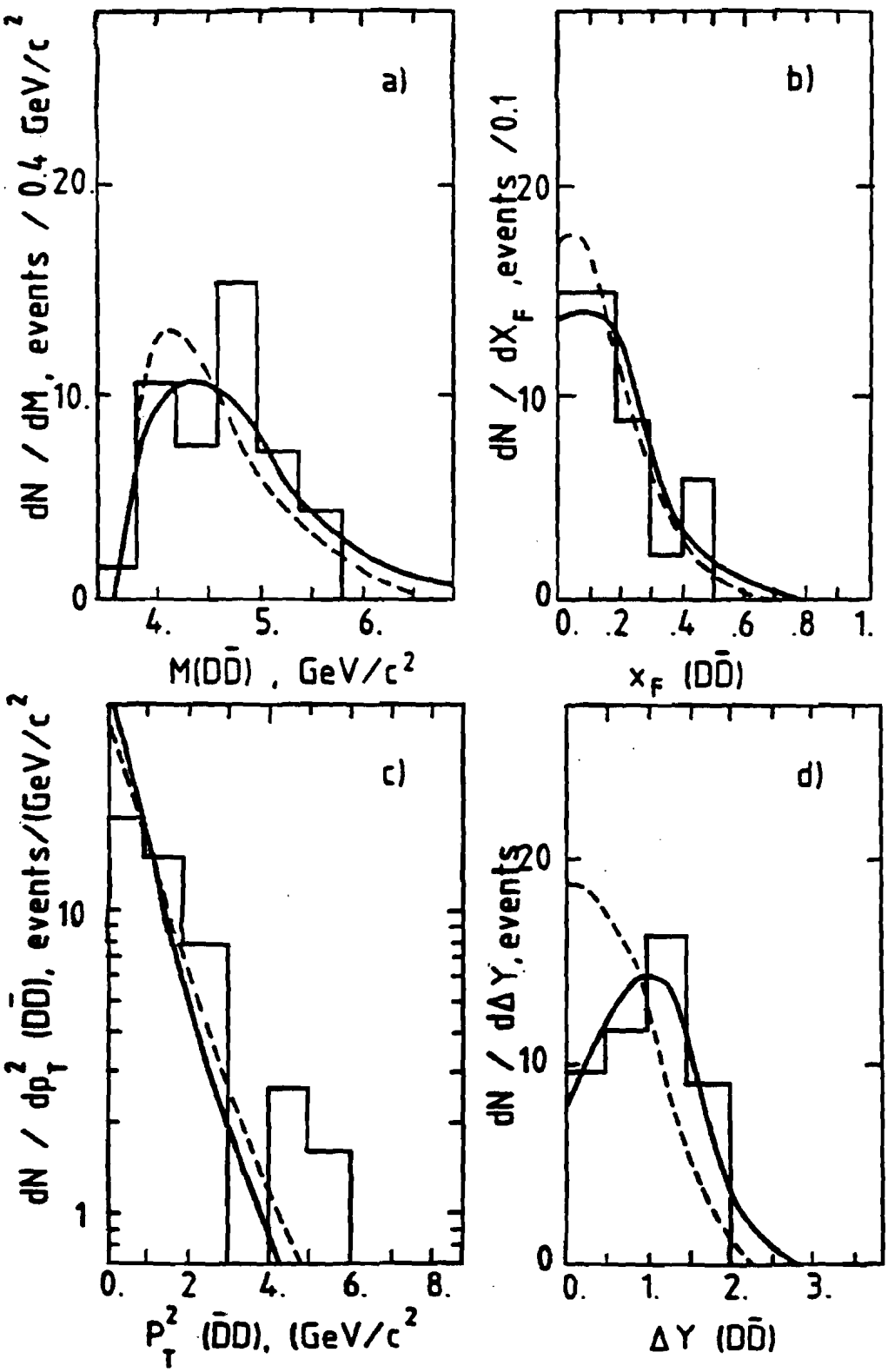

Figure 9: The weighted X_f, mass, P_t^2 and ΔY distributions for the 17 LEBC-PP charm pairs. The dashed curve is from the LUND MC with a δ fragmentation function and the solid curve is the LUND MC with LUND fragmentation.

diagrams were included in the calculation. It could be that the next-to-leading order diagrams contribute only at large Q^2 or mass and the LEBC-πP or LEBC-PP data has not probed that region. A high statistics charm pair experiment with large mass charm pair events is needed to determine the exact role of the production diagrams for leading and next to leading orders.

2.4 Drell-Yan Di-Lepton Production

2.4.1 Introduction

The purpose of this section is not to give an extensive review of Drell-Yan results, but to briefly state some of the scaling observed in the Drell-Yan experiments. Complete and detailed reviews can be found elsewhere [17,20].

2.4.2 The Drell-Yan – Charm connection

The mechanism first proposed by S. Drell and T. Yan for the continuum di-lepton production in hadronic interactions is a quark–antiquark annihilation into a virtual photon that splits into a lepton and anti-lepton pair (Figure 10) [19]. This simple parton description has been very successful in describing the experimental results. The factorization theorem is complete for the Drell-Yan process [11] and the theoretical understanding of di-lepton production is on firm ground.

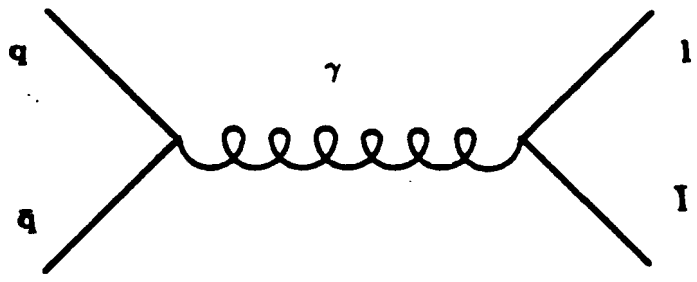

Figure 10: Leading order production diagram for di-lepton production in hadronic interactions.

Total Cross section

The initial total cross section calculations for di-lepton production were lower than the experimental cross sections by more than a factor of two. This discrepancy was accounted for when the next to leading order production diagrams were included in the cross section calculation. This is very analogous to the recent results on the theoretical calculation of the charm cross section. The equation for the prodution cross section is similar to that written for heavy quark production with the number of partons summed over reduced to the quark and anti-quark partons. The perturbative expansion is done through powers of $\ln Q^2/\mu^2$ where Q^2 represents the di-lepton mass squared.

A-dependence

Since di-lepton production in a hadronic environment is perceived as a parton–parton interaction, the total cross section should be independent of the target composition. The α value measured with π and proton beams is consistent with $\alpha = 1.0$. The recent measurements from charm production experiments are also consistent with $\alpha = 1.0$ and the premise of a short order parton–parton interaction being responsible for both di-lepton production and heavy quark production appears to be valid.

2.4.3 Drell-Yan Scaling

The parton description of the di-lepton process simplified the theoretical calculation and allowed for detail predictions of how measured quantities should scale. The prominent scaling observed in di-lepton experiments will be described here along with some of the

important results.

Di-Lepton Mass Scaling

By introducing the dimensionless parameter:

$$\tau = \frac{{m_{ll}}^2}{s} = x_i \bar{x}_j \tag{10}$$

the differential cross section was seen to scale as:

$$s\frac{d^2\sigma}{dyd\sqrt{\tau}} = const \cdot e^{-a\sqrt{\tau}} \tag{11}$$

This scaling allowed experiments performed at different center of mass energies to compare results by comparing their respective values of a. The experimental results were seen to scale over almost two orders of magnitude of $\sqrt{\tau}$. If this scaling holds for charm pairs it will provide a way for different charm pair experiments at different energies to compare results. The value for the exponent for 400 GeV/c proton-platinum interactions is $a = 27.04 \pm 0.17$ [22]. This scaling also reflects the probability distribution of the product of the momentum fractions, $x_i \bar{x}_j$.

Average P_t^2

The average P_t^2 of the di-lepton pair was predicted to scale as:

$$< P_t^2 > = < k_t^2 > + \alpha_s(Q^2) f(\tau, X_f, \ln Q^2) \cdot s, \tag{12}$$

where k_t^2 represents the intrinsic transverse momentum of the partons and X_f is the di-lepton X_f. Thus at constant τ, X_f and Q^2 the relationship is linear:

$$< P_t^2 >_{\tau, X_f, Q^2} = < k_t^2 > + C_{sl} \cdot s. \tag{13}$$

This analysis has been done [21] and has yielded:

$$< k_t^2 > = 0.52 \pm 0.12 (GeV/c)^2 \tag{14}$$

$$C_{sl} = 0.0014 \pm 0.0002 (GeV/c^2) \tag{15}$$

for protons and

$$< k_t^2 > = 0.59 \pm 0.05 (GeV/c)^2 \tag{16}$$

$$C_{sl} = 0.0028 \pm 0.0002 (GeV/c^2) \tag{17}$$

for π's.

Since Drell-Yan production proceeds through quark-antiquark annihilation the $< k_t^2 >$ measured is that of the quarks and antiquarks. Charm pair analysis would measure the intrinsic k_t^2 of the gluons that dominate the charm pair production process.

2.4.4 Structure Functions

Large statistic di-lepton experiments were able to determine the structure functions of the quark and anti-quarks inside the incident proton and pions. This was done by studying

di-lepton mass distributions at constant pair rapidity. For πp interactions the cross section is dominated at large x_p and x_π by the product of the structure functions, $f_{\bar{u}}^{\pi}(x_\pi)$. The structure functions of the sea quarks determined in deep inelastic lepton scattering for the proton, $f_u^p(x_p)$, are used to unfold the structure function of the incident pion, $f_{\bar{u}}^p(x_\pi)$. In the case where the structure functions of both particles are unknown the structure functions can be extracted by studying the di-lepton mass distribution at $X_f(l\bar{l}) = 0$.

The same analysis can be applied to high statistics charm pair data and the structure functions of the gluons in protons, pions and kaons can be measured. This might be the only way to directly measure these distributions.

The di-lepton production analysis has made important measurements of the quark distributions inside the incident hadrons. It has also provided a test of perturbative QCD. Charm pair production holds the same promising future however both the experimental and theoretical aspects of charm pair production are much more complicated that those for di-lepton production.

Chapter 3

The Hardware

3.1 Introduction

E653 was designed to study the properties of charm production in hadronic interactions and their subsequent decays. The known characteristics of hadronic interactions and charm decays were used to optimize the expected charm yield.

These considerations were:

- The ratio of the charm cross section to the total cross section in hadronic:photon:neutrino:e^+e^- interactions is approximately 0.001:0.01:0.1:1.

- Typical charm meson lifetimes were then measured at:

  $c\tau(D^{\pm}) = 0.320 \pm 0.010$ mm

  $c\tau(D^{o}) = 0.1283 \pm 0.0033$ mm

- The semi-leptonic branching ratios for heavy quarks were measured to be large and roughly 10% [25].
- Average charged track multiplicity in hadronic interactions is large, approximately 15 tracks per event.

The solution to these hard technical problems was the following:

- An emulsion target with 1μm spatial resolution could resolve the short decay lengths characteristic of charmed particles and handle the high charged track density.
- High resolution silicon strip detectors would aid in selecting charm events and predicting their location in the emulsion.
- A Muon trigger to select events with a high momentum muon, thereby reducing the non-charm background.
- Reconstruct this trigger muon throughout the spectrometer and use the resolution of the silicon strip detectors to determine if the muon is consistent with coming from a decay.

These were the primary ideas behind the E653 hybrid emulsion-spectrometer technique. The plan view of the complete experiment is shown in Figure 11. Each detector had its own internal geometry and coordinate system, which had to be converted to the chosen E653 coordinate system shown in Figure 12. The E653 coordinate system was a right handed system with the Z-axis along the beam direction, see Figure 12. The hardware that was used consisted of the following:

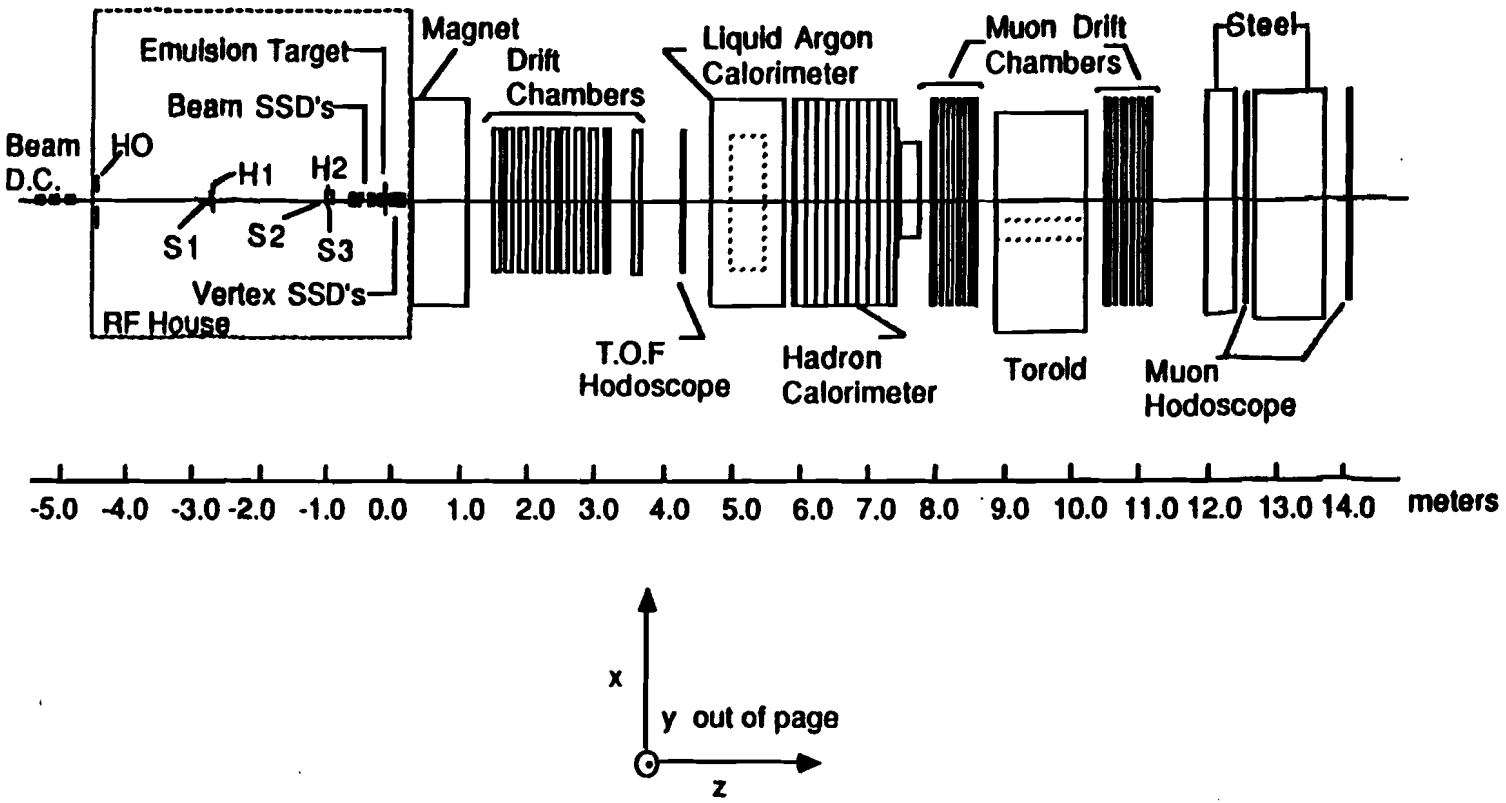

Figure 11: Plan view of the compact E653 spectrometer.

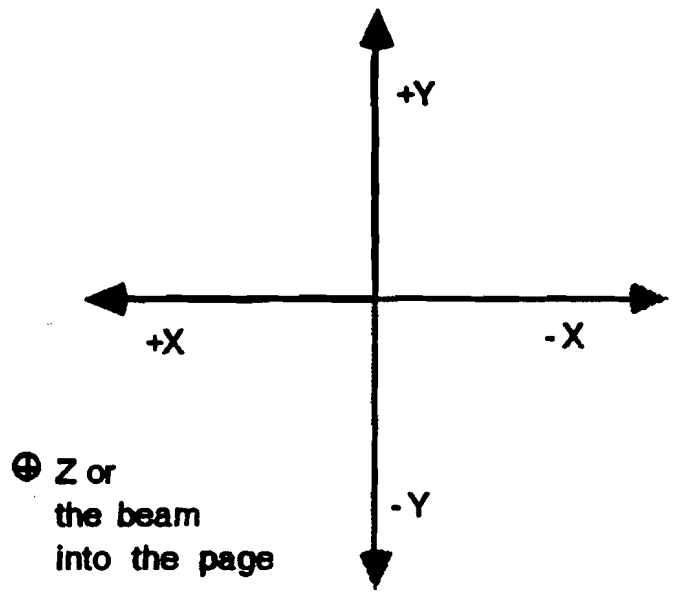

Figure 12: The E653 coordinate system.

- Beam system: The beam proton trajectory was determined before it enter the emulsion by a drift chamber system coupled with 9 planes of 20μm pitch silicon strips. The beam track provided an important starting point in reconstructing the primary vertex.

- Emulsion target: There were two types of emulsion targets, vertical and horizontal, with 14mm and 20mm thickness, respectively. The emulsion targets were uniformly exposed by moving the emulsion during data taking.

- Vertex silicon strip detectors: Following the emulsion were 18 planes of 50μm pitch silicon strip detectors. The vertex silicon strip detectors (VSSD's) measured the charged track trajectories upon leaving the emulsion target.

- Analyzing magnet and vector drift chambers: The charged tracks were then bent by

the magnetic field of the analyzing magnet and the new trajectories were measured by 10 vector drift chambers (SDC's). Track linking between the VSSD's and SDC's provided the momentum measurements for the charged tracks.

- Time of flight, liquid argon calorimeter, and hadron calorimeter: Low momentum particles were identified by the time of flight (TOF) system immediately downstream of the SDC's. Following the TOF system was the liquid argon calorimeter (LAC) that provided electron identification, γ tagging and π^o reconstruction. Long lived hadrons deposited their energy into the hadron calorimeter that followed the LAC.

- Muon spectrometer and trigger: Following the hadron calorimeter was the muon spectrometer which consisted of ranging steel, 12 drift chambers, a toroidal magnet, and the muon hodoscope. The muon spectrometer provided a completely independent measurement of the muon momentum crucial in linking this track to the upstream spectrometer. The muon trigger was accomplished by requiring a coincidence between the front and back sections of the muon hodoscope that followed the muon spectrometer.

Of course there are always sacrifices to be made when designing an experiment and this case the notable compromises in the design were (hindsight is a wonderful thing):

- The multiple scattering in the thick emulsion target would reduce the vertex resolution of the VSSD's.

- For the muon trigger to have a large acceptance and to reduce the number of μ's from π decay the spectrometer must be short (Total length from target to muon hodoscope

Subsystem	Reference
Overall	[28,30,36]
Emulsion	[34]
VSSD's	[28]
SDC's	[27]
LAC	[26,31]
Hadron calorimeter	[32]
Muon Spectrometer	[29,33]
Data Acquisition	[30]

Table 3: References for the E653 spectrometer and its components.

was 15m). This short spectrometer does not allow the use of Cerenkov detectors for particle identification.

- The muon trigger forces one of the decay particles to be semi-leptonic. This decay due to associated neutrino daughter cannot have a precise momentum determination.

The muon trigger has turned out to be an exceptional advantage in studying of the semi-leptonic decays of charm mesons.

It is the purpose of this chapter to describe the apparatus needed for the charm pair production analysis (Beam system, emulsion target, charged particle spectrometer, and the muon spectrometer). The E653 apparatus has been described in detailed elsewhere, and I would at this time direct the reader to the theses and papers in Table 3 for complete detailed information on the E653 emulsion-spectrometer.

3.2 Beam Line

E653 ran with the highest possible proton beam energy available to take advantage of the dependence of the charm cross section on the center of mass energy (see Figure 5). In 1985 this meant using the 800 GeV proton beam available from the Fermilab accelerator. The intensity of the proton beam was controlled by a triangular cross section shaped tungsten attenuator and ranged between 10^4 and 10^7 protons/sec. The beam spot was required to be less than 3mm x 3mm in area, to ensure that the region of highest track density passed through the central region of the electronic spectrometer. The beam halo, integrated over $10cm^2$, was required to be less than 7% of the beam intensity. The small halo was necessary to ensure that the emulsion did not become blackened by uninteresting tracks. The beam line chosen for E653 was the NE beam line shown in Fig. 13 of the Fermilab accelerator and beam line complex.

3.3 Beam System

The beam proton's trajectory was determined by the E653 beam system. The beam system consisted of two independent detectors, the beam drift chambers (BDC's) 500cm upstream of the emulsion and the beam silicon strip detectors (BSSD's) situation 27cm upstream of the emulsion target. The beam track was an important part of the primary vertex reconstruction since it limited the window transverse to the beam direction in which the primary interaction occurred.

The upstream (BDC) element of the beam system was a conventional drift chamber

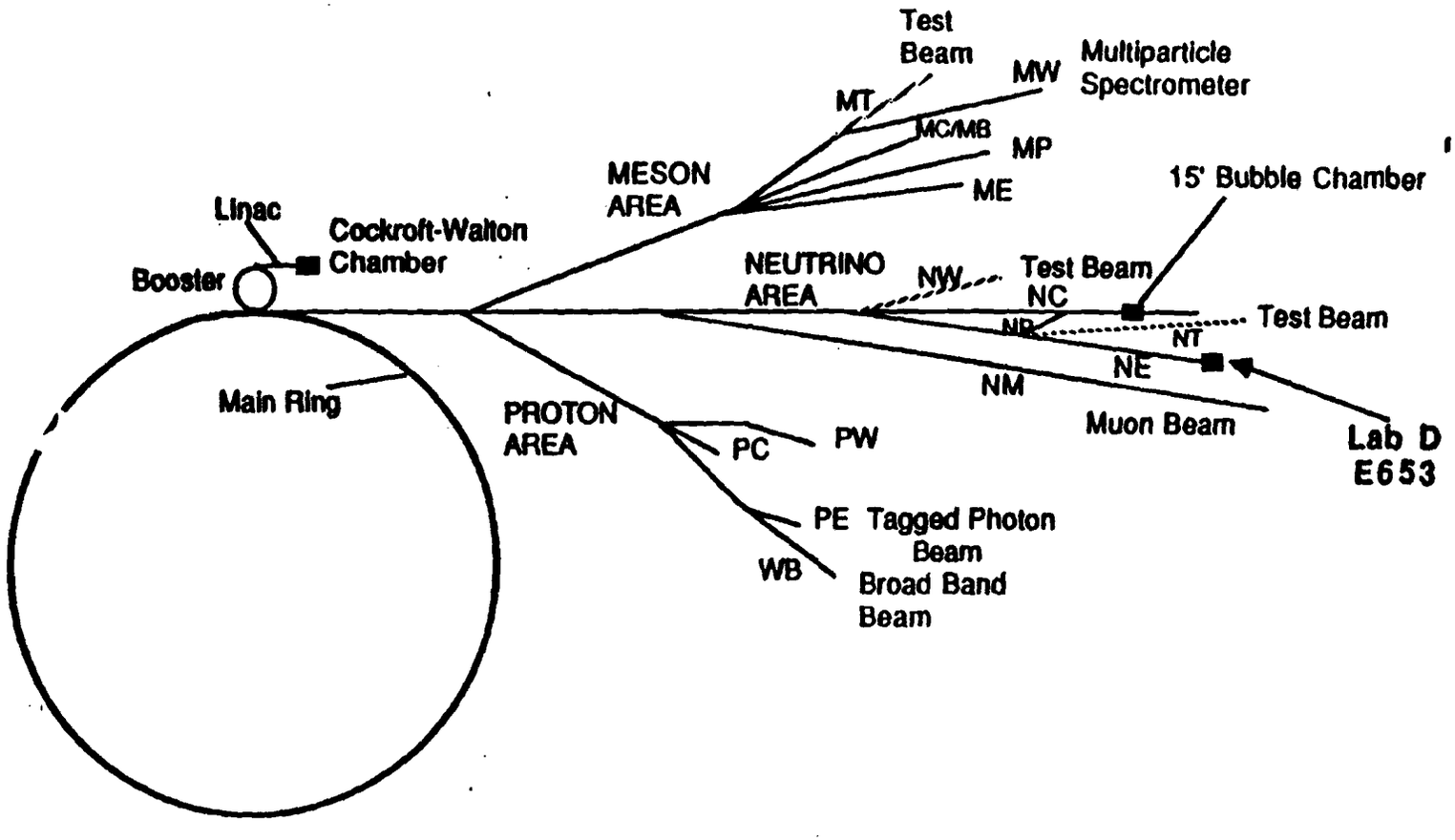

Figure 13: The Fermilab accelerator complex with the fix target beam lines.

composed of 18 planes in three different views, X, U and V, with the U and V views making a $\pm 60^o$ angle with the X axis. Each plane had two sense wires per plane. The planes were grouped in pairs with the same orientation but with the wires offset within the pair to aid in unfolding ambiguous tracks. The resolution of the BDC was 150 μm (microns)/plane.

The BSSD's located 27cm in front of the target provided another measurement of the beam position. There were 9 planes of silicon strip detectors with 20 micron pitch in the BSSD system. The planes were arranged in the same XUV projections as the BDC's. Only the center 1.24 cm region of the 3.4cm x 3.6cm detectors was implemented since the beam was confined to a 3mm x 3mm spot size. This central region of the silicon strips had a position resolution of 10 microns.

The complete beam system had an overall angular resolution of 20 μrad and a position resolution of 10 microns. Figure 14 shows the beam spot and slope as measured by the beam system.

3.4 Emulsion Target

The emulsion target provided the target nuclei for the incident proton and served as a detector for the outgoing charged tracks. These two uses for the emulsion defined its design criteria. The emulsion target had to be thick enough to provide a reasonable rate of primary interactions yet thin enough so that the products of the primary interaction could escape the emulsion without considerable multiple scattering. A thin emulsion would also reduce the probability of a track from the primary interaction interacting with an emulsion nucleus

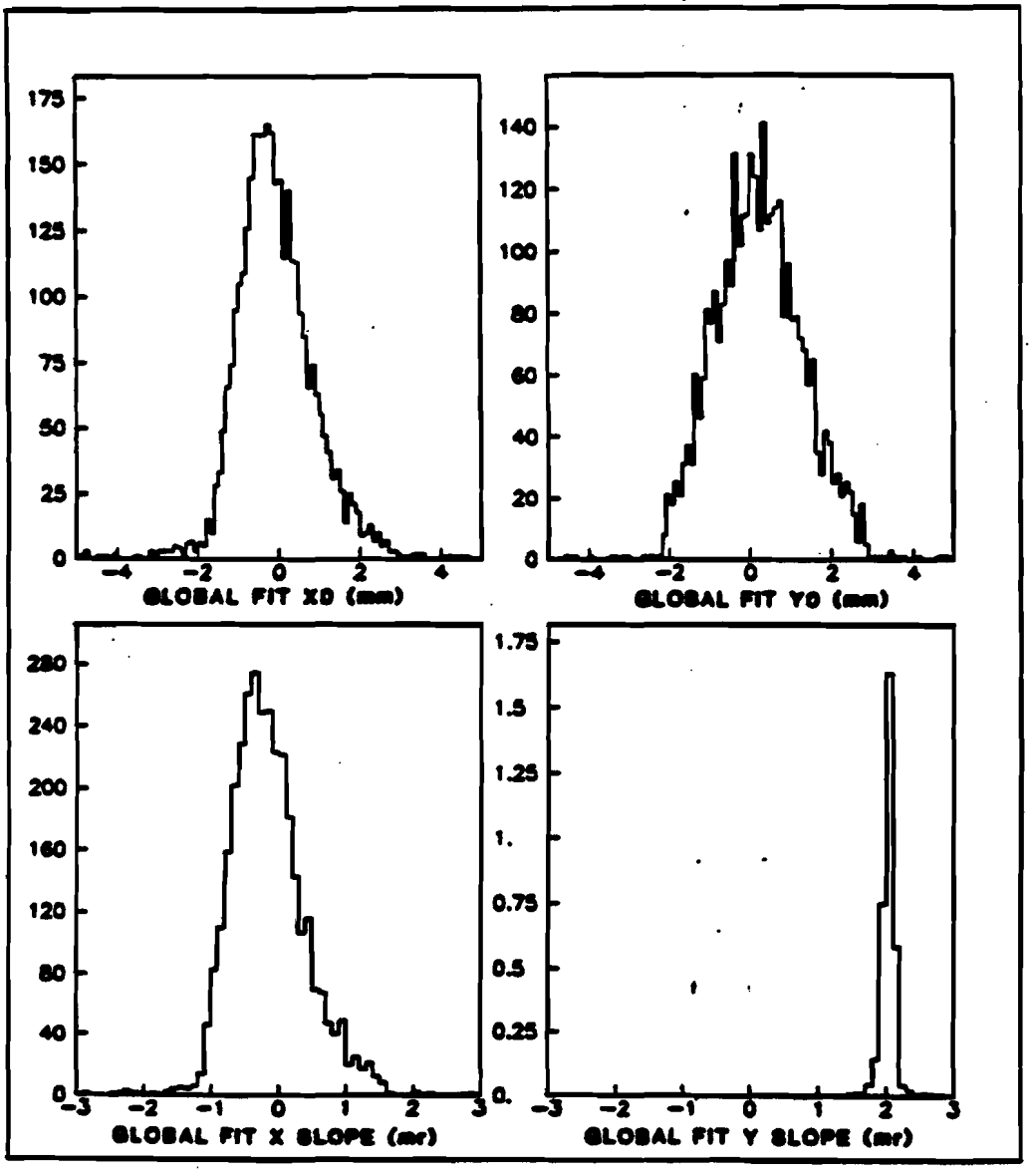

Figure 14: The integrated beam spot of the 800 GeV proton beam measured by the beam system.

Element (i)	Weight % (W_i)	Atomic Weight (A_i)	Atomic Number (Z_i)	Number % (N_i)
I	0.3	126.90	53	0.1
Ag	45.4	107.87	47	11.7
Br	33.4	79.90	35	11.1
S	0.2	32.06	16	0.2
O	6.8	16.00	8	11.3
N	3.1	14.01	7	5.9
C	9.3	12.01	6	20.6
H	1.5	1.01	1	39.6
Totals	100.0	<A>=26.64	<Z>=12.42	100.0

Table 4: Chemical composition of Fuji ET-7B nuclear emulsion. The value for <A> was calculated assuming a linear dependence on A.

(secondary interactions), and the number of gamma conversions.

Nuclear emulsion is always active. This meant that the amount of stray (out of BSSD, VSSD acceptance) protons or halo in the beam had to be kept to a minimum (less than 7% of the total intensity). The emulsion was moved throughout the beam spill at a constant rate to insure uniform exposure of the emulsion block.

The nuclear emulsion used in E653 was Fuji E7-7B. The chemical composition is given in Table 4 taken from [30] along with the calculation for the average effective atomic weight. This calculation was done assuming a linear A dependence.

During the Run I (1985) 32 liters of emulsion were exposed in four months of running. This corresponded to 49 target modules. The target modules came in two different configurations, vertical and horizontal.

3.4.1 Vertical Emulsion Module

Most (71%) of the data was taken with vertical emulsion targets. The vertical targets consisted of a closely spaced region, the main emulsion block, of emulsion sheets (called pellicles) and followed by a region of spaced out pellicles, the analyzing region. The pellicles were oriented perpendicular to the beam. Figure 15 shows the configuration of the pellicles for a vertical module. The vertical modules represented 0.043 interaction lengths and 0.473 radiation lengths of material. The analyzing region allowed the emulsion scanners to follow tracks far from the primary interaction and locate daughter tracks from decays from long lived particles. The density of beam proton tracks for the vertical modules was 1.5 x 10^5 protons/cm^2 this corresponds to an average incoming beam track separation of 26 μm. This separation was enough for the emulsion scanners to distinguish separate events.

3.4.2 Horizontal Emulsion Module

Figure 16 shows the configuration of the horizontal emulsion modules. The beam was incident on the edge of the pellicles. The main horizontal emulsion block was also followed by a analyzing region of spaced out emulsion sheets. A horizontal module represented 0.064 interaction lengths and 0.719 radiation lengths of material. The density of beam proton tracks was 0.5 x 10^5 protons/cm^2 for the horizontal module. This track density corresponds to an average incoming beam track separation between 77 μm.

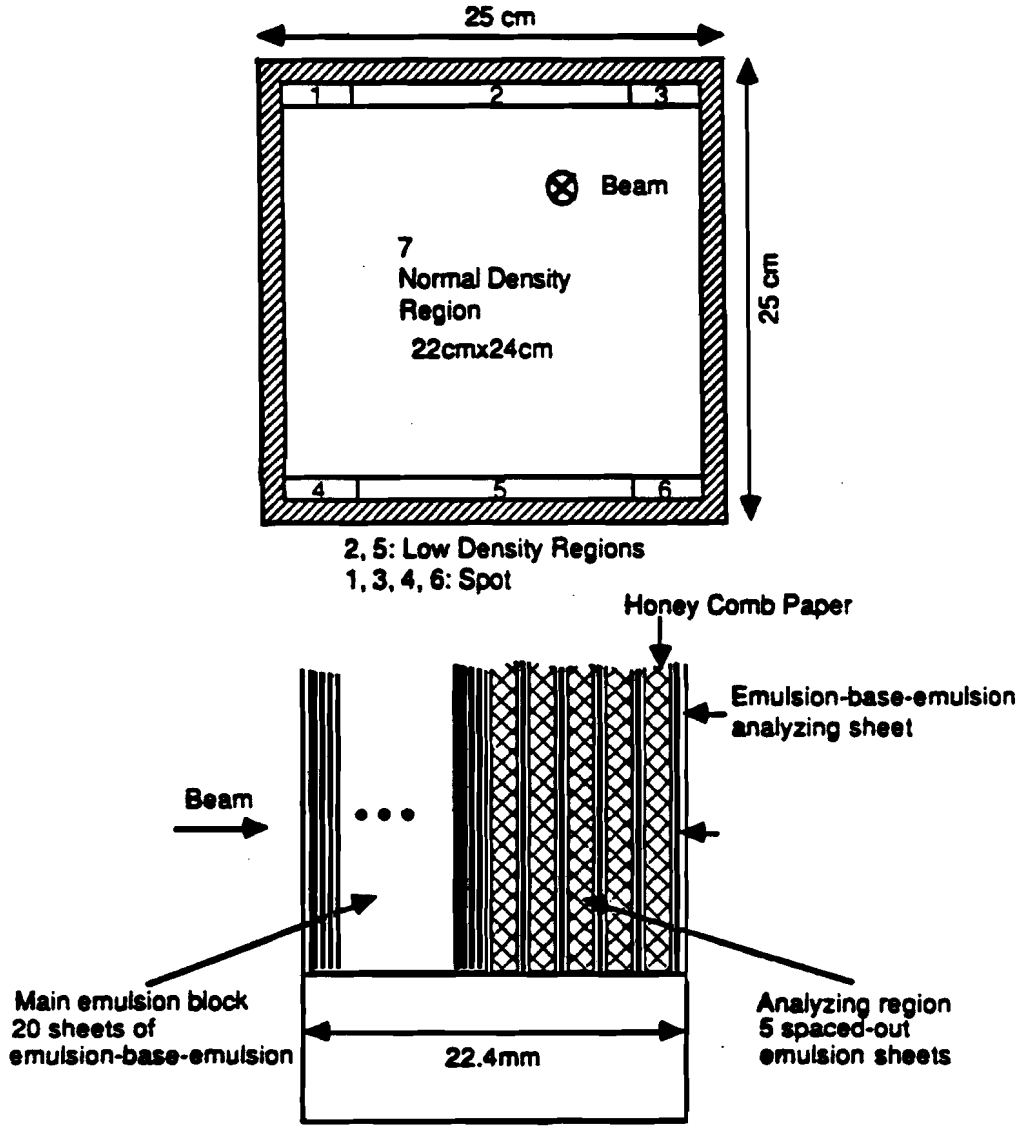

Figure 15: The configuration of a vertical emulsion module.

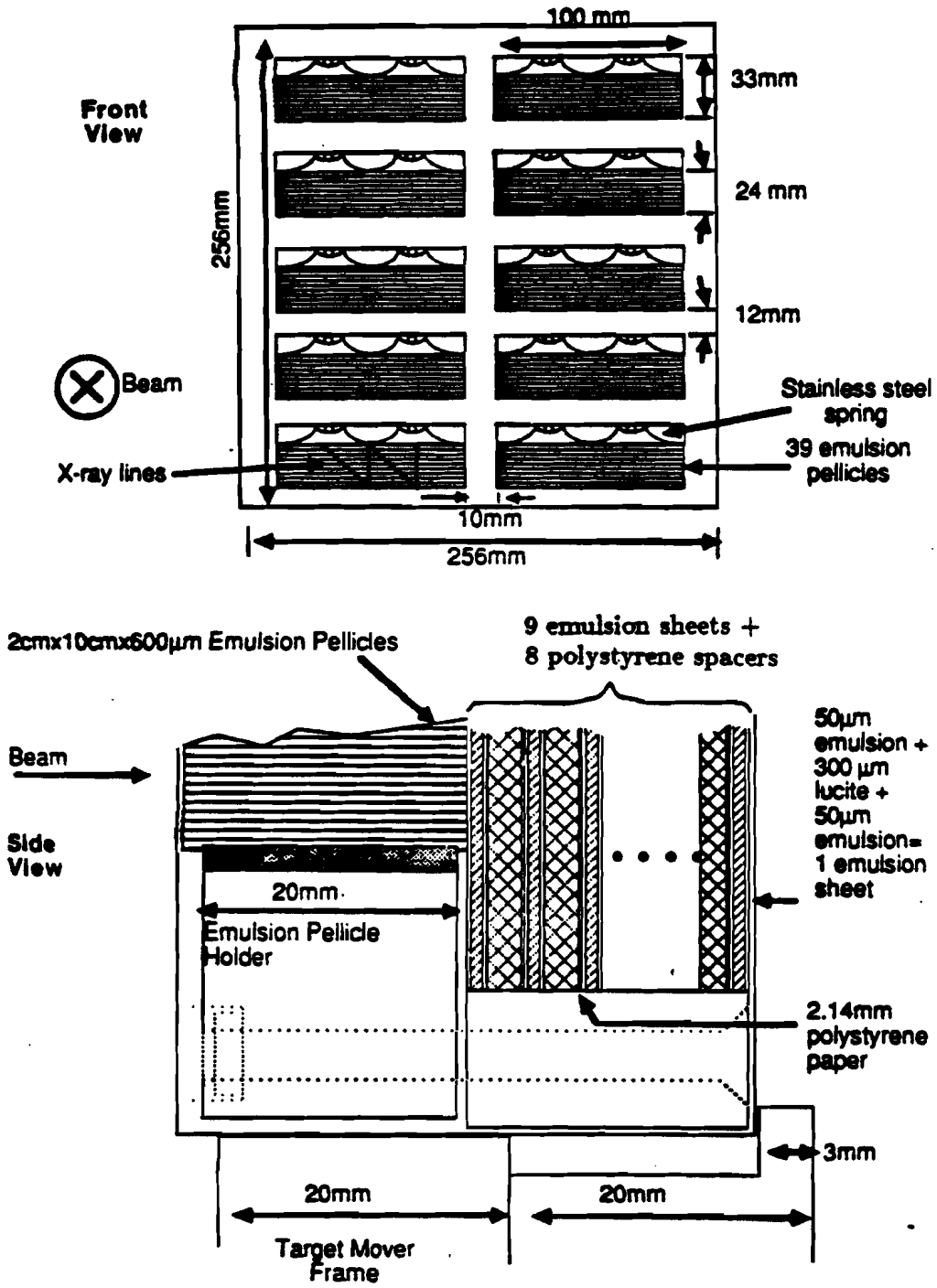

Figure 16: Horizontal emulsion target module configuration.

3.4.3 Emulsion Alignment

The exposure density in the emulsion was kept constant by moving the emulsion transverse to the beam during the beam spill. The target mover coordinates were latched and incorporated into the event information upon triggering. These coordinates were accurate to 1 micron and determined the event location.

Internal calibration of the emulsion modules and alignment to the electronic spectrometer was an important and difficult task. Upon developing the emulsion module shrinks and distorts. By controlling the developing process (uniform drying temperature) the shrinkage is kept as uniform as possible. Internal calibration was accomplished by beam spots and x-ray marks. Beam spots were exposures to the beam at known positions, by comparing the distance between beam spots before and after developing the shrinkage can be accounted for. The horizontal modules used an x-ray gun to etch lines into the pellicles. By aligning x-ray lines the horizontal pellicles could be calibrated relatively.

Alignment to the electronic spectrometer was done by aligning beam track trajectories from the beam system to tracks in the emulsion. To aid this alignment each module was framed with a low track density region to allow this matching to proceed in a relatively clean environment. This alignment had a precision of $\sim$10 microns and allowed event location in the emulsion to proceed quickly.

3.5 Charged Particle Spectrometer

Upon leaving the emulsion module the particles entered the first arm of the charged particle spectrometer, the vertex silicon strip detectors(VSSD's). The charged particles were bent by the magnet field of the analyzing magnet, SCM-104, before entering the spectrometer drift chambers (SDC's) that followed the magnet. This system not only provided momentum measurements for the charged tracks, it also provided vertex reconstruction. The most important being the position of the primary nuclear interaction.

The spectrometer was designed to cope with the high track multiplicity and high density of tracks in the highly collimated central region. The VSSD's achieved a two track separation of 60 microns, and the spectrometer drift chambers had two track separation of 600 microns.

3.5.1 Vertex Silicon Strip Detectors (VSSD's)

The VSSD's were composed of 18 planes of 5cm x 5cm silicon strip detectors. The center to center strip distance (pitch) was 50 microns. The 18 planes were stacked 7mm apart in Z and strips were positioned in there different projections X, U and V with the U, and V projections at an angle of $\pm 60^o$ with the X axis. The entire stack was positioned 71mm from the upstream face of the target emulsion and was approximately 150mm in length. The 5cm x 5cm detector furthest from the target had an acceptance of 110mrad x 110mrad. However, tracks with larger angles could be reconstructed in the planes closer to the target.

The 50 micron pitch and 5cm width translates to 1000 lines per detector. To economize electronic costs and cooling needs not every line was read out. Figure 17 shows the read-out

structure of the VSSD's. The central 7.95mm of the VSSD's had every line instrumented, every other line was read out in the next 3.6mm. Every third line was read out 7.575mm from the center strip to 9.975mm. The outer 15mm had every fifth line instrumented. Capacitive coupling between adjacent strips permitted a charge sharing algorithm to achieve a spatial resolution better than the instrumented strip separation alone would give. The amount of charge deposited in each strip was recorded and the amount of charge determined how far from the instrumented strip the particle hit the detector. The residuals for the four different read out regions are shown in Figure 18 and the resolution for the central region was measured to be 8.8 μm rms. The decision to read out the pulse height from each strip, instead of just recording whether or not the strip had activity (0/1) meant that 7000 lines of VSSD information had to be digitally converted and read out by the data acquisition system.

The detectors had 96% efficiency during the run and required very little maintenance.

3.5.2 Analyzing Magnet

The charged particles were bent by the magnet field of the SCM-104 analyzing magnet. The gap separation was 50.8cm with shaped pole pieces to increase the magnetic field without losing any acceptance. This asymmetric shape, shown in Figure 19, resulted in a non-uniform field that had symmetry in the Y-Z plane only.

The field was mapped out in intervals of 12.7mm in ΔZ and 25.4mm in ΔX and ΔY.

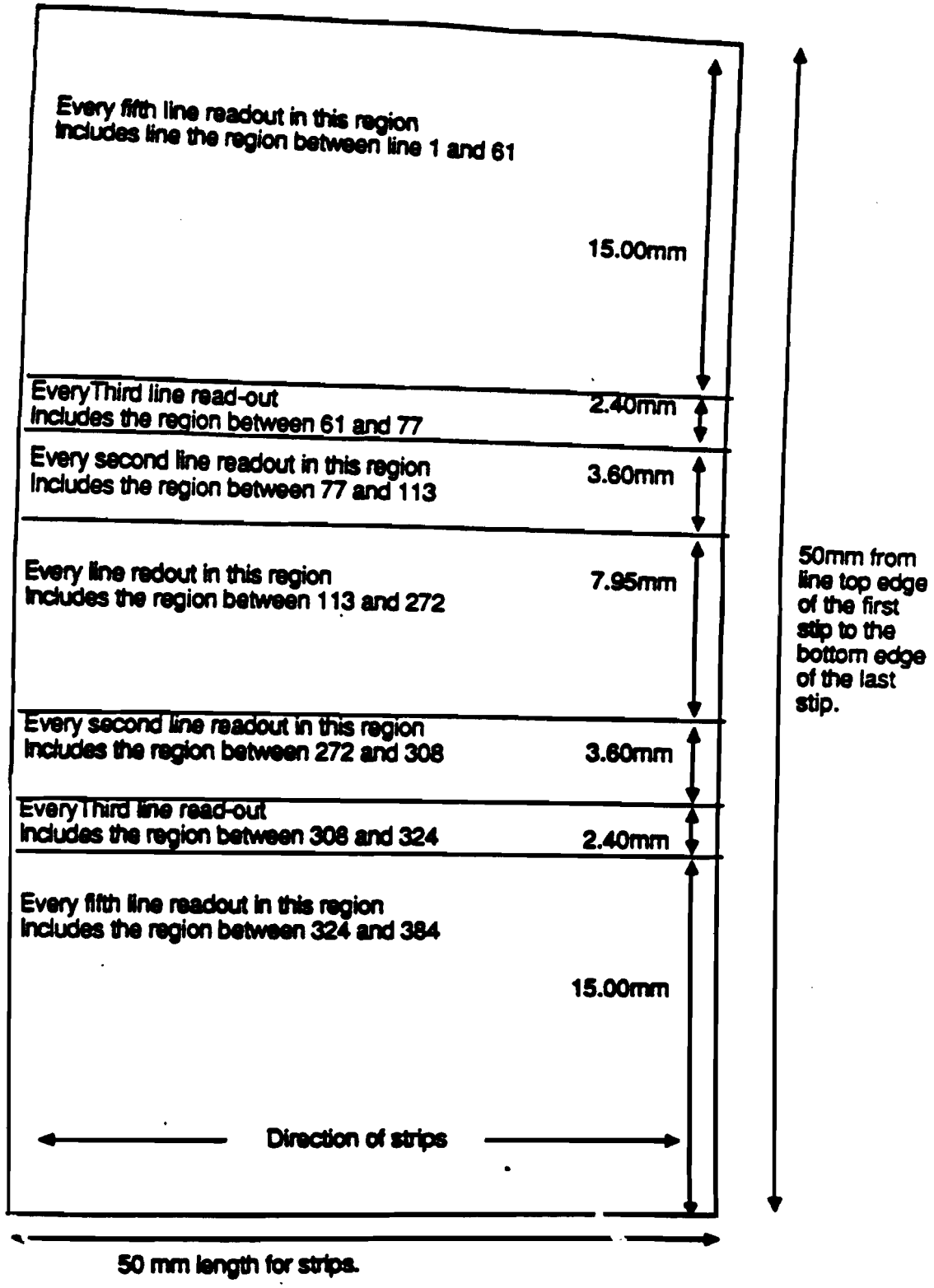

Figure 17: Read out pattern for the vertex silicon strip detectors.

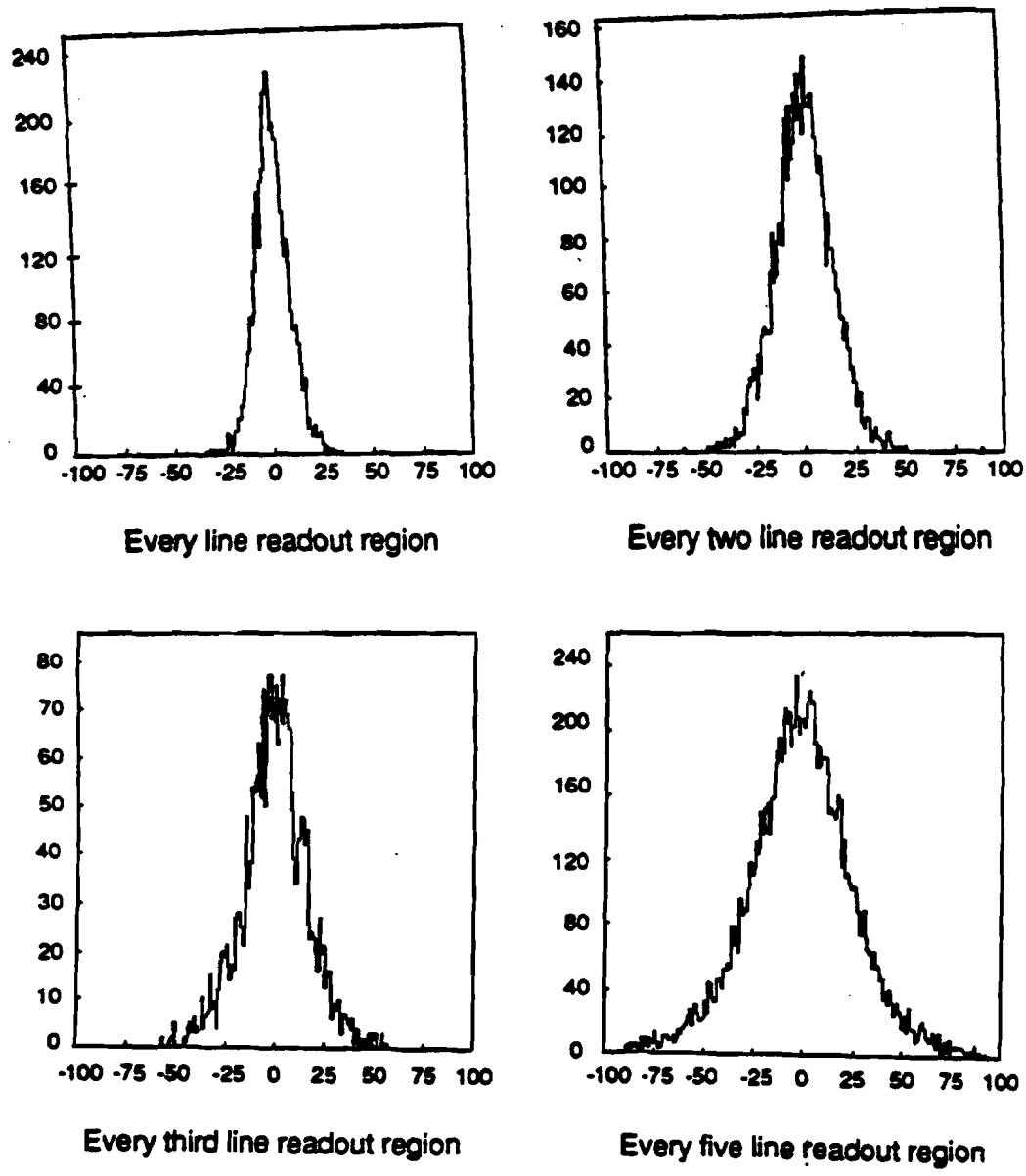

Figure 18: Residuals in the vertex silicon strip detectors.

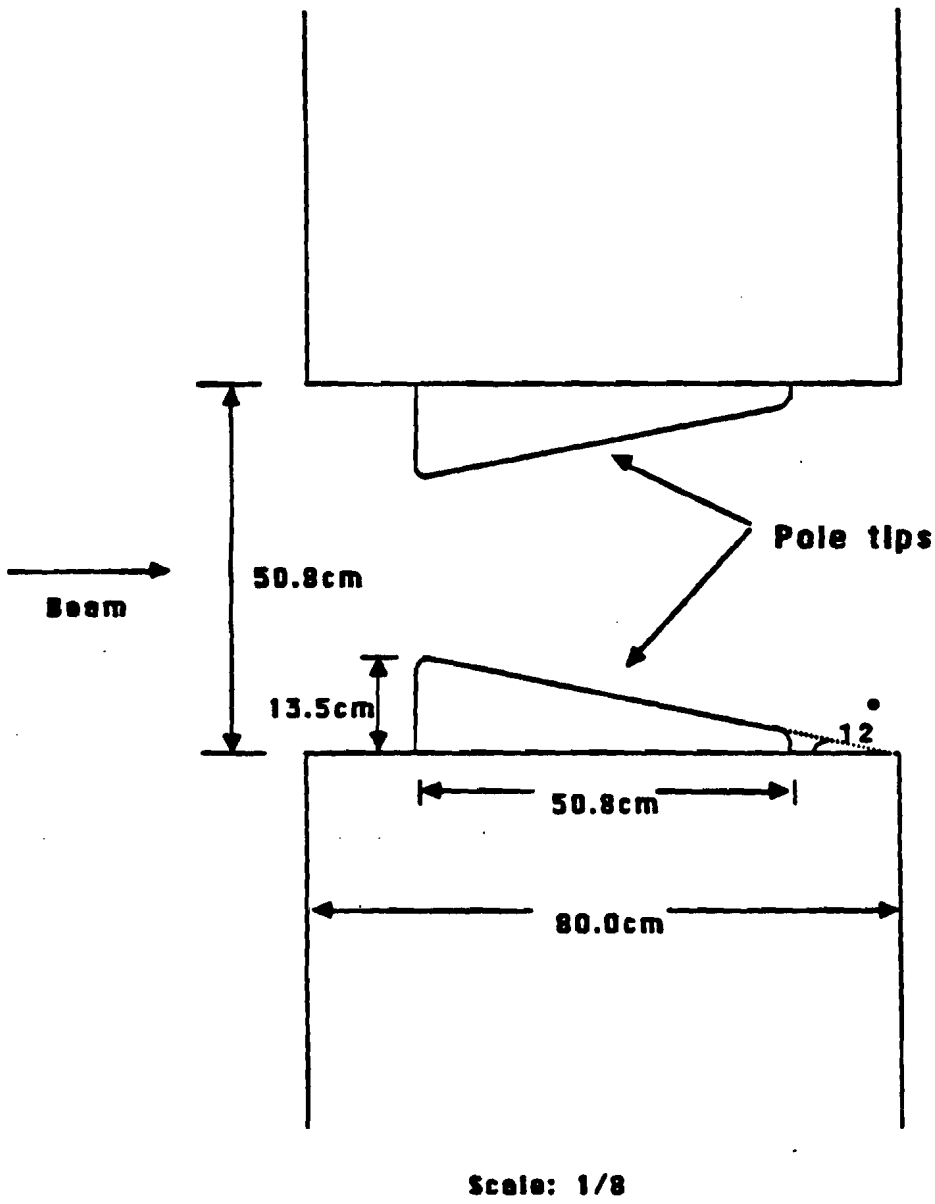

Figure 19: The poles of the analyzing magnet, SCM-104.

The integrate field strength at 2400 amps was

$$\int B \cdot dl = 11.2\ kilogauss \cdot meters \tag{18}$$

The magnet imparted a transverse kick of 0.336 GeV/c to the charged particles.

3.5.3 Spectrometer Drift Chambers

Completing the charged particle system were 10 multi-sampling "vector" drift chambers located down stream of the analyzing magnet. The chambers covered a 1.7 x 1.7m^2 area transverse to the beam and were in there different projections X, U and V, with the U and V projections rotated $\pm 30^o$ with respect to the X axis. The term multisampling comes from the 5 position samplings (at 1.02cm spacings) along the Z-axis per chamber. Transverse to the beam axis the chambers were divided into 22 cells. The central 10 cells were called 'fine' cells and had a drift distance of 2.54cm with sense wires every 5.1mm along the z direction. Surrounding the fine cells were 6 'coarse' cells. The coarse cell were identical to the fine cell except the sense wire spacing was twice that of the fine cells. Figure 20 shows the wire positions for the two types of cells. The chambers were operated a 1 atmosphere of pressure and a 50% argon, 49.5% ethane and 0.5% ethanol gas mixture.

Figure 21 shows the position residuals for the SDC's. When a single beam track passed through the chambers, the resolution was 110 microns rms. For typical secondary tracks the resolution was 140 microns.

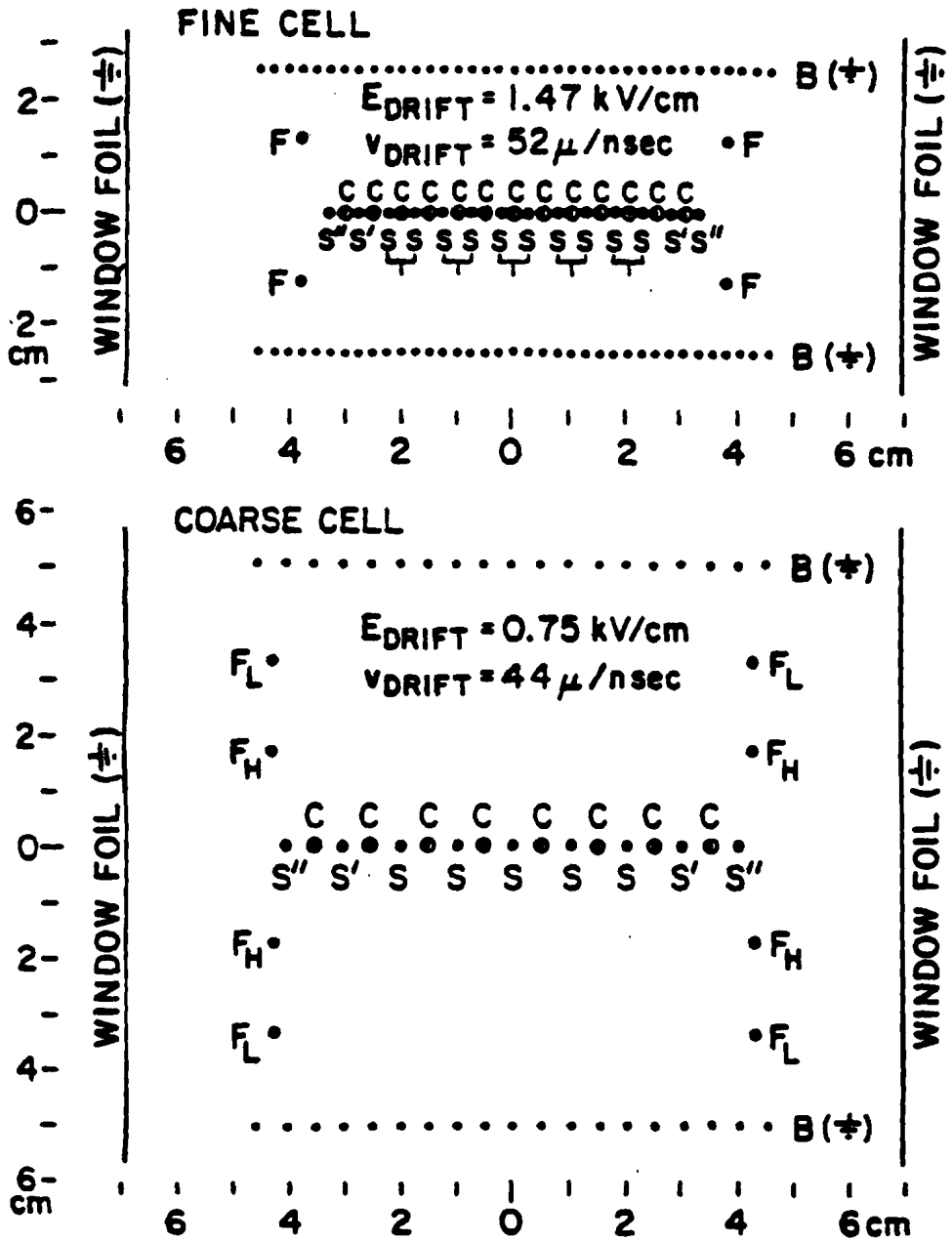

Figure 20: Wiring diagram for the fine and coarse cells in the spectrometer drift chambers.

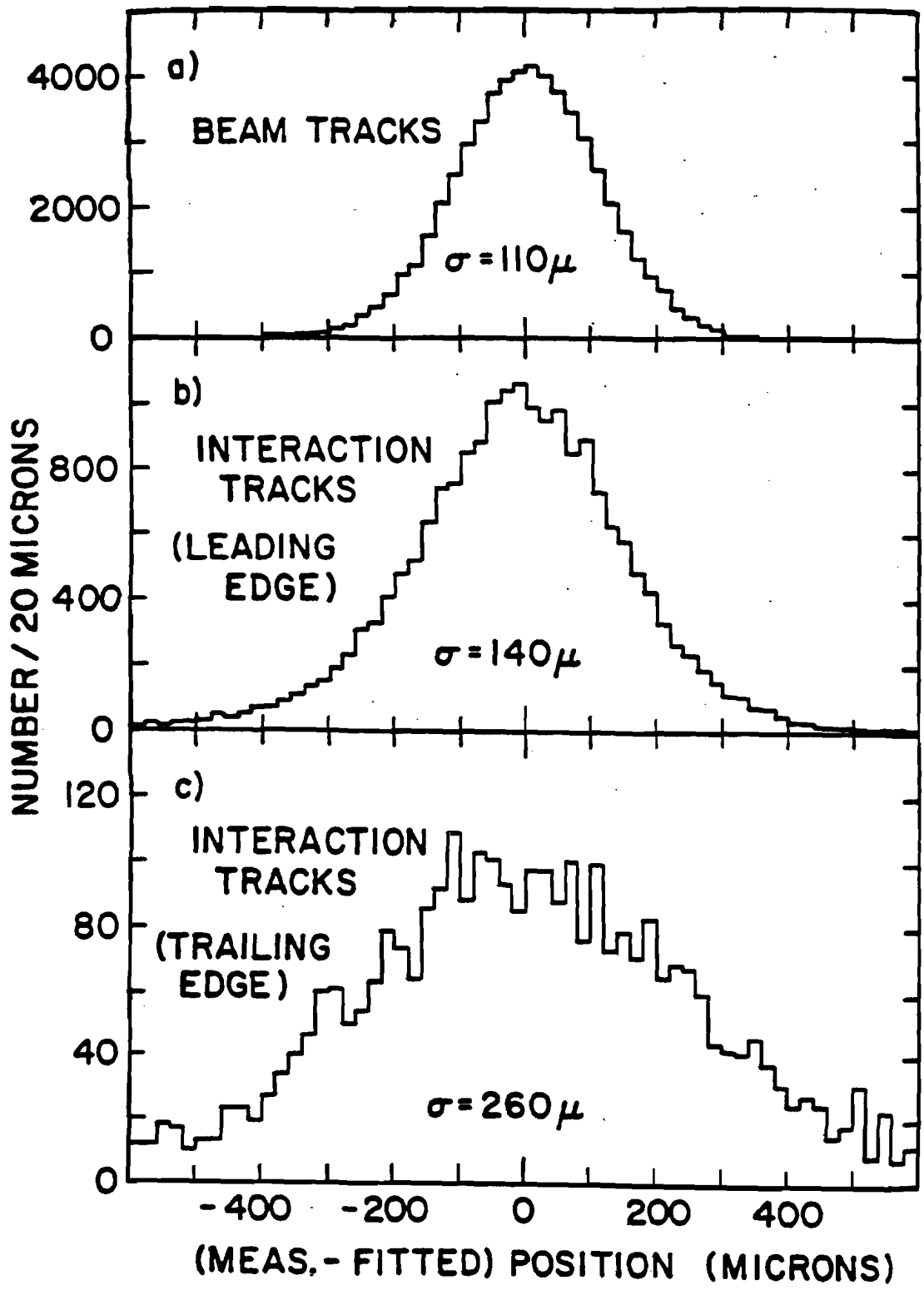

Figure 21: Position residuals for the spectrometer drift chambers.

3.5.4 Momentum

The charged particle spectrometer provided momentum measurements for tracks that were linked between the VSSD's and SDC's. For charm selection a simple thin lens approximation was used to determine the momentum. The error in this calculation was:

$$\delta p/p = \sqrt{(0.01)^2 + (0.00023p)^2} \quad p \ in \ GeV/c \tag{19}$$

The first term is from multiple scattering and second term is the contribution from slope measurement errors. An attempt to incorporate a Runge-Kutta iterative integrated fit to the track trajectories through the magnetic field found no significant improvement over the thin lens approximation [31]. The thin lens momentum estimate was used throughout this analysis.

3.6 Muon System

The muon system provided the only particle identification used in this analysis. Muons were tagged by scintillation counters placed down stream of 26 interaction lengths of material. The muon hodoscope was preceded by the muon spectrometer which provided an independent measurement of the muon trajectory and momentum. The muon spectrometer consisted of two sets of 6 drift chambers and a toroidal magnet. Figure 22 shows the plan view of the complete muon system.

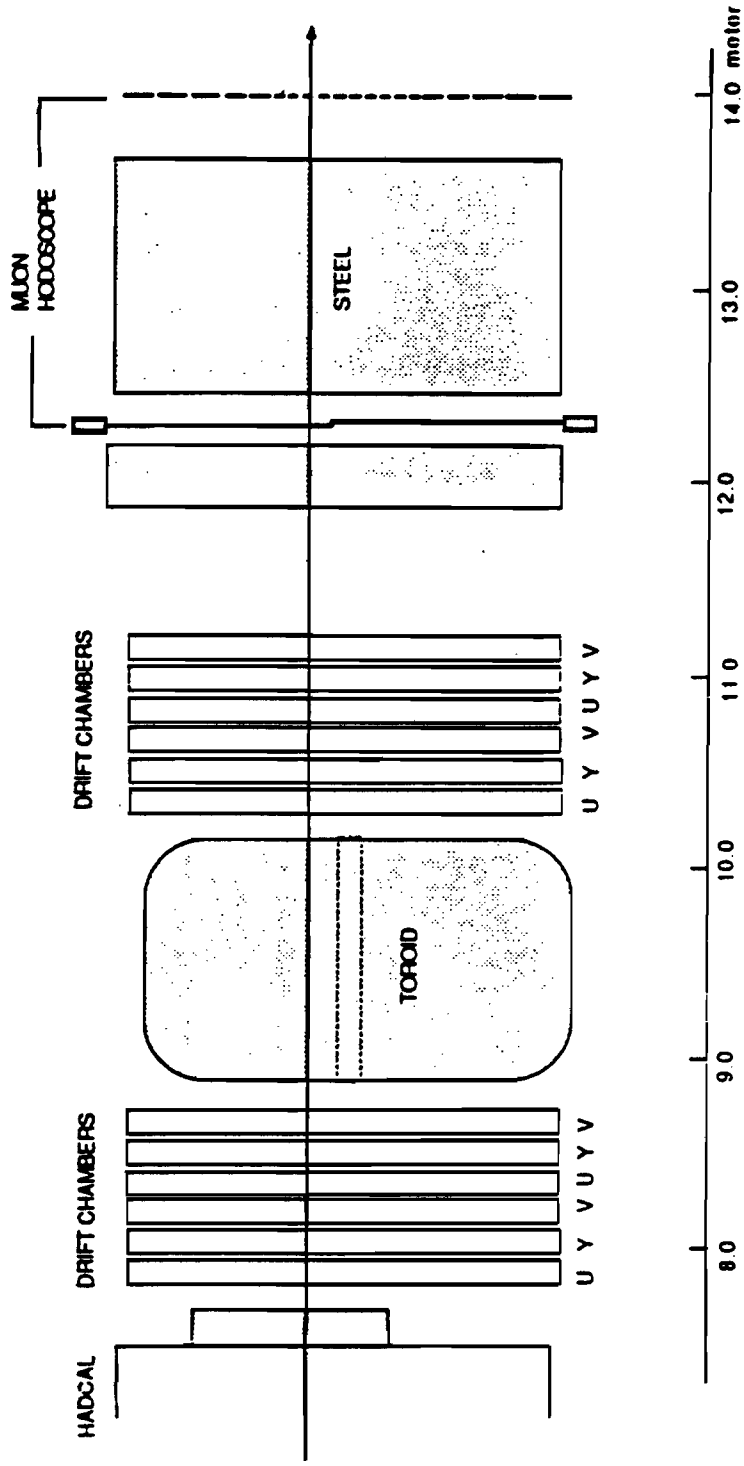

Figure 22: Plan view of the muon system.

3.6.1 Muon Spectrometer

After leaving the SDC's the particles encountered the time of flight counters, liquid argon calorimeter, hadron calorimeter, and ranging steel. The information provided by these systems was not used in this analysis. Particles that managed to get through the 8.77 interaction lengths of material in the calorimeters entered the muon spectrometer.

The muon spectrometer consisted of 12 drift chambers with a 3m x 3m area transverse to the beam axis. The chambers were arranged in three views, Y, U and V. The U and V views were set at $\pm 12^o$ with respect to the X-axis. Each chamber had two 1.6cm wide gaps, and the sense wires in the two gaps were offset to eliminate left/right ambiguity. Six chambers preceded the steel toroid magnet, representing 8.03 interaction lengths, and six chambers followed the magnet. The last drift chamber was just 11m from the emulsion target.

The chambers were operated initially with 50% argon 49.5% ethane and 0.5% ethanol gas mixture, for the later runs a 50% argon 50% ethane gas mixture was used.

Unexpected non-uniform electric fields caused by floating some of the shaping strips caused a non-linear drift velocity. The non-linear effects were determined by using a high momentum muon calibration beam. The final overall position resolution of 400 microns was achieved when properly accounting for the non-linear velocity on a cell by cell basis. Figure 23 plots the residuals for four of the muon drift chambers.

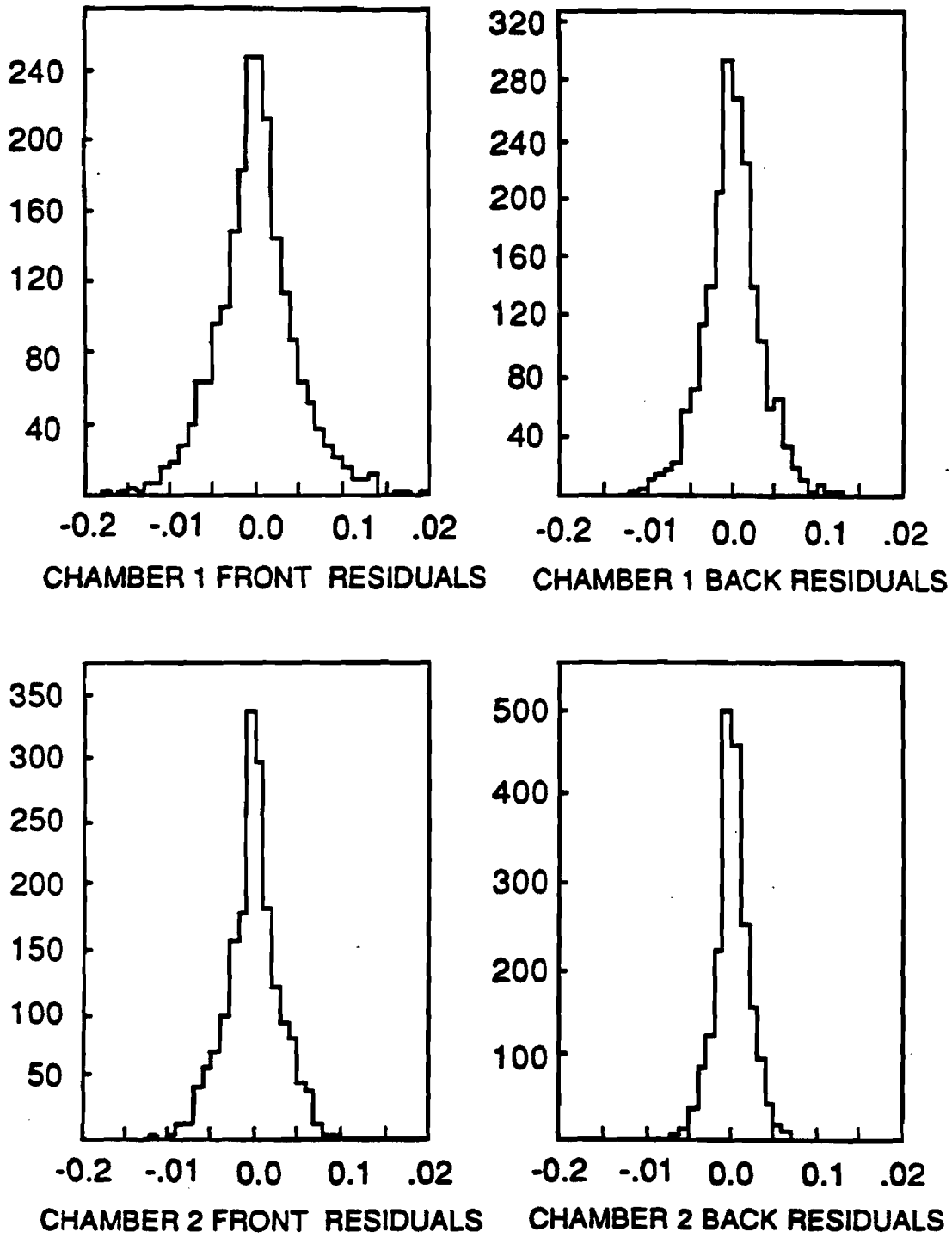

Figure 23: Position residuals for four of the cells in the muon drift chambers.

3.6.2 The Toroid

Sandwiched between the muon drift chambers was a toroidal steel magnet, 130cm thick and a radius of 180cm. The toroid consisted 8.03 interaction lengths of steel. In conjunction with tracking information provided by the muon drift chambers, the toroid provided an independent momentum measurement of the muon momentum. This momentum provided another constraint on the linkage of the muon track reconstructed by the muon system to its upstream track in the spectrometer drift chambers.

The field map of the toroid was generated with the POISSON program in the CERN program library. The results of the program agreed within 2% with hall probe measurements. The equation for the magnetic field of the toriod is:

$$B(r) = 22.196 - 0.040049r \quad 12 < r < 86 \tag{20}$$

$$B(r) = 21.037 - 0.024904r \quad 86 < r < 775 \tag{21}$$

The momentum equation is:

$$P = 0.03B(r)L/\theta \tag{22}$$

The resolution is:

$$\delta P/P = \sqrt{(0.19)^2 + (0.007p)^2} \tag{23}$$

- r = radius from center of magnet (cm)

- L= thickness traversed (cm)
- θ = angle deflection of the track (mradians)
- P = momentum in GeV/c

The magnetic field in the toroid was 19.5 $\pm$ 2.5 kilogauss and imparted a 0.76 GeV/c momentum kick to the muons.

The amount of ranging material preceding the muon system was not quite enough to contain the hadronic cascade caused by the incident hadrons. This hadron punch through swamped the six upstream muon drift chambers. The muon drift chambers were designed to operate in a low multiplicity environment. The front muon chambers were incapable of resolving the muon track in events with large hadron punch through.

Because of the hadronic punch through the events were divided into three types:

- Up-Down Muons: The muon track was successfully reconstructed in both sets of muon drift chambers. 57% of the events.
- Down Only Muons: Muon track information is available from the downstream chambers only. 38% of the events.
- No Muon: No muon track in the downstream chambers, 5% of the events. These events were later rejected by the offline analysis.

3.6.3 Muon Hodoscope

At the very end of the E653 spectrometer, 15m from the emulsion target, was the muon hodoscope. The muon hodoscope consisted of two sets of scintillation counters seperated

by ranging steel. The effective area of the counters was 360cm x 304cm and had an angular acceptance of +99 to -157 milliradians in dx/dz. And +142 to -99 milliradians in dy/dz. The front scintillators, MU_{Front} consisted of 36 horizontal counters logically 'or'ed together. The 40 back paddles were oriented vertical behind another 6.67 interaction lengths of steel and were also logically 'or'ed together. A particle was tagged as a muon if both MU_{Front} and MU_{Back} arrays fired in coincidence.

$$MU = \Sigma MU_{Front} \cdot \Sigma MU_{Back} \tag{24}$$

A particle had to traverse 26 interaction lengths of material to reach the MU_{Back} paddles.

The signal in the MU hodoscope was used to complete the trigger requirements discussed in the next section.

The efficiency of the muon hodoscope was 94%. This was determined by removing the muon requirement from the trigger. The number of events with both a muon track reconstructed in the MDC and a hit registering in the hodoscope was compared to the number of events with a reconstructed muon track.

3.7 The Trigger

The E653 trigger was the logical 'and' of three scintillator counter systems, the beam trigger counters, the interaction counter and the muon hodoscope. The beam trigger counters and the interaction counter are shown in Figure 24. The beam counters forced the incoming proton to be incident on the central regions of the silicon strip detectors and required that

the proton was not associated with any halo particles. The counter S_3 which was 5mm in diameter defined the beam position and also provided the start time for the time to digital converters discussed in the next chapter. The interaction counter was placed immediately after the emulsion stack and was 6.35mm thick. The signal from this counter was sent to a discriminator with the threshold set at the equivalent of 3 minimum ionizing particles. This counter required that an interaction had occurred in the emulsion, and produced at least three charged tracks.

The muon hodoscope, described in the previous section, completed the trigger.

The logical definition of the E653 trigger was

$$Trigger = Beam \cdot Interaction \cdot Muon \tag{25}$$

This was referred to as the $B \cdot I \cdot \mu$ data trigger.

The data trigger was vetoed by the data acquisition system if it was busy reading out a previous event or if the memory had insufficient space available for another event. The dead time was 25 to 30 %. Figure 25 shows the logical schematic of the Run I E653 trigger.

3.8 Data Acquisition

The job of the data acquisition system was to convert the analog information into binary numbers, digitization. This information must then be "packed" into a readable format and transcribed to a recording medium, magnetic tape or hard disk. The data acquisition

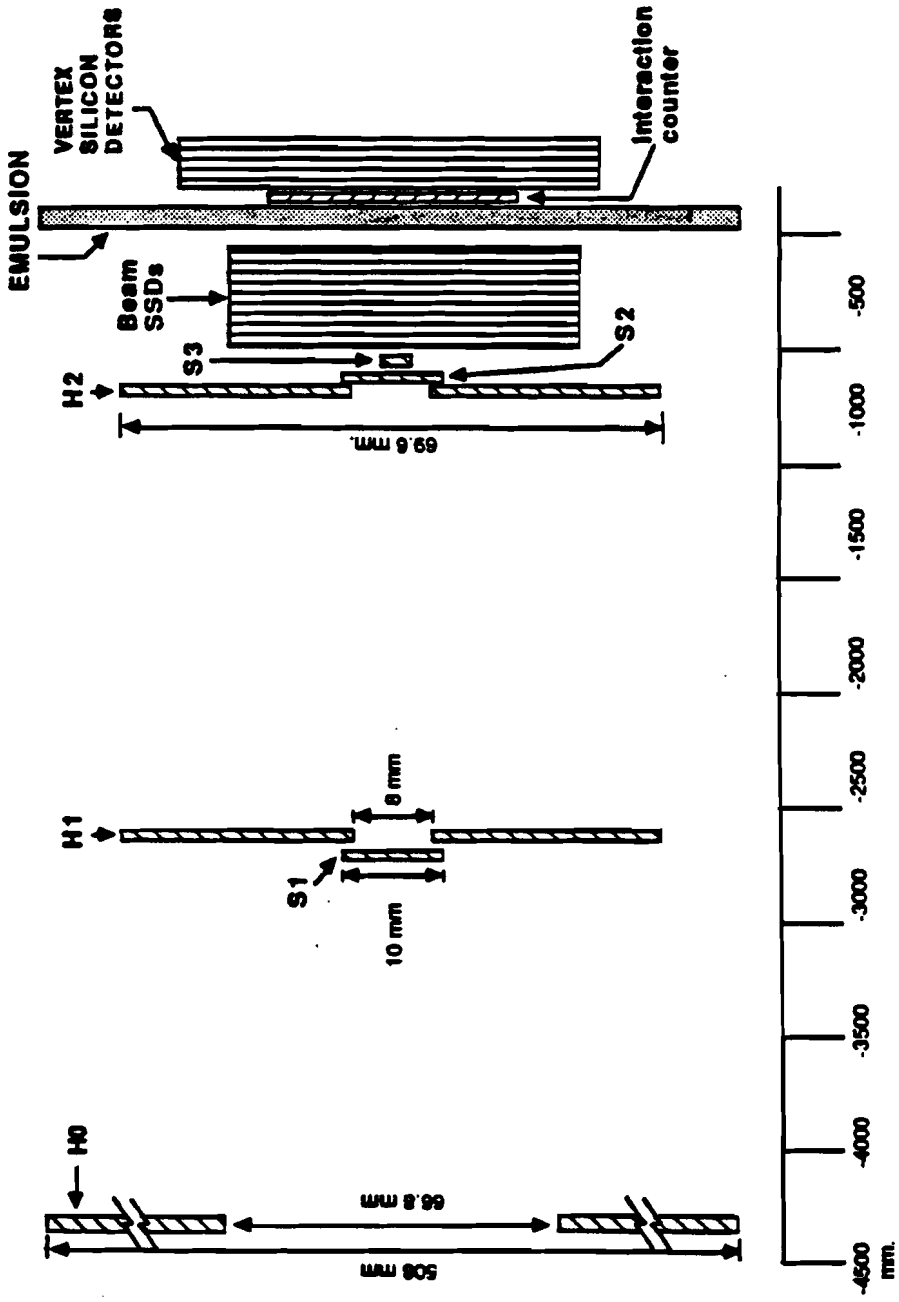

Figure 24: The beam and interactions counters of the E653 trigger system.

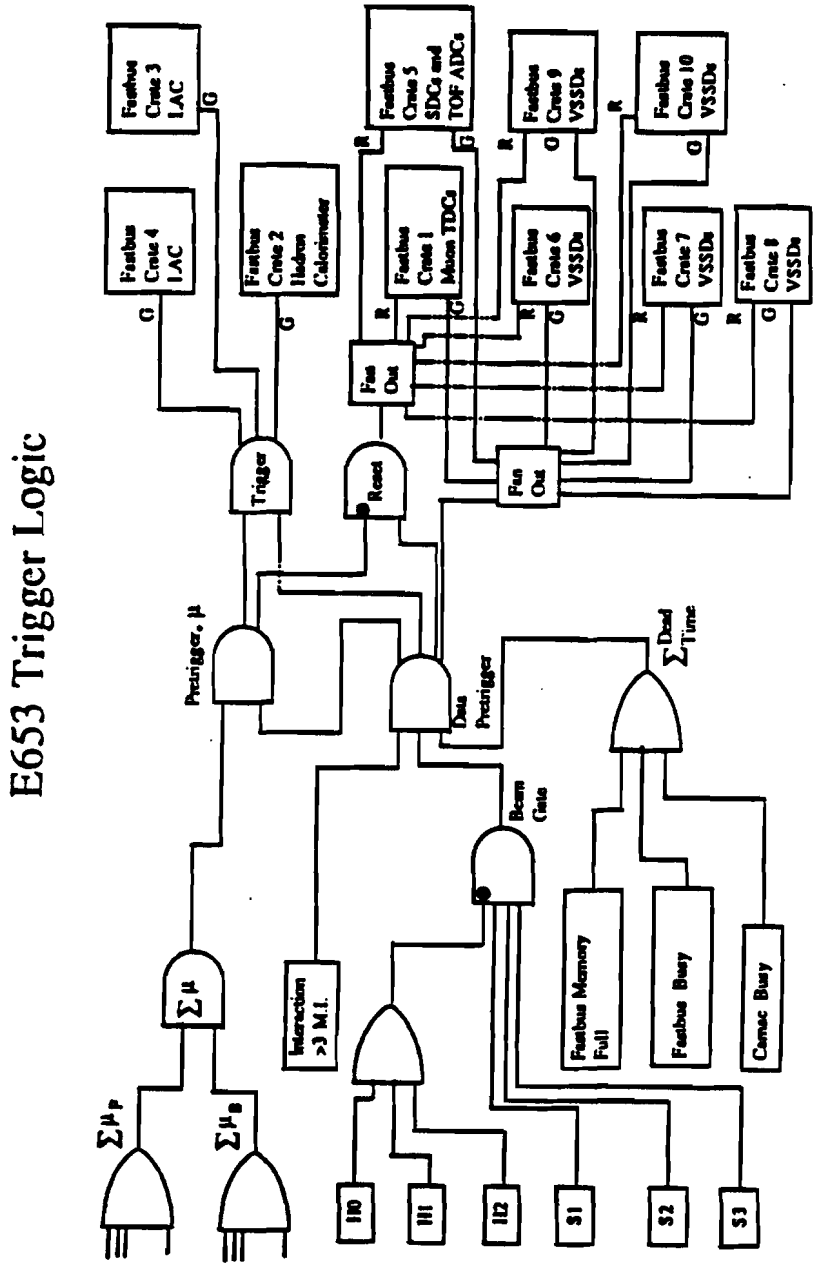

Figure 25: Logical schematic of the E653 trigger.

system used by E653 was the new FASTBUS data acquisition system.

E653 was the first experiment to use the new FASTBUS data acquisition system. Being the first meant that the majority of the devices had to be developed and debugged on the experimental floor. For example: a direct path connecting the FASTBUS system to a VAX computer architecture did not exist at the time of the first data run (1985). For this reason a rather convoluted FASTBUS to LSI 11/83 to VAX 11/750 data path had to be used. This data path and the inclusion of some CAMAC modules, because the FASTBUS equivalents were unavailable at the time, slowed the data rate to almost the same rate as the older CAMAC system. The compactness of FASTBUS modules compared to the older CAMAC modules made up for lack of a significant improvement in the data rate. This section will briefly review the data acquisition system (DA) and the ONLINE programs used to monitor the performance of the equipment during data taking.

3.8.1 Fastbus Hardware

The number of lines of information per experiment grows as the cost of associated electronics becomes tolerable. The problem becomes one of increasing the density of information. With this in mind the FASTBUS data acquisition system was developed. The FASTBUS system is a modular and crate system. Each crate would hold a programmable unit that controlled the crate and the data acquisition modules. Each data acquisition module had 96 channels of input and each crate could hold up to 22 data acquisition modules. The FASTBUS modules used were the first generation modules produced by Lecroy Research Services.

The Lecroy 1885 anolog to digital converter (ADC's) used by the silicon strip detectors

and calorimeters had bi-level readout capability. In the low range the sensitivity was 50 femtocoulombs/count and the high range sensitivity was 400 femtocoulombs/count. The total range of the ADC's was 200 picocoulombs for the low range and 1600 picocoulombs for the high range. Each ADC received a gate from the crate Calibration and Trigger Module (CAT). The timing and width of the gate was set by the experimenter.

The Lecroy 1879 time to digital converters (TDC's) were used by all the drift chamber systems to convert the time difference between the start pulse from trigger counter S_3 and the leading and trailing edges of the signal pulse from the drift chambers. The resolution of the TDC's depended on the clock frequency. The clock frequency was provided by the CAT module and was set at 334 MHz and had a bin width of 3 nanoseconds.

In addition to performing the digitization of the event information each FASTBUS crate had a CAT module which provided the ADC's and TDC's with the timing pulses (gates, and start and stop times). Each crate also had a programmable processor module (Lecroy 1821) that enabled online pedestal subtraction of the ADC signals. The digitized information from each crate was sent to its memory module, the Lecroy 1891. The memory module had multiple record capabilities and could hold up to one megabyte of information (two of the 1891's had four megabyte capabilities).

Once the event made it into the FASTBUS memory buffer the information was shipped to a LSI 11/73 via the DR11W interface. From there the information was shipped to the online computer, a VAX 11/750, and then onto magnetic tape. The online data acquisition system running on the VAX skimmed some of the events onto disk for online monitoring of the apparatus. The complete online data acquisition system data path is shown in Figure

26. With this configuration E653 was able to achieve a data rate of 122 Kilobytes/sec.

3.9 The 1985 Run and Overall Performance

The first run of the spectrometer just described started in May 1985 and was over by August of that year. The spectrometer had its quirks during this running period but for the most part the problems in keeping the hardware running were inconsequential to its final performance. Figure 27 shows the number of B·I·μ triggers written to tape during the 1985 run. Periods of down time were due to lack of beam to the experiment, not equipement failure.

After the data taking run the individual groups responsible for building the detectors attacked the problem of writing the software needed to do the event reconstruction. Various calibration data were taken during the run:

- High momentum μ tracks were used to calibrate and align the muon spectrometer, spectrometer drift chambers and vertex silicon strip detectors.
- Low momentum electron beams were used to calibrate the liquid argon calorimeter.
- Low momentum hadrons and high momentum muons were used to calibrate the hadron calorimeter.
- Conversion electrons from a parasitic γ beam were used to provide low momentum electrons used for additional LAC calibration.
- 800 GeV/c protons, no interaction target, were used to align the beam system, VSSD's,

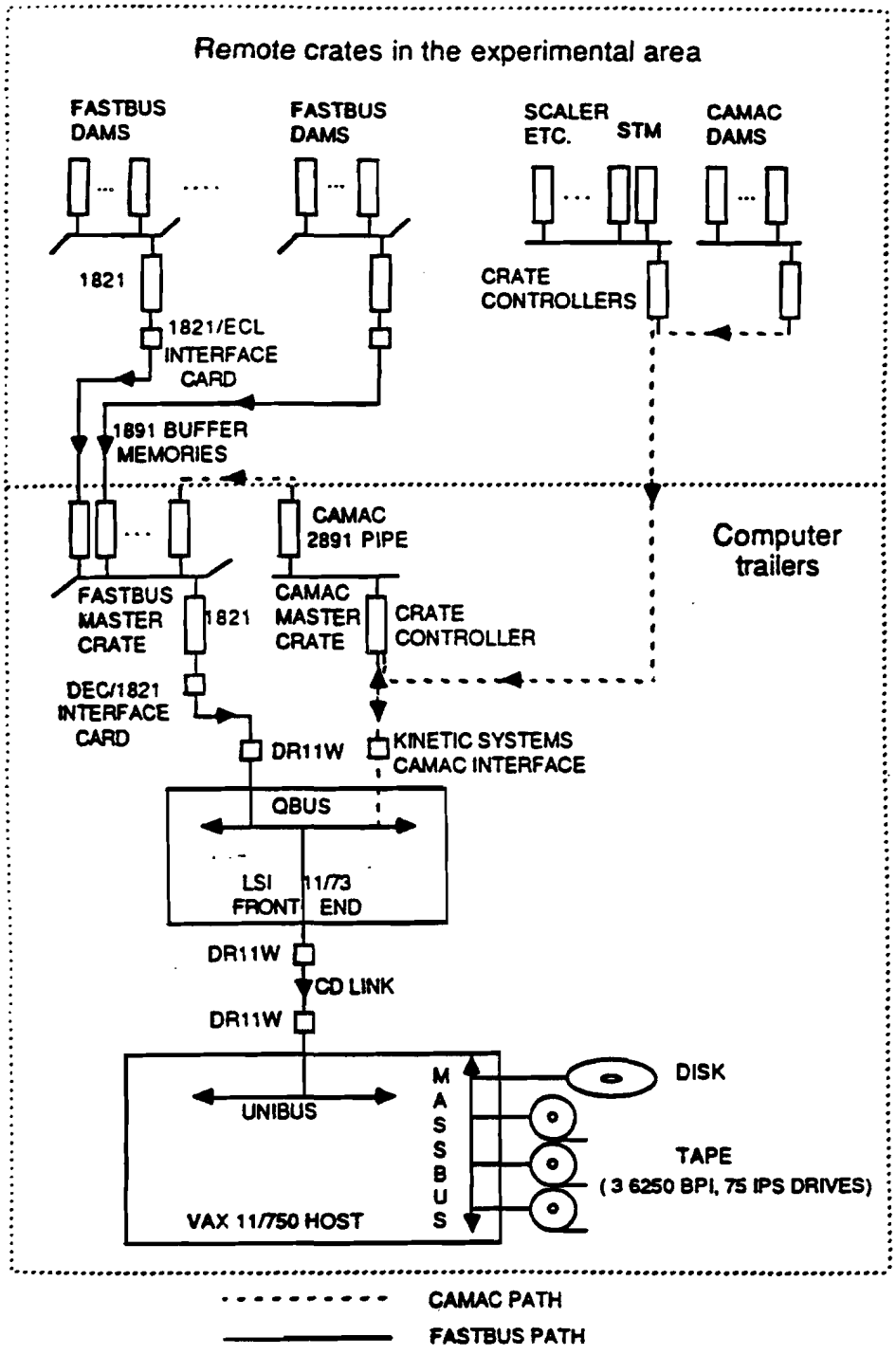

Figure 26: The event data path from the the FASTBUS crates to the magnetic tape.

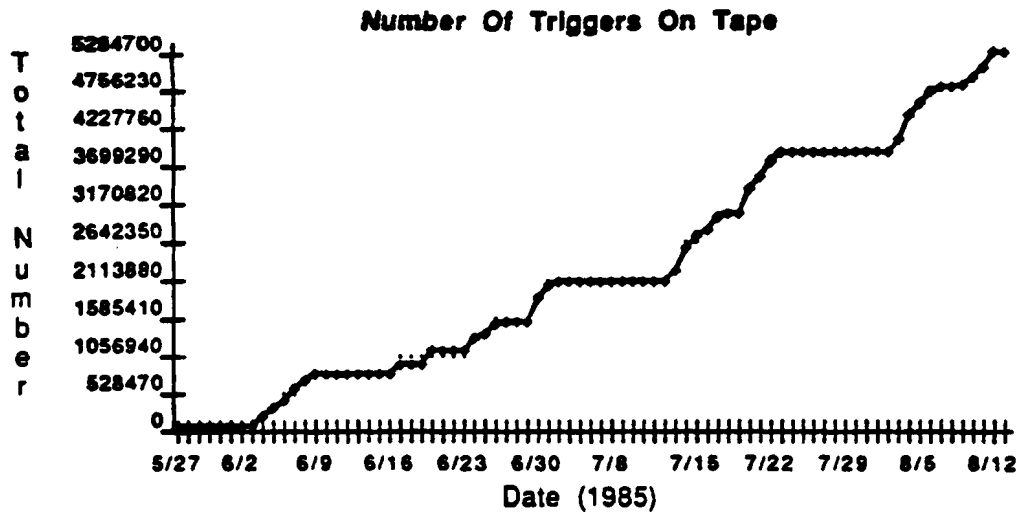

Figure 27: The integrated number of data triggers written to tape during the 1985 run of E653.

and SDC's.

B·I·μ data triggers were also used by the system for additional alignment and calibration.

The resolution achieved by the individual systems is listed in Table 5.

System	Quantity	Units	Resolution
Beam Drift Chambers	Position/plane	μm	150
Beam Silicon Strips	Position/plane	μm	17-35
Combined Beam System	Position at z=0	μm	10
	Angular	μrad	20
Emulsion	Position	μm	1-10
	Angular	milliradians	1-10
Vertex SSD	Position/plane	μm	8-24
	Position at z=0	μm	10
	Angular	μrad	70
Spectrometer Drift Chambers	Position/plane	μm	50-60
	Angular	μrad	35
Primary Vertex	Position(z)	μm	300-400
	Position(x,y)	μm	6-10
Secondary Vertex	Position(z)	μm	550-750
	Position(x,y)	μm	11-18
LAC	Position(x,y)	mm	1.2
	Energy(δE/E)	%	$(12/\sqrt{E})$+2.5
Muon Drift Chambers	Position(x,y)	μm	250-600
Charged Particle Spectrometer	Momentum	p in GeV/c	$\sqrt{(0.01)^2 + (0.00023p)^2}$
Muon Spectrometer	Momentum	p in GeV/c	$\sqrt{(0.19)^2 + (0.007p)^2}$

Table 5: The individual detector resolutions for the E653 spectrometer.

Chapter 4

Charm Selection

The motivation behind the E653 spectrometer was to collect a large number of unbiased heavy quark decays located in an emulsion target, by triggering on the semi-muonic decay of the partner quark. Emulsion scanning candidates were selected via offline spectrometer reconstruction. These events were visually scanned in the emulsion and decays with a topology consistent with charm were saved as charm candidates. The topological candidates went through a second pass of spectrometer reconstruction and decays consistent with charm decays were used for production analysis. This chapter describes the complete analysis chain used to obtain the charm pair sample, starting with the initial muon trigger.

4.1 E653 Trigger

Semi-leptonic decay rates of heavy quarks were predicted by theory to be large at the time E653 was being designed. Measurements just being made of this important decay mode

for charm mesons agreed with the predicted rates [25,63]. Hadronic interactions produce a charm event for every 1000 interactions, the muonic trigger enhanced the charm yield by eliminating background interactions that did not produce a high momentum muon.

E653 used a muon hodoscope positioned behind 5-GeV of ranging steel to trigger the data acquisition system (see Figure 22). The trigger also required a well defined beam particle and at least three charged particles leaving the emulsion (see Figure 24). These three requirements together formed (in E653 jargon) the B·I·μ trigger where the B stands for beam, I for interaction and μ for μ-hodoscope. The results for this work are from the $5*10^6$ B·I·μ triggers written to tape and the 35 liters of exposed emulsion during the 1985 run.

4.2 Event Reconstruction and Emulsion Predictions

The first stage of the offline analysis used the tracking information in the VSSD, SDC, and MDC to select charm events and to determine the location of the events in the emulsion block. Charm selection utilized the properties of the reconstructed trigger muon track; event location was determined by the reconstructed primary vertex position.

The trigger muon track had to be reconstructed in the muon drift chambers and it had to be linked to a track in the upstream tracking detectors. The linking was done at the mid-plane of the material between the SDC and the MDC systems. At this mid plane (Z= 710 cm) multiple scattering effects are minimized. The momentum measurement of the muon track in the MDC system and the upstream spectrometer had to agree in sign and

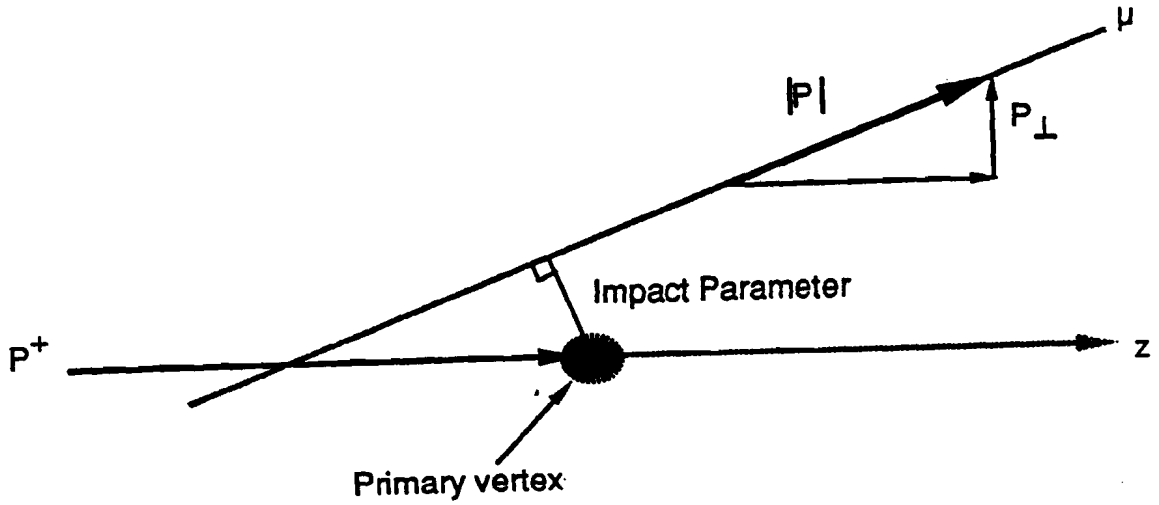

Figure 28: Cut variables applied the muon track to select events for emulsion scanning.

value. Muon tracks were required to have a $\chi^2 < 3.0$ for the link between the MDC and the SDC, and $\chi^2 < 5.0$ for the link between the SDC and VSSD. The linking efficiency between the MDC and SDC was 35%. The major source of the linking inefficiency was due to K or π decay into muons and the unexpectedly large amount of hadron punch through in the first six muon drift chambers. The linking requirements insured that the event contained a high quality reconstructed trigger muon and allowed the properties of the muon track to be used for event selection. Approximately, 35% of the events had a completely reconstructed trigger muon track.

The reconstructed tracks in the VSSD's that linked to the SDC's (so they had a momentum measurement) were used to form primary and secondary vertices. If a primary vertex was reconstructed inside the main emulsion block, the impact parameter of the muon with respect to the primary vertex position was determined (see Fig. 28).

The charm selection cuts used in this analysis are listed in Table 6. There were four sets of cuts involving several variables, but the most significant cuts involved the impact parameter of the μ (b_μ), the transverse momentum ($P_\perp$) of the μ with respect to the beam direction and a momentum cut on the muon (P_μ). The momentum cut ($P_\mu > 8.0$ GeV/c) on the muon track insured a high momentum muon which reduced the effects of multiple scattering in the emulsion and the in the ranging steel. The $P_\perp$ cut reduced the background from K or π decay into muons, only 5% of muons from prompt π's decays survived the cut while 40% of muonic charm decays survived [63]. This is due to the combination of a larger P_t available in charm decay and the fact that charm is produced with a higher average $P_\perp$. Kaons and pions from charm decay which subsequently decay into muons were not eliminated by this cut. This sample of mis-identified muonic charm decays represents about 14% of the muonic sample [62]. The impact parameter cut insured that the muon was not associated with primary interaction.

The three different classes of cuts were established with the muon cut variables (P_μ, b_μ, $P_{\perp\mu}$). These cuts are listed in Table 6. Type I events required a clean separation of the muon track from the primary vertex and a modest $P_\perp$ of the muon. Type III events represented the subset of Type I events in which the muon track was associated with a secondary decay vertex. The reconstructed muonic vertex allowed the cut values on $P_{\perp\mu}$ and b_μ to be reduced slightly to increase the yield. Possible beauty events, Type II events, were selected on the basis of the larger $P_\perp$ spectrum seen in Monte Carlo simulations of beauty decays. Type IV events were selected because of a reconstructed decay vertex outside the emulsion. These Type IV events were used for K_s^o momentum analysis and

Cut Variable	Class 3	Class 2	Class 1	Class 4
P_μ	8.00	8.00	8.00	0.00
$P_{\perp\mu}$ wrt Beam (GeV/ c)	0.20	0.80	0.250	0.00
Impact Parameter of Muon (microns)	50	100	100	0
$P_{hadrons}$(GeV/c)	5.0	0.0	0.0	0.0
Impact Parameter of Hadrons (microns)	0.050	0.0	0.0	0.0
Decay Length (mm)	2.0	0.0	0.0	0.0
Invariant Mass (GeV/c^2)	0.250	0.0	0.0	0.0

Table 6: Listing of the four different classes of cuts used in selecting events for emulsion scanning.

some preliminary charm analysis (done without emulsion information [28,29,30,31,33]). If an event passed Type I, II, and III cuts, the tracking and vertex information was sent to the emulsion scanners in Japan to scan the event.

Event loss during offline scan selection for a typical vertical emulsion module is listed in Table 7 taken from [30].

4.3 Emulsion Scanning

The two different emulsion modules, horizontal and vertical, had two different scanning techniques. The horizontal scanning was done mainly by human eye whereas the vertical scanning incorporated a sophisticated automated emulsion scanner. The automation of the vertical scanning increased the scanning rate. Since only 3 out of the 37 charm pairs came from the horizontal modules, the scanning technique used for the vertical modules will be

Number of Events Before Cut(s)	Cut(s) description	Percent of Events Cut
17450	Event is readable from tape and is within the fiducial volume	30.1
12093	Fully reconstructed muon	71.3
3469	No primary vertex reconstructed	1.0
3331	Z of primary upstream of the emulsion block	1.9
3268	Z of the primary downstream of the emulsion block	12.8
		# of events
2849	Class 1 cuts	116
	Class 2 cuts	23
	Class 3 cuts	105
	Class 4 cuts	113

Table 7: Typical emulsion scanning predictions for a vertical emulsion module.

discussed briefly.

4.3.1 Automated Scanning

The last plate of the vertical emulsion stack, the analysis plate, was measured by the automatic scanner. This scanner consists of a video image microscope with a computer driven stage. The movable stage had a position read-out with a 1μm accuracy. The focal length of the microscope is also controlled by the computer and was varied in 10μm intervals. The last emulsion plate has two 80 μm thick layers of emulsion, so there were 16 measurements corresponding to 16 different focal lengths. This allowed measurement of the track angle and position at exit of the emulsion. These angles and intercepts were then matched to tracks reconstructed by the VSSD's. Tracks that have matches were then projected onto

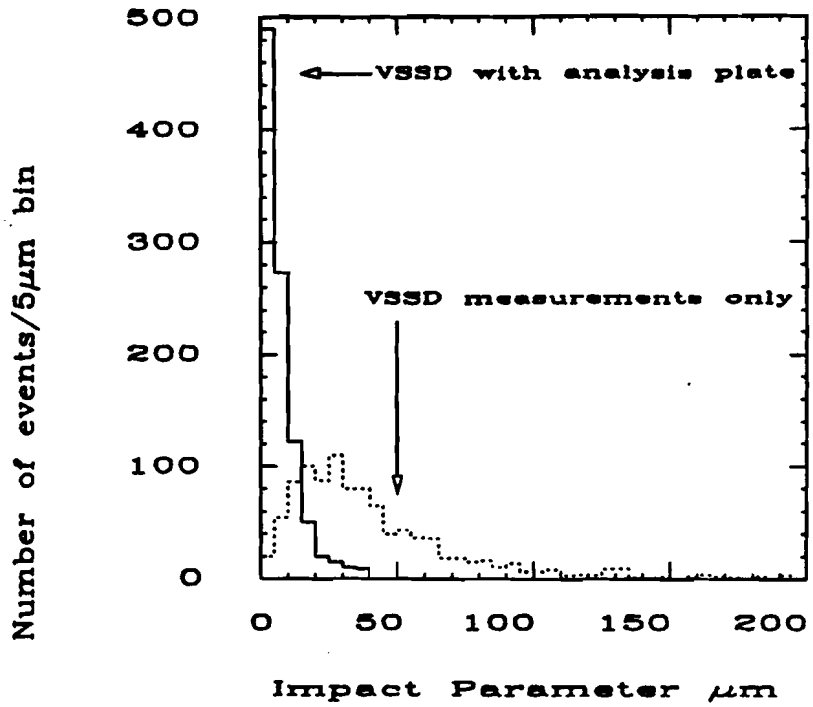

Figure 29: Impact paramter for tracks coming from the primary vertex.

the last emulsion pellicle of the main emulsion block.

The analysis plate information with its 1μm resolution allows a more precise measurement of the impact parameter of the tracks with respect to the primary position. Figure 29 shows the impact parameter for VSSD tracks confirmed to be coming from the primary vertex, the dotted line is for the impact parameter calculated using VSSD information only and the solid line is the recalculated impact parameter using the analysis plate information. With this improved impact parameter resolution events with the μ coming from the primary interaction were eliminated.

4.3.2 Graphic Analysis

Graphic analysis refers to using the primary vertex position and analysis plate track information to quickly eliminate uninteresting tracks from the primary vertex. A computer generated image of the analysis plate track segments and VSSD reconstructed tracks. Tracks were humanly matched between the emulsion and VSSD. Any tracks that were reconstructed by the VSSD's but not attached to the primary vertex were possible decay daughters. Events with a low P_t muon with respect to its parent, as measured in the emulsion, direction were rejected at this stage as $K \rightarrow \mu$ decays. If the event passed this graphic analysis the event was saved for complete emulsion scanning.

4.3.3 Decay Search

The decay search started by scanning back all tracks that had a match at the analysis plate but were not linked to the primary interaction. This search path ended at the source of the daughter track, either a decay vertex or a secondary interaction vertex. Tracks that originated at the primary but had no match at the analysis plate were scanned starting from the primary vertex until the track led to a decay vertex or the downstream edge of the emulsion. In this search charged decays that had failed reconstruction could be located. Table 8 lists the fraction of events that survived the different stages of emulsion scanning and the time needed to do the measurements.

Emulsion analysis	Percent that survived (%)	Length of time (minutes)
Fiducial volume cuts	80	0
Locate Primary Vertex	95	5
Analysis plate measurements reject if μ coming from primary	33	5-10
Graphic analysis reject low P_t μ's	50	10
Decay search reject if no decay is found	20	60
Totals	3.1	80-85

Table 8: Event through put for the different emulsion scanning stages.

4.3.4 Interaction Background

The emulsion technique also rejected secondary interactions in the emulsion block. The presence of heavily ionizing tracks indicative of nuclear breakup were clear indications of non-diffractive secondary interactions. All the events that were considered charm events went through a second pass of scanning. One of the objectives of this second scan was to search for the presence of 'blobs' that would indicate de-excitation of the nucleus after a diffractive interaction. This powerful technique provided a sample of charm decays with small backgrounds from interactions in the emulsion block.

4.4 Emulsion Charm Selection

Once a decay vertex was located in the emulsion the event had to pass several criteria for it to be saved as a charm candidate event. The muon track reconstructed by the spectrometer must not be linked to the primary vertex. Events with the reconstructed muon linked

to the primary vertex or linked to a secondary interaction vertex were rejected as charm candidates. The emulsion scanners must find at least one decay vertex in the emulsion. A vertex was a candidate decay vertex if the emulsion scanners did not see any heavily ionizing tracks from nuclear break up coming from the vertex.

If a decay candidate was found the event was completely measured by the emulsion scanners. The emulsion measurements started by matching spectrometer tracks to the primary vertex tracks. Unmatched primary tracks (emulsion tracks without a spectrometer match) were then scanned to the end of the emulsion block or until the track ended in a secondary vertex. Unmatched spectrometer tracks (spectrometer tracks without an emulsion match) were located at the downstream end of the emulsion block and scanned back towards the primary vertex until the source (neutral decay vertex) of the track was located. This process of following tracks down from the primary and scanning back towards the primary provided a way to pick up both charged and neutral decays. Upon completion of emulsion scanning, the topology of the emulsion decay vertices was known.

4.4.1 Decay Topologies

The decays were classified by the following topologies. First the decays were broken into two groups depending on whether the muon track was attached to the decay. Decays with attached μ's were called muonic decays since they involved the trigger μ. Decays without attached μ's were called unbiased or hadronic decays. The hadronic name was somewhat erroneous since this decay sample also had electron daughters or low momentum muon daughters about 20% of the time. In addition to the muon tag, the events were tagged by

the number of charged tracks or prong count and charge of the parent. Charged decays into one charged track were called C-1's and three charged tracks were called C-3's, five tracks were called C-5's. Neutral decays into two prongs were called V-2's and four prongs V-4's.

The notation that evolved in the E653 classification was to place a μ after the prong count if the decay had a muon daughter - a neutral V-2 decay with a tagged muon was written V-2μ. If there was no μ assignment, the decay was assumed to be hadronic - V-2 implies a hadronic V-2 decay.

At this point, the event was selected as a charm event by topology alone with some cuts on the muon track. The decays found in the emulsion were tagged visually and non-diffractive secondary interactions were eliminated by the presence of heavily ionizing tracks. The next stage in the analysis was to use the emulsion information to help the spectrometer tracking and to reconstruct the decays outside the emulsion block.

4.5 Refitting

If at least one decay was found in the emulsion, complete measurements were made by the emulsion scanners of all vertex positions in the emulsion and emulsion track slopes for tracks that did not have a spectrometer match. The emulsion scanners did not measure the track slope if the emulsion track had a spectrometer match since the spectrometer track slope resolution was 3 orders of magnitude better than the emulsion (See Table 5). Emulsion measurements were then used to guide the spectrometer track reconstruction. Specifically, emulsion track information was used to predict the track path through the VSSD's allowing

the VSSD's to use a more relaxed criterion to reconstruct tracks. Once all the emulsion tracks had been matched to spectrometer tracks, the reconstruction program then used the left over hits in the VSSD's to reconstruct tracks not matched to the emulsion tracks.

The unmatched spectrometer tracks were then used to form decay vertices outside the emulsion block. These vertices were called counter or computer vertices and formed another distinct topology of decays. Once a counter vertex was reconstructed, the unmatched emulsion tracks were checked to see if they pointed to the counter vertex position. A counter vertex was considered a good charm decay candidate if the sum of the charge tracks was 0 or ± 1 (there were some ± 2 or ± 3 vertices) and if it had (had not) an emulsion parent it was a charged (neutral) decay. The complete event topology was established at this point and the next step in charm selection was to use the momentum information of the linked tracks to determine if the decay was consistent with a charm decay. The emulsion scanners found 1205 events that contained a decay with a topology consistent with charm decay.

4.6 Final Charm Pair Sample

A progression of cuts was applied to the 1205 charm candidates found by the emulsion scanners to obtain a sample of charm pairs. These cuts are listed in Table 11 and are described in the following sections. Without particle identification, a set of cuts was developed that utilized the topological properties of charm pair events. The kinematic quantities of the decays were also used in the final cut to ensure that the decays were consistent with charm decays.

4.6.1 Level 1: A Muonic Vertex

The trigger muon was used not only to trigger the data acquisition system but was also used offline to select events for emulsion scanning. The understanding of the efficiencies for the analysis required that one of the charm decays had the trigger muon as a daughter. This requirement removed the serendipitous charm found by the emulsion scanners. These serendipitous events were initially kept by the emulsion scanners since there was a decay (non-muonic) found in the emulsion and it was hoped that the refitting procedure would reconstruct a partner muonic decay outside the emulsion. There were 344 events that failed this cut.

4.6.2 Level 2: Two or more decay vertices

A complete charm event must have two charm decays reconstructed. The level 2 cut checked the vertex list and saved only those events that had two or more decay vertices. At least one of the decays must reside in the main emulsion block, this allowed the analysis to use the visual power of the emulsion to check the decay vertex for nuclear break up indicative of a secondary interaction. A good "counter" vertex was required to have 2 or more charged daughters and to be located outside the main emulsion block. The counter vertex was also required to be a muonic vertex; the number of counter hadronic vertices reconstructed with a charge sum of $\pm$ 2 for V-2's and V-4's or $\pm$ 3 for C-3's demonstrated that the hadronic counter vertices were consistent with being all background (See section 5.4 for details). One of the decays must also be the muonic decay required in the previous cut level. There were 409 events that had at least two vertices that passed these cuts.

4.6.3 Level 3: Complete tracking

The decay daughters must be fully linked through the spectrometer to determine the momentum for the charged daughters. This tracking requirement allowed more sophisticated charm selection than just topological identification and allowed a momentum estimate (see Chapter 6) for the charm parent to be obtained. In addition to requiring complete tracking of the decay daughters, the cuts of the previous levels were still enforced, the event now consisted of at least two decay vertices which were fully reconstructed. At least one of the decays must be in the emulsion, and at least one of the decays must be a muonic decay. The number of fully reconstructed events with at least two vertices was 273.

4.6.4 Level 4: M_{min} Cuts

Without extensive particle identification the task of determining if a decay was consistent with a charm meson decay was not easy, but by relying on the strengths of the spectrometer (excellent vertex positions, momentum resolution, and muon identification) a parameter called M_{min} was developed which enabled charm event selection and background determination [24].

WHAT IS M_{min}?

The high resolution of the vertex positions (2μm) enabled the transverse momentum imbalance with respect to the charm parent to be well measured. This imbalance was called the missing P_t of the vertex and was the transverse momentum carried by the neutral daughters. The minimum mass associated with the decay was calculated by

assuming that the charged and neutral systems, in the rest frame of the D, were produced transverse to the boost direction and were assigned particles masses using the mass assignments described in Section 6.2.1. M_{vis} is the effective mass for the charged tracks and M_{neut} is the mass assignment for the neutral particle. The value M_{min} in equation 26 is identical to the value obtained by solving for the mass that yields only one solution from the 0-C equation for the decay hypothesis and for this historical reason it is call M_{min}.

$$M_{min} = (M_{vis}^2 + P_t^2)^{\frac{1}{2}} + (M_{neut}^2 + P_t^2)^{\frac{1}{2}} \tag{26}$$

The distributions for M_{min} depended on the topology in question and how many missing neutrals were involved. Single neutral decays had a M_{min} distribution that peaked at the charm mass whereas multiple neutral modes had a rounded distribution that peaked well below the nominal charm mass. For this analysis the decay branching ratios in Table 23 were used. Figure 30 shows the M_{min} distribution for C-1μ V-2μ and C-3μ charm decays, the solid curve shows the Monte Carlo distribution, and the dashed curve is for the data *before* any cuts were applied. Figure 31 shows the M_{min} distribution from the hadronic modes, C-1, V-2 and C-3. The M_{min} for each decay was required to be within topologically dependent bounds described below, the error (σ) on the measured value of M_{min} was used to allow all properly reconstructed charm decays to be accepted by these M_{min} cuts. The M.C. M_{min} curves are compared to the data M_{min} distributions in the following sections.

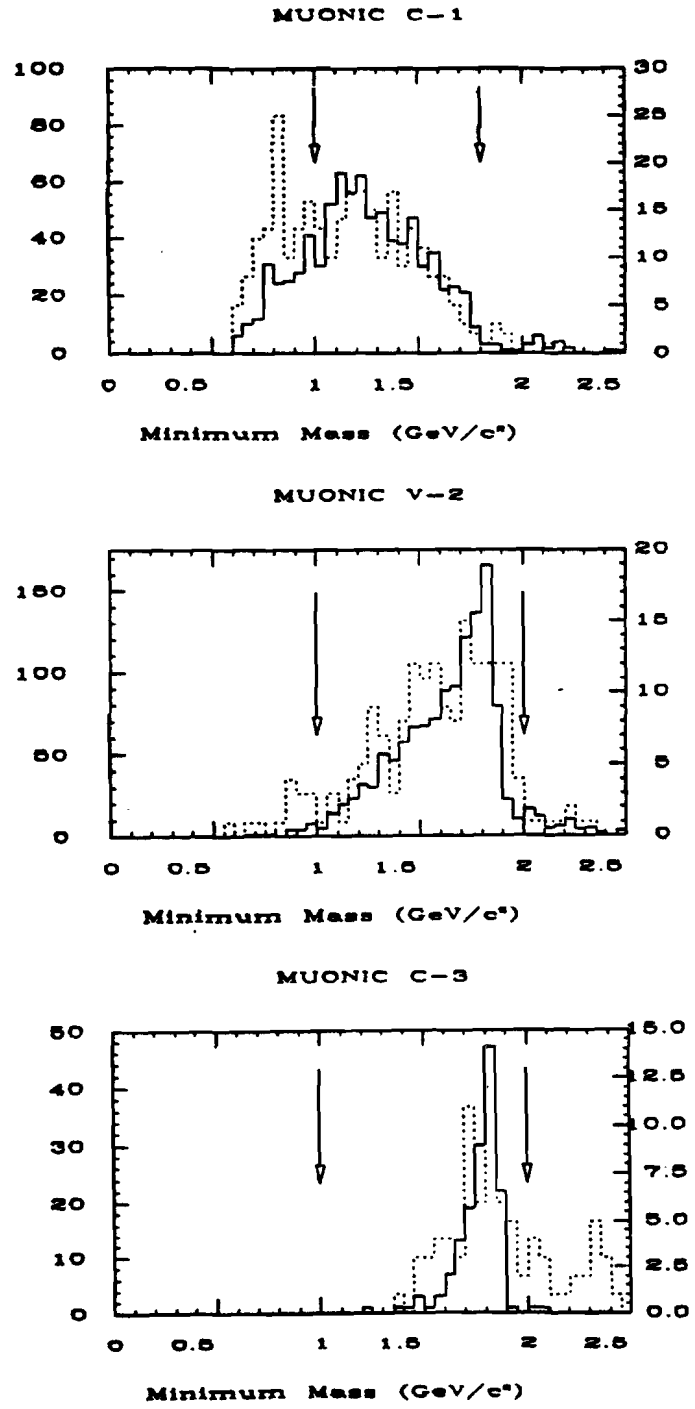

Figure 30: M_{min} distributions for muonic decays of D^o and D^+ mesons. The solid curve is for Monte Carlo and the dashed represents the data before any cuts. The arrows point to the upper and lower bounds on M_{min} required for a decay to be considered charm.

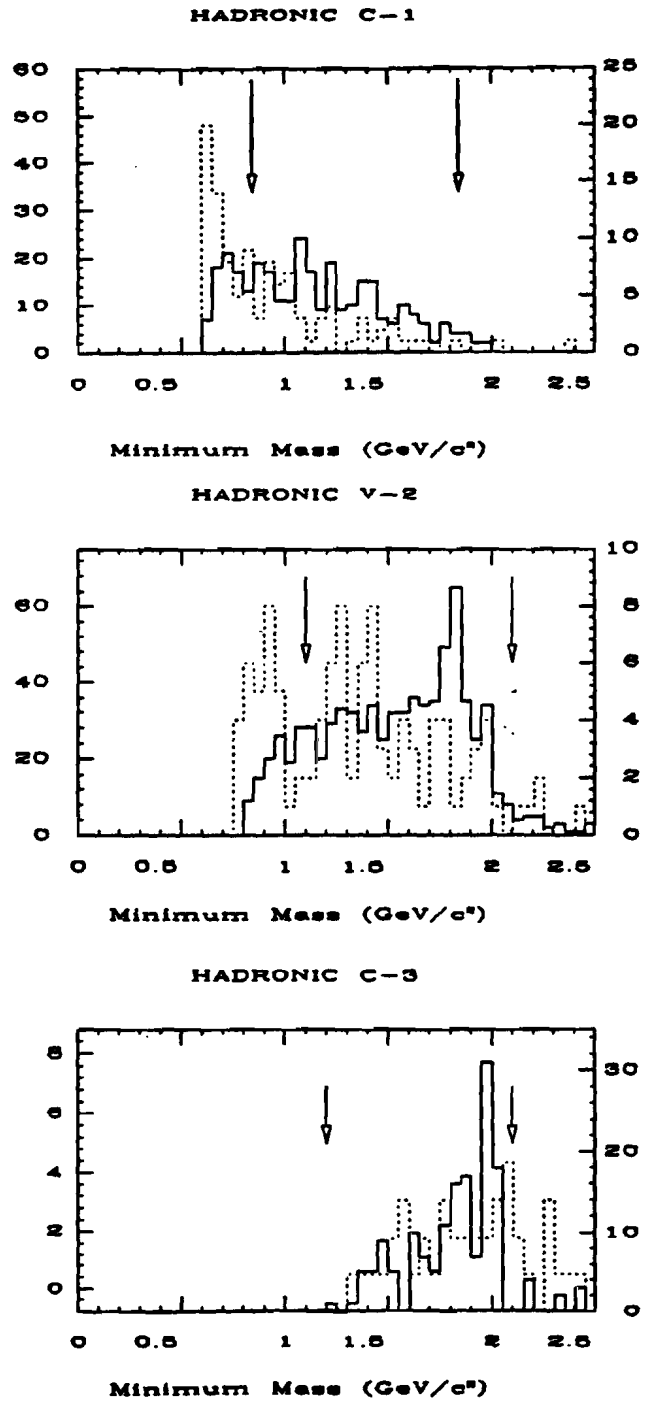

Figure 31: M_{min} distributions for non-muonic decays of D^o and D^+ mesons. The solid curve is for Monte Carlo and the dashed represents the data before any cuts. The arrows point to the upper and lower bounds on M_{min} required for a decay to be considered charm.

Muonic Kink Decays (C-1μ's)

The M_{min} for the muonic kink decays in the complete data sample agreed well with the Monte Carlo M_{min} at high M_{min}. The discrepancy at low M_{min} was due to $K^{\pm} \rightarrow \mu\nu$ decay. This strange background was eliminated by placing the low M_{min} cut at (1.0 -1σ) GeV/c^2 and by requiring the P_t of the μ with respect to the parent direction to be greater than 0.250 GeV/c.

Muonic V-2 Decays

The raw M_{min} distribution for the V-2μ's agreed very well with the Monte Carlo. The small bump at low M_{min} (at 0.9 GeV/c^2) was due to $K_s^o \rightarrow \pi\pi$ decays where one of the π's then decayed into a μ which triggered the apparatus. These strange decays were eliminated by placing the lower M_{min} cut at (1.0 -1σ) GeV/c^2 and requiring one of the decay daughters to have a P_t with respect to the parent direction of greater then 0.250 GeV/c^2 and by also explicitly cutting on the $\pi\pi$ mass of the vertex (See Table 9).

Muonic C-3 Decays

The high M_{min} tail in the C-3μ M_{min} data distribution was due to two possible sources:

- Charm background: Hadronic feed through where one of the K's or π's from a $D^{\pm}$ decay subsequently decayed into a μ which triggered the apparatus and was reconstructed by the spectrometer.

- Non-charm background: Diffractive interactions which can not be flagged as secondary interactions by the emulsion scanners.

These two sources of background are explained in more detail in the following chapter on background determination in the charm sample. Muonic tridents with high M_{min} can be attributed to mis-identified hadronic charm decays and were included in the sample by placing the upper M_{min} at (2.0 $+2\sigma$) GeV/c^2.

Hadronic C-1's

The M_{min} distribution for the hadronic C-1's in the complete data sample showed a strong peaking at low M_{min}. The peak at low M_{min} was due to small angle scattering in the emulsion. The low M_{min} kinks were eliminated by placing the lower cut on M_{min} at (0.80 -1σ) GeV/c^2, and a P_t >0.250 GeV/c cut on the missing P_t of the vertex.

Hadronic V-2's

The hadronic V-2's were contaminated predominantly by three sources of background: K_s^o and Λ^o decays and γ conversions. These sources of background appeared at the low end of M_{min} distribution and were eliminated from the charm pair sample by placing the M_{min} cut at (1.1 - σ) GeV/c^2 and by explicitly cutting on $M_{\pi\pi}$ of the decay (see Table 9).

Hadronic C-3 Decays

The M_{min} distribution for the hadronic C-3's had the interesting attribute of peaking at 2.0 GeV/c^2 instead of at the nominal charm mass (1.867 GeV/c^2). This over shoot of the

Lower Bound GeV/c^2		Upper Bound GeV/c^2
0.310	$< M_{\pi\pi} <$	0.490
0.504	$< M_{\pi\pi}$	

Table 9: Allowed range for $M_{\pi\pi}$ of neutral V-2 decays.

charm mass was due to the all charged mode of $D^+ \rightarrow K^-\pi^+\pi^+$. For this reason the upper M_{min} cut was placed at $(2.1 + 2\sigma)$ GeV/c^2 to include as many of the high M_{min} decays as possible.

Hadronic V-4 Decays

There were no cuts on the M_{min} for the neutral V-4 decays found in the emulsion. The hadronic V-4's represented a very clean sample since there is no source for strange contamination and the neutral diffractive background was very low.

Table 10 lists the allowed ranges for M_{min} by topology - if a decay had an acceptable M_{min} it was considered a charm candidate.

4.6.5 Level 5: Multiprong-Multiprong Charm pairs

The momentum estimator, to be described in Chapter 6, worked for all topologies but the resolution of the estimate became poor when most of the parent momentum was carried away by neutral daughters. The study of the kinematic distributions for the charm pair sample required the momentum of the two charm parents to be known with some

Topology	Lower Bound on M_{min} (GeV/c^2)	Upper Bound on M_{min} (GeV/c^2)
C-1 Hadronic	0.80 - 1σ	1.84 + 2σ
C-1 Muonic	1.0 - 1σ	1.80 + 2σ
V-2 Hadronic	1.1 - 1σ	1.95 + 2σ
V-2 Muonic	1.0 - 1σ	1.87 + 2σ
C-3 Hadronic	1.2 - 1σ	2.10 + 2σ
C-3 Muonic	1.0 - 1σ	2.00 + 2σ
V-4 Hadronic	No cuts	No cuts

Table 10: M_{min} cut values for the different topologies. The sigma is the measured error on the M_{min} for the decay.

Cut Level	Type of Cut	Number of Events that passed
-1	Type 1,2,3 events selected for emulsion scanning	56283
0	Events with charm decay candidates found by emulsion scanners	1205
1	μ track attached to a decay vertex	861
2	At least two decay vertices / at least one in the emulsion at least one muonic no counter C-1's, C-1μ, V-2's, C-3's	409
3	At least two decay vertices with complete tracking / at least one muonic / at least one in the emulsion	273
4	M_{min} Cuts C-1's,C-1μ's allowed in sample	95
5	Fully reconstructed multiprong-multiprong charm pairs	37

Table 11: Succession of cuts applied to the charm candidate sample.

Hadronic → Muonic ↓	V-2	C-3	V-4
V-2μ	12	3	4
C-3μ	3	2	1

Table 12: Emulsion-emulsion charm pair topologies in the final charm pair sample.

Emulsion → Counter ↓	V-2	V-2μ	C-3	C-3μ	V-4
V-2μ	1	1	5		3
C-3μ	1		1		

Table 13: Emulsion-counter charm pair topologies in the final charm pair sample.

accuracy for the momentum of the charm pair to be determined. For this reason the final charm pair sample used for kinematic study involved only those events with both charm mesons decaying into two or more charged particles. This final cut leaves 37 multiprong-multiprong charm pair events. Table 12 lists the topology of the 25 emulsion-emulsion events in the final 37 charm pairs and Table 13 lists the topology for the 12 emulsion-counter charm pairs.

Chapter 5

Backgrounds

5.1 Introduction

The charm pair event selection described in the previous chapter eliminated vertices if they were not fully reconstructed or if their M_{min} was inconsistent with charm decay. The cuts did not eliminate reconstructed background that had an acceptable value of M_{min}. This chapter will study how many of the decays and events in the charm pair sample were attributed to non-charm vertices and reconstruction errors. A source of non-charm vertices was diffractive interactions in the emulsion that can not be tagged by the presence of heavily ionizing tracks in the emulsion. Reconstruction errors were from two sources, track matching between the emulsion and spectrometer, and errors in the counter vertex reconstruction. The background from these two sources will be calculated in this chapter and shown to be small.

Topology	Found Non-Diffractive	Scaled Diffractive
C-1	18	5.0 ± 1.2
C-1μ	16	4.5 ± 1.1
V-2	6	1.68 ± 0.69
V-2μ	5	1.40 ± 0.63
C-3	2	0.56 ± 0.39
C-3μ	6	1.68 ± 0.69
V-4	4	1.12 ± 0.56
TOTAL	57	15.9 ± 2.11

Table 14: The number of non-diffractive vertices with all light shower tracks match to the spectrometer, scaled to yield an estimate of the diffractive background in the complete data set.

5.2 Diffractive Background

The amount of diffractive interaction background was estimated by requesting from the emulsion scanners the number of non-diffractive neutral interactions in which light shower tracks were produced in addition to the heavily ionizing nuclear break up tracks indicative of non-diffractive interactions. Non-diffractive interactions that have the light shower tracks matched to the spectrometer were taken to reflect the number of diffractive interactions matched. The non-diffractive interactions was scaled by the ratio of diffractive to non-diffractive interactions seen in the emulsion (using white stars), i.e. 10%. Table 14 list the number of non-diffractive interactions found in 10,711 emulsion scan events by the topology reflected by the light shower tracks. The found non-diffractive events must be scaled up by 2.8 since the information listed does not include the complete date set. The scaled diffractive numbers represent the total number of diffractive events in the entire data set. The final amount of diffractive background was calculated assuming a

Topology	Total Number of Decays	Total Diffractive Background	Decays at Level 4	Diffractive Background at Level 4	Decays at Level 5	Diffractive Background at Level 5
C-1	140	5.04 ± 1.19	30	1.08 ± 0.26	X	X
C-1μ	273	4.48 ± 1.12	33	0.54 ± 0.14	X	X
V-2	92	1.68 ± 0.69	29	0.53 ± 0.22	17	0.31 ± 0.13
V-2μ	179	1.40 ± 0.63	36	0.28 ± 0.13	20	0.16 ± 0.07
C-3	44	0.56 ± 0.39	17	0.22 ± 0.15	11	0.14 ± 0.10
C-3μ	100	1.68 ± 0.69	9	0.15 ± 0.06	6	0.10 ± 0.04
V-4	23	1.12 ± 0.56	13	0.63 ± 0.32	7	0.43 ± 0.22
TOTAL	851	15.9 ± 2.11	167	3.43 ± 0.53	61	1.14 ± 0.29

Table 15: Diffractive background estimates in the complete data set and the charm pair data set at the last two stages of charm pair selection.

constant percentage of diffractive background. This assumption leads to a very conservative estimate for the diffractive background.

The emulsion scanners have checked each decay vertex in the decay sample for associated 'blobs' at the decays. These 'blobs' indicate de-excitation of a nucleus after a diffractive interaction. Decays with 'blobs' attached to the decay vertex were removed from the charm candidate list. However the efficiency for finding these diffractive interactions was not determined and we are forced to use the best esitmate quoted in the Table 15. Assuming a constant percentage of background throughout the charm selection process implies that the charm selection process does nothing to enhance the charm signal. Discussion of sign correlations in the next chapter will show that this is not true. Table 15 lists the number of decays for each emulsion topology for the entire data set and for the events in the charm pair sample at level 4 and 5 of the selection process.

The diffractive background in the final data set is on the order of one event. The study of the charge correlations in the charm pair events is another way to study the diffractive

background in the charged decays.

5.3 Wrong Sign Charged Background

The reconstructed muon track tagged the charm species produced in the event. Comparing the sign of the charged decays with the charm species determined by the μ sign in the event allowed the background from the non-charm vertices to be estimated. Figure 32 shows pictorially the definitions described below. Although decays with only one charged daughter (kinks) were cut from the final data set, they provided some insight as to the performance of the charm cuts in reducing background and are described in detail. There are three possible sources for these wrong sign decays.

- The track matching or vertex reconstruction problems.
- Hadronic charm decay where the K subsequently decays via, $K \rightarrow \mu \nu$, and is reconstructed by the spectrometer.
- Non-charm vertices, diffractive background.

5.3.1 Hadronic Kinks (C-1's)

A hadronic kink (C-1) was consistent with charm decay if it had the opposite charge to the muon in the event. The hadronic kinks were divided into right sign/wrong sign, emulsion vertex/counter vertex and kinks with a P_t <0.250 GeV/c or P_t >0.250 GeV/c. Evidence that low P_t kinks were inconsistent with a charm hypothesis was seen by

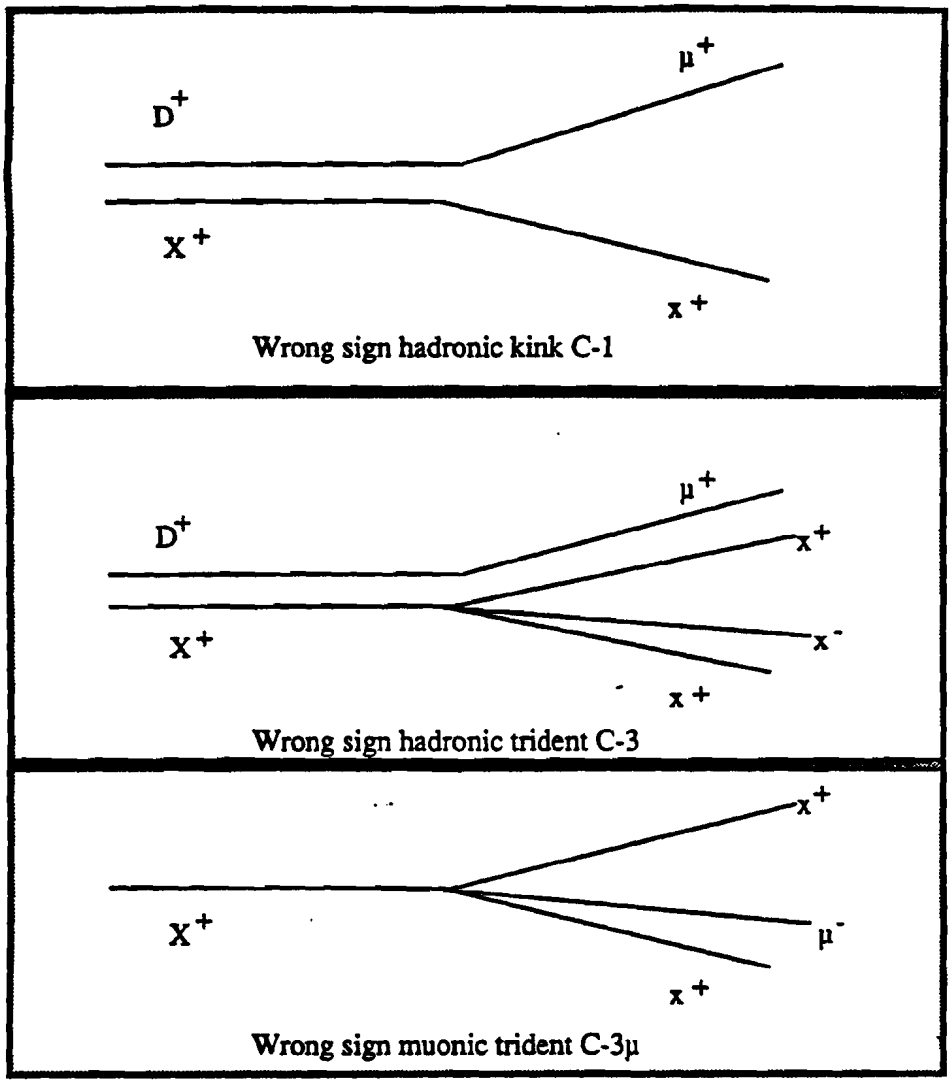

Figure 32: Wrong sign μ events used to estimate charge background.

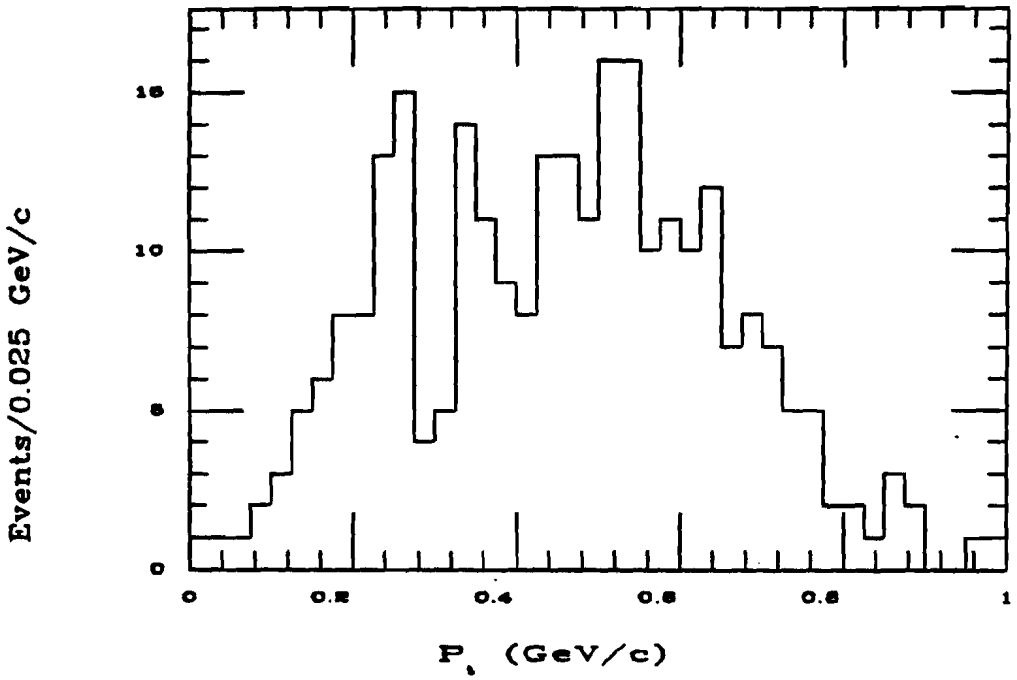

Figure 33: P_t distribution for right sign C-1's found in the emulsion.

comparing the P_t spectrum for the right sign and wrong sign hadronic C-1's found in the emulsion (Figure 33 and 34). The wrong sign spectrum had a much lower P_t distribution than the right sign kinks indicative of small angle scattering in the emulsion. The difference between the two P_t distributions also gave one confidence that the μ in the event was associated with charm decay. Any kinks, hadronic or muonic, had to have a $P_t > 0.250 GeV/c$ for it to be counted as a charm candidate.

The background in the right sign kinks was taken to be the number of wrong sign kinks for the type of kink in question. Table 16 contains the results from the complete data set. From Table 16 we see that all the counter hadronic kinks, regardless of P_t, were consistent with being all background. All counter kinks were rejected as charm candidates. Emulsion kinks with a $Pt > 0.250 GeV/c$ with the right sign have about 24% background. The number of wrong sign emulsion kinks at Level 4 is 3 events out of 33 decays, thus the

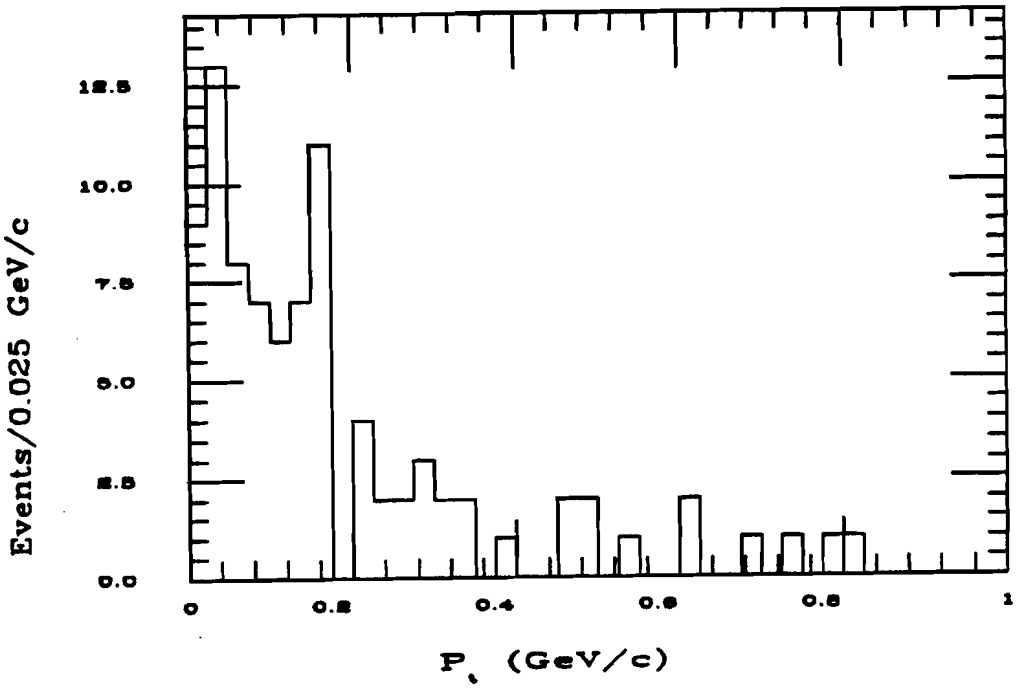

Figure 34: P_t distribution for wrong sign C-1's found in the emulsion.

background in the hadronic kinks was reduced by more than a factor of two in the charm selection process.

5.3.2 Hadronic Tridents (C-3's)

The sign of a hadronic trident was also required to be opposite the sign of the μ for the event to be consistent with a charm pair event. Table 17 shows the right sign/wrong sign break down for the hadronic tridents for the entire charm sample. Hadronic C-3's found by the emulsion scanners were consistent with charm decay. The hadronic counter tridents show the same level of background as the hadronic kinks. It is for this reason that counter hadronic tridents were eliminated from the charm sample. The final charm sample contained 11 right sign hadronic tridents located in the emulsion with no wrong sign tridents passing the selection cuts.

Kink	Right Sign	Wrong Sign	Background
Emulsion kinks with $Pt < 0.250GeV$	63	67	106%
Emulsion kinks with $Pt > 0.250GeV$	46	11	24%
Counter kinks with $Pt < 0.250GeV$	10	10	100%
Counter kinks with $Pt > 0.250GeV$	6	4	67%

Table 16: Sign correlations in hadronic kinks with respect to the μ in the event. Right sign kinks had the opposite sign of the muon sign in the event.

Vertex Type	Total	Right Sign	Wrong Sign	Background
C-3 emulsion	36	33	3	11%
C-3 counter	5	3	2	66%

Table 17: Sign correlation for hadronic tridents (C-3's) with respect to the μ in the event. Right sign tridents have the opposite charge sum of the muon charge in the event.

5.3.3 Muonic Tridents (C-3μ's)

A trident with a muon daughter (C-3μ) had the same sign as the daughter muon if it was from charm decay. Table 18 is a listing of the number of wrong sign/right sign C-3μ's in the complete data sample. The emulsion decays had a higher background than the counter decays due to the amount of charged secondary interactions that occurred in the emulsion. The final charm pair sample did not contain any wrong sign muonic tridents. The Level 4 charm pair sample had one emulsion C-3μ.

All the charged topologies (C-1,C-3 and C-3μ) showed a reduction in the number of wrong sign vertices to right sign vertices as the charm selection cuts became more stringent.

Vertex Type	Total	Right Sign	Wrong Sign	Background
C-3μ emulsion	86	65	21	32%
C-3μ counter	12	12	0	0%

Table 18: Sign correlations for muonic tridents. Right sign means the sign of the muon equals the charge sum of the vertex.

Topology	Q=±0	Q=±1	Q=±2	Q=±3
V-2 emulsion	76		6	
V-2μ emulsion	157		7	
C-3 emulsion		33		2
C-3μ emulsion		65		3
V-4 emulsion	19		2	
V-2 counter	36		31	
V-2μ counter	41		16	
C-3 counter		3		3
C-3μ counter		12		2

Table 19: Wrong charge vertices in the complete data set.

5.4 Wrong charge vertices

The track mismatch errors and vertex reconstruction error exhibit themselves in vertices that have a charge sum greater than one. The number of Q= ± 2 V-2's, Q= ± 3 C-3's and Q= ± 2 V-4's reflects the number of background vertices in the charm sample that had an acceptable charge sum. Table 19 lists the number of wrong charge vertices for the different topologies in the complete data set. The hadronic counter vertices show an unacceptable amount of background and were eliminated from the charm pair analysis at cut Level 2. The Level 4 charm pair sample had 9 wrong charge vertices and 124 vertices with a Q= 0 or ± 1. The Q=± 1 vertices had to have a sign consistent with the muon sign in the event. This 8% background was reduced to one decay out of 74 decays in the final sample.

Topology	Q=±0	Q=±1	Q=±2	Q=±3
V-2 emulsion	28		1	
V-2μ emulsion	37		2	
C-3 emulsion		17		0
C-3μ emulsion		9		0
V-4 emulsion	13		2	
V-2μ counter	16		4	
C-3μ counter		4		0

Table 20: Wrong charge vertices in the Level 4 charm pairs.

Topology	Q=±0	Q=±1	Q=±2	Q=±3
V-2 emulsion	21		1	
V-2μ emulsion	20		0	
C-3 emulsion		11		0
C-3μ emulsion		6		0
V-4 emulsion	7		0	
V-2μ counter	10		0	
C-3μ counter		2		0

Table 21: Wrong charge vertices in the Level 5 charm pairs.

Background	Complete Data Set		Level 4		Level 5	
	Signal + Background	Background	Signal + Background	Background	Signal + Background	Background
Diffractive Interactions in Emulsion	851	15.9 ± 2.11	167	3.43 ± 0.53	61	1.14 ± 0.28
Wrong sign analysis	165	41 ± 6.4	63	4 ± 2.0	19	$0.0^{+1.0}_{-0.0}$
Wrong charge analysis	442	83 ± 9.1	124	9 ± 3	62	1.0 ± 1.0
Total			198	16.4 ± 3.6	74	2.1 ± 1.0

Table 22: Total Background for the charm pairs. The diffractive interaction background is lower than measured due to additional emulsion measurements.

5.5 Final Background Determination

The previous sections described how the backgrounds were determined for the different topologies and gave results based on looking at the entire data sample and the charm pair samples of Level 4 and 5. Table 22 shows the the final total background for the three different sources just described. The total non-charm background is estimated to be 2.1 ± 1.0 events, this estimate is conservative since it scales the diffractive background from the complete data set. Improvement of signal to background ratios at different cut levels demonstrates that the charm pair selection reduced the background to signal ratio, but no quantitative means were available to account for this reduction. The value of 2.1 ± 1.0 background events is taken to be an upper limit and is low enough to permit data analysis on the complete charm pair data set without background subtraction.

Chapter 6

Momentum Estimation

6.1 Introduction

The study of the production characteristics of charm pairs requires that the momentum of each of the two charm particles be known. Adding the two momentum vectors of the individual charm, yields the momentum for the charm pair system so the production kinematics and dynamics of the charm pair can be measured. The μ trigger used in E653 forced at least one of the two charm decays in an event to be semi-leptonic and therefore to have an undetected neutrino. The partner decay was unbiased, other than by dynamic production correlations, and had a neutral daughter $\sim 90\%$ of the time. Although hadronic neutrals (π^o's,K^o's...) could be detected using calorimeters, the efficiency for detecting these neutrals strongly limited the number of unbiased decays that could be used to complete a charm pair event.

A technique that estimated the charm momentum without measuring the momentum of

the neutral daughters allowed production studies on a large sample of charm decays from the E653 data. The background in the charm sample must be small in order for the momentum estimator to work well. This chapter will describe the philosophy, development, and performance of the momentum estimator used for production analysis of charm singles and charm pairs.

6.2 Kinematics

The momentum estimator developed for the production studies was based on modeling the charm decay as a two body decay. One body was the vector sum of the visible (charged) momentum and the other body was the neutral momentum [24]. The neutral system was assigned enough momentum to balance the momentum perpendicular to the charm direction (P-perp,P_t). Figure 35 depicts the momentum vectors in the laboratory frame for a neutral decay and Figure 36 shows the momentum vectors in the center of mass frame. The model assumed that the daughter particles are produced having only transverse momentum in the COM frame with respect to the parent direction.

6.2.1 Mass Assignments

The boost that transformed the COM frame to the LAB frame was defined by γ_{vis}. γ_{vis} was calculated by making mass assignments to the charged tracks, and calculating the γ that boosted the visible momentum to the frame where the visible momentum along the parent direction, P_{Lvis}, equals zero. The mass assignments depended on whether the vertex in question had a muon attached (muonic vertex) or if it was an unbiased vertex

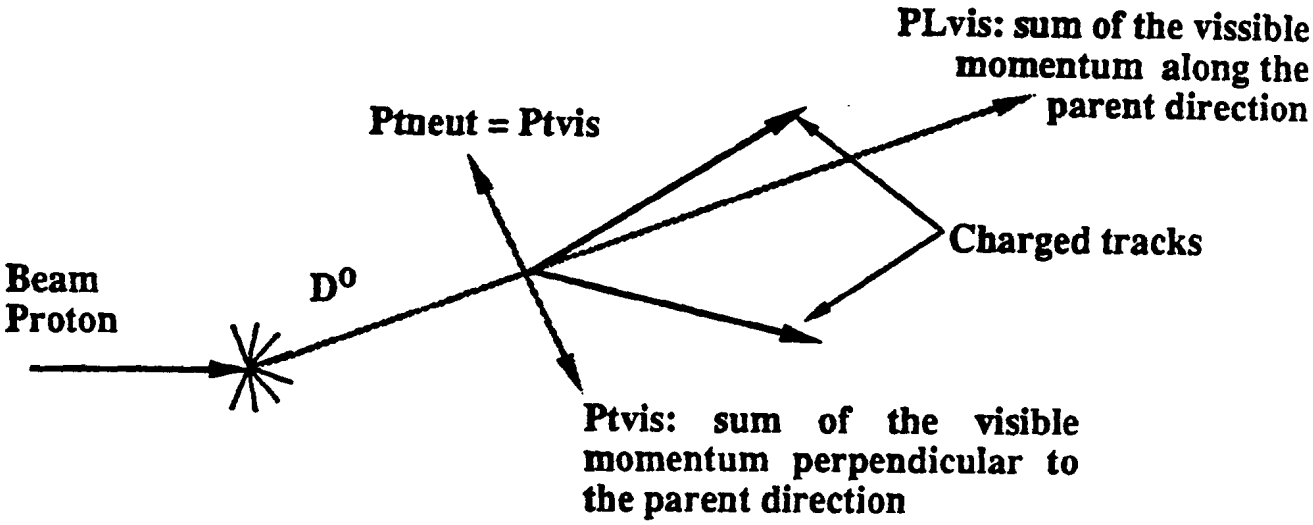

Figure 35: Momentum vectors in the laboratory frame for a neutral decay.

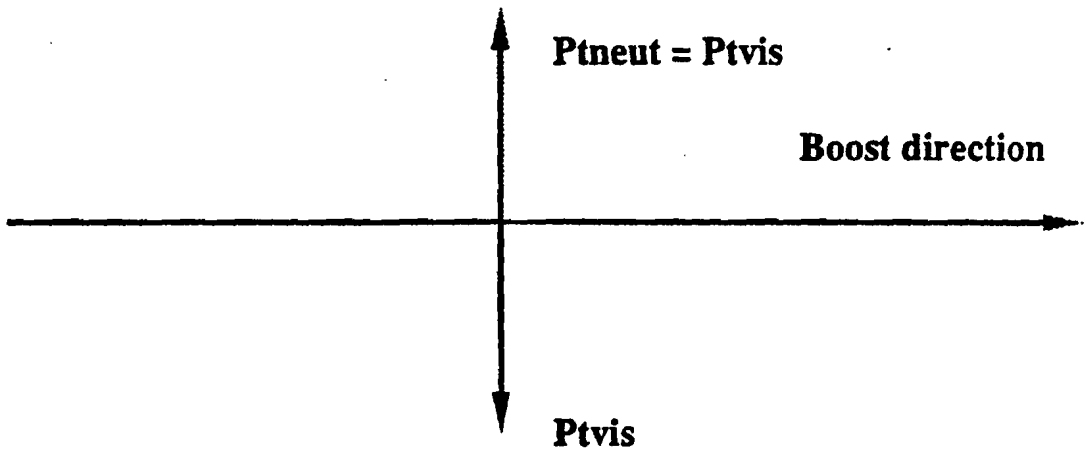

Figure 36: Momentum vectors in the center-of-mass (COM) frame for a neutral decay. Note that the only momentum in the center-of-mass frame in perpendicular to the parent direction in the LAB frame.

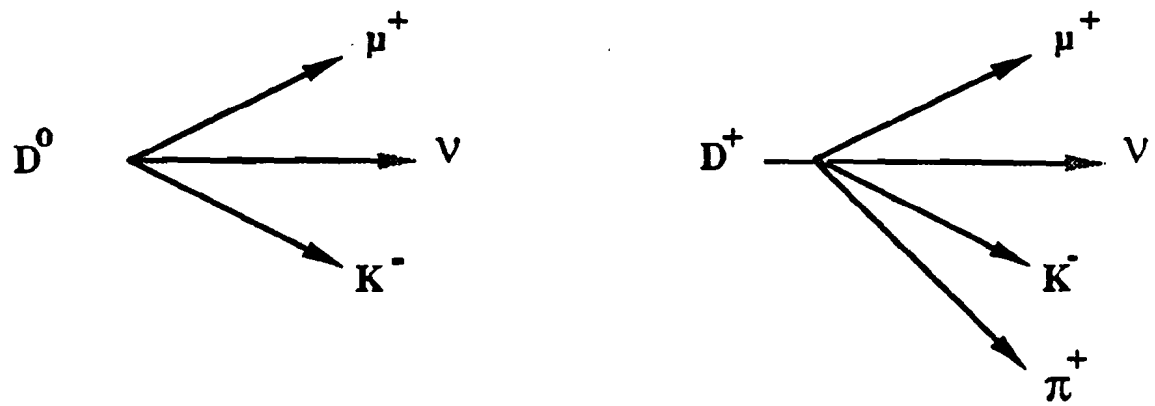

Figure 37: Mass assignments for decays with a tagged muon.

(hadronic vertex). For decays with a tagged muonic daughter, the muon track was assigned the muon mass and the track with charge opposite to that of the muon was assigned a kaon mass. For muonic tridents, the track with the same charge of the muon was assigned a π mass. The missing neutral for muonic vertices was assumed to be a neutrino with zero mass. Figure 37 shows the mass assignments for neutral and charged muonic decays. Unbiased decays were assumed to be hadronic and the mass assignments depend on the the sign of the muon in the partner decay (Figure 38). The track with the same charge as the muon in the event was assigned a kaon mass and tracks opposite in charge with respect to the muon were assigned a π mass. The missing neutral was assumed to be a π^o. For neutral decays with four charged tracks (V-4's) all the charged tracks were assumed to be $\pi's$ and the neutral track was a particle with zero mass.

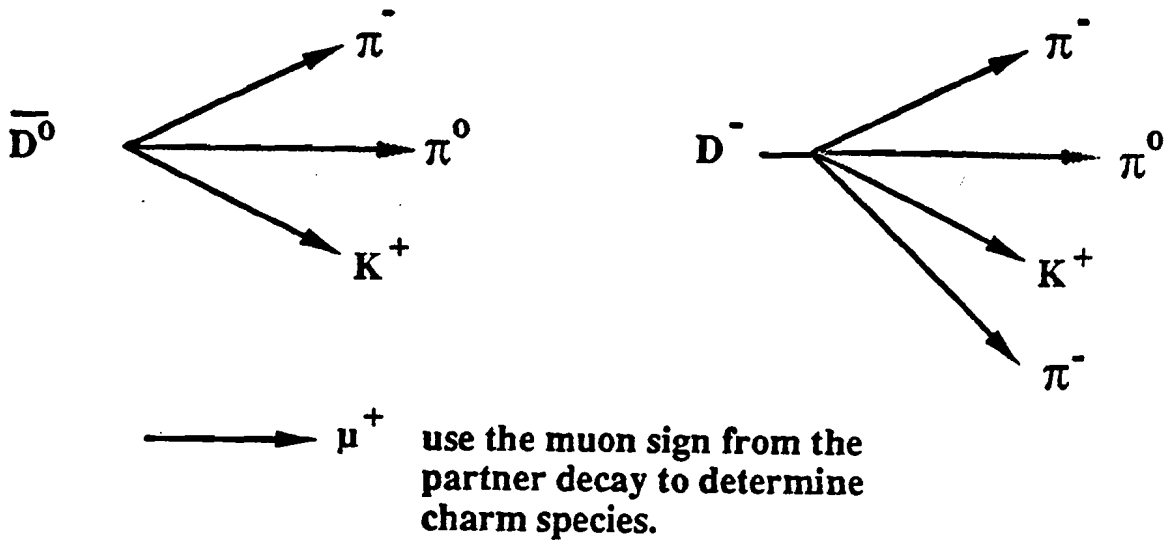

Figure 38: Mass assignments for decays without a tagged muon.

Once the mass assignments were given, the calculation for the momentum estimate was straight forward.

$$\gamma_{vis} = E_{Lvis}/M_{vis} \tag{27}$$

$$E_{Lvis} = \sqrt{{P_{Lvis}}^2 + {M_{vis}}^2} \tag{28}$$

$$M_{vis} = \sqrt{E_{vis}^2 - P_{vis}^2} \tag{29}$$

$$P_{tneut} = P_{tvis} \tag{30}$$

$$P_{min} = M_D * \gamma_{vis} \tag{31}$$

$$M_{min} = \sqrt{P_{tvis}{}^2 + M_{vis}{}^2} + \sqrt{P_{tneut}{}^2 + M_{neut}{}^2} \tag{32}$$

M_{min} was the transverse mass for the decay and the closer M_{min} was to the actual value of M_D, the more accurate the momentum estimate (P_{min}). Using Monte Carlo generated charm decays the resolution function for the momentum estimate was parameterized as a function of M_{min}.

6.3 The Resolution Function and Monte Carlo Studies

Monte Carlo decays of charmed meson (D^o,D^+) into Cabbibo favored modes were generated to develop the momentum estimator. The decays in the E653 data sample were divided into distinct topologies by the prong count and muon tag. The dominant and measured decay modes were installed into the Monte Carlo so that a specific topology could be studied. The decay modes for the topologies used in production studies are shown in Table 23 with the branching ratios that were used in this analysis.

Mode	Reference	Branching Ratio (percent)
Hadronic Kinks		
$D^+ \to K^o\pi^+$	[38]	2.8 ± 0.4
$D^+ \to K^o\pi^+\pi^o$	[38]	$8.3\pm^{1.8}_{1.7}$
$D^+ \to K^o\pi^+\pi^o\pi^o$	[61]	2.8
Muonic Kinks		
$D^+ \to K^o\mu^+\nu$	[60]	$10.2 \pm 3.1 \pm 1.7$
$D^+ \to K^o\pi^o\mu^+\nu$	[60]	$3.8 \pm^{5.3}_{1.7} \pm 0.6$
Hadronic V-2's		
$D^o \to K^-\pi^+$	[38]	$3.77\pm^{0.37}_{0.32}$
$D^o \to K^-\pi^+\pi^o$	[38]	$12.5\pm^{1.5}_{1.4}$
$D^o \to K^o\pi^+\pi^+$	[38]	$5.6\pm^{0.7}_{0.6}$
$D^o \to K^-\pi^+\pi^o\pi^o$	[38]	15 ± 5
$D^o \to K^o\pi^+\pi^-\pi^o$	[37]	$11.5 \pm 2.2 \pm 2.8$
Muonic V-2's		
$D^o \to K^-\mu^+\nu$	[37]	$4.1 \pm 0.7 \pm 1.2$
$D^o \to K^o\pi^-\mu^+\nu$	[37]	$2.7 \pm^{1.1}_{1.0} \pm 1.6$
$D^o \to K^-\pi^o\mu^+\nu$	[37]	$1.7 \pm^{0.9}_{0.7} \pm 0.6$
Hadronic C-3's		
$D^+ \to K^-\pi^+\pi^+$	[38]	$7.8\pm^{1.1}_{0.8}$
$D^+ \to K^-\pi^+\pi^+\pi^o$	[38]	$3.7\pm^{1.5}_{0.8}$
$D^+ \to K^o\pi^-\pi^+\pi^+$	[38]	$7.0\pm^{2.3}_{2.1}$
$D^+ \to K^-\pi^+\pi^+\pi^o\pi^o$	[54]	$2.2\pm^{5.0}_{22}$
$D^+ \to K^o\pi^-\pi^+\pi^+\pi^o$	[54]	$4.4\pm^{5.0}_{22}$
Muonic C-3's		
$D^+ \to K^-\pi^+\mu^+\nu$	[37]	$3.9 \pm^{0.9}_{0.8} \pm 0.7$
$D^+ \to K^o\pi^+\pi^-\mu^+\nu$	[38]	$2.2\pm^{5.0}_{0.7}$
$D^+ \to K^-\pi^+\pi^o\mu^+\nu$	[38]	$4.4\pm^{5.2}_{1.5}$
Hadronic V-4's		
$D^o \to K^-\pi^-\pi^+\pi^+$	[38]	$7.9\pm^{1.0}_{0.9}$
$D^o \to K^o\pi^-\pi^-\pi^+\pi^+$	[61]	4.3
$D^o \to K^-\pi^-\pi^+\pi^+\pi^o$	[61]	7.9

Table 23: Branching Ratios used in the Monte Carlo development of the momentum estimator and charm selection.

The generated momentum was then compared to the momentum estimate of P_{min} as a function of M_{min}. Figure 40 shows the scatter plot of $P_{min}/P_{generated}$ versus M_{min} for D^o two prong decays. An important feature of Figure 40 is that the M_{min} distribution is concentrated at the value for the D mass. This means that the estimator performed well for the majority of the decays. The resolution dependence on M_{min} is also quite evident from Figure 40 and the projections onto the P_{min}/P_{gen} axis for different slices in M_{min} shown in Figure 41.

M_{min} was a measured quantity and had measurement errors (assumed to be gaussian). The resolution distribution that corresponded to a measured value for M_{min} and its error was the sum of the resolution function distributions weighted by the amount defined by the value for M_{min} and its error (Equation 34). (Error in M_{min} depends on the error in the P_t of the decay.)

$$M_{min} = M_{min} \pm \delta M_{min} \tag{33}$$

$$Resolution\ Function = \sum R_j \int_{m_{0j}}^{m_{fj}} (\sqrt{2\pi}\delta M_{min})^{-1} e^{(m_j - M_{min})^2/\delta M_{min}{}^2} dm_j \tag{34}$$

$$R_j = P_{min}/P_{gen}\ distribution\ for\ m_{0j} < m_j < m_{fj} \tag{35}$$

For example: If M_{min} and its error were entirely within a 100 MeV/c^2 interval in M_{min}, the resolution function representing that value of M_{min} would be assigned to the decay. If M_{min} and its error were situated 50% in R_j and 50% in R_i, the resolution function, R, would be the average of the two resolution functions, R=(R_j + R_i)/2. The integral in

Equation 34 represents the weight assigned to the 100 MeV/c^2 binned resolution functions. The resolution function for the decay was then shifted so the average value for $P_{min}/P_{generated}$ is equal to one. Figures 42 and 43 are the projected resolution distributions for hadronic D^o 2-prong decays and Figures 44 and 45 are for muonic D^+ decays into three prongs. Figures 46 and 47 show the resolution distributions for hadronic three prong D^+ decays and Figures 48 and 49 are for four prong hadronic D^o decays.

6.4 The 0-C Analogy

The kinematics described in the previous section are analogous to those used for a 0-C (unconstrained) fit to the decay. Using the same particle identification as in the previous section, Formulas 36 through 42 for the neutral momentum assuming a known parent mass are obtained. Equation 36 is a quadratic and will yield two solutions for the neutral momentum, except in the degenerate case. The two solutions represent the ambiguity in the longitudinal momentum in the COM frame. The degenerate solution was called the solution at the minimum since it represented the minimum of the curve shown in Figure 39 and it also represented the case where P_L was equal to zero in the COM frame (This is the same assumption that was made in the previous section).

When this minimum was at the D mass the decay had only one momentum solution for the charm parent. For most charm decays the D mass was above the minimum mass and the solution at the minimum now represents the momentum for a parent particle with a mass equal to the minimum mass. The curve in Figure 39 shows the relation between the

parent mass for the decay and its quadratic solutions for the neutral momentum. The closer the minimum mass was to the D mass the closer the momentum at the minimum was to the actual charm momentum.

Since the momentum estimator was first developed using the 0-C technique, the names for the momentum and mass variables were taken from this analogy. Hence P_{min} was the momentum for a particle of mass M_{min} which decayed into the hypothesis chosen for this decay, or M_{min} and P_{min} were the mass and momentum for the decay if its daughters had only transverse momentum in the COM frame.

$$P_{lneut} = -b/2a \pm \sqrt{b^2 - 4ac}/2a \tag{36}$$

$$a = P_{lvis}^2/E_{vis}^2 - 1 \tag{37}$$

$$b = (M_D^2 - M_{vis}^2 - M_{neut}^2 - 2P_{tvis}^2)P_{lvis}/E_{vis}^2 \tag{38}$$

$$c = (M_D^2 - M_{vis}^2 - M_{neut}^2 - 2P_{tvis}^2)^2/4E_{vis}^2 - P_{tvis}^2 - M_{neut}^2 \tag{39}$$

$$P_D = P_{lvis} + P_{lneut} \tag{40}$$

$$M_{min}^2 = \sqrt{4(P_{tvis}^2 + M_{neut}^2) * (P_{tvis}^2 + M_{vis}^2)} + M_{vis}^2 + M_{neut}^2 + 2P_{tvis}^2 \tag{41}$$

$$P_{lmin} = -b/2a \; with M_D = M_{min} \tag{42}$$

$$P_{min} = P_{lvis} + P_{lmin} \tag{43}$$

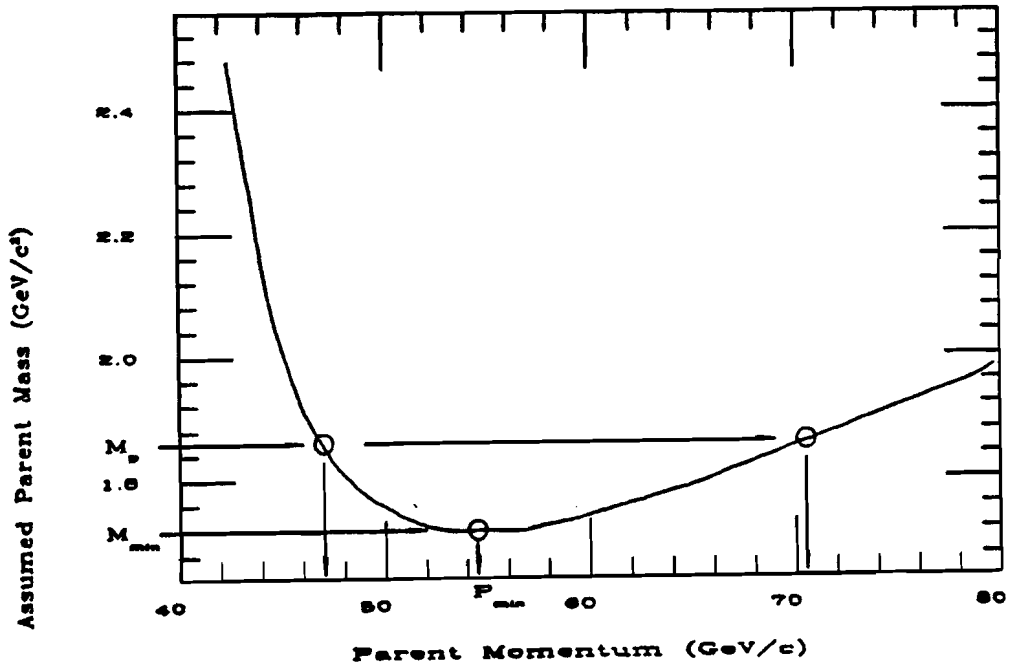

Figure 39: The momentum solutions for the 0-C equation as a function of parent mass.

6.5 Other Charm Decay Modes

The decay modes listed in Table 23 are not complete. However the performance of the estimator will not be strongly effected by the decay modes that are not accounted for. The resolution of the momentum estimator depends mainly on how many neutrals are involved in the decay, it does not depend heavily on the masses of the particles involved. This was seen by looking at neutral hadronic decays and studying the difference between the decays which involve K^o's and π^o's. The plots of the resolution function versus M_{min} are quite similar for the two sets of decays, and the fact that the kaon was mis-identified in the K^o decays has not resulted in any significant difference in the resolution functions. The momentum estimator will be tested at the end of the next section by comparing the results of maximum likelihood fits on Monte Carlo data to the known generated values.

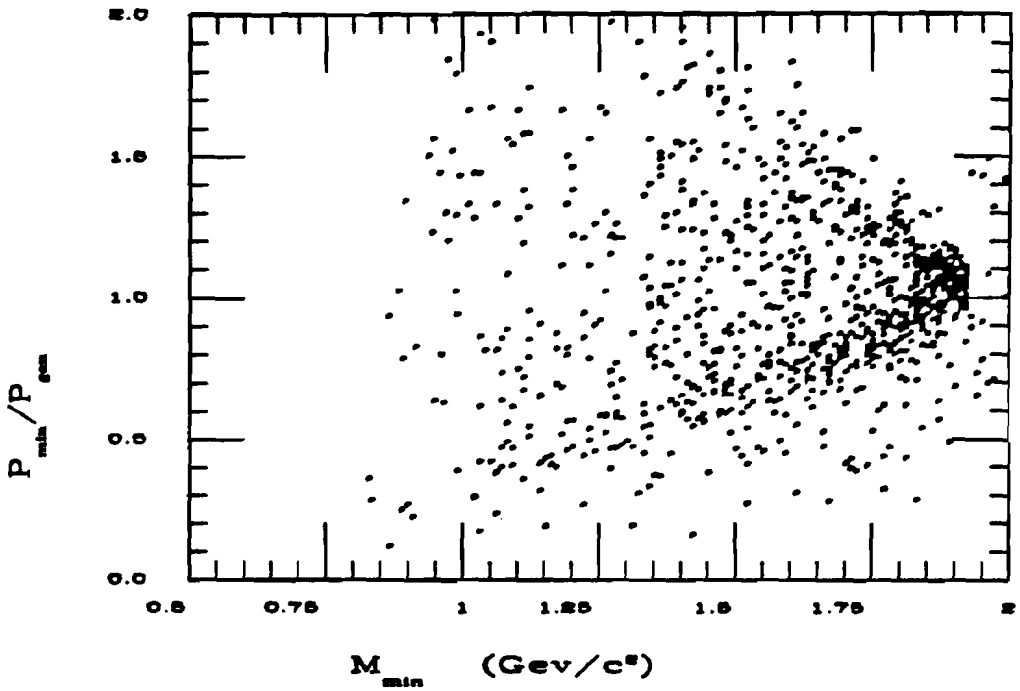

Figure 40: $P_{min}/P_{generated}$ versus M_{min} for two prong muonic D^o decays.

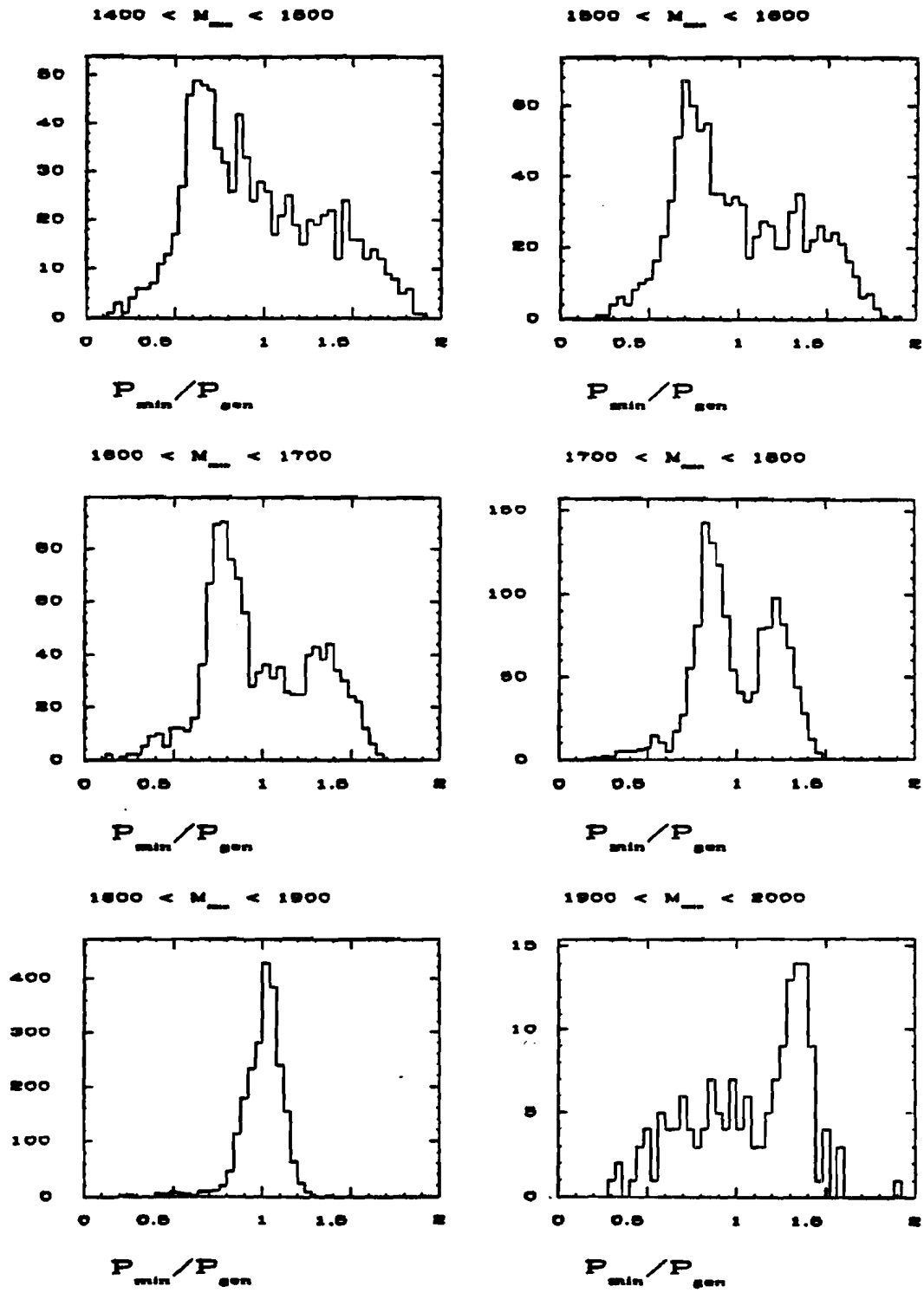

Figure 41: $P_{min}/P_{generated}$ projections in $100MeV/c^2$ slices of M_{min} for two prong muonic D^o decays.

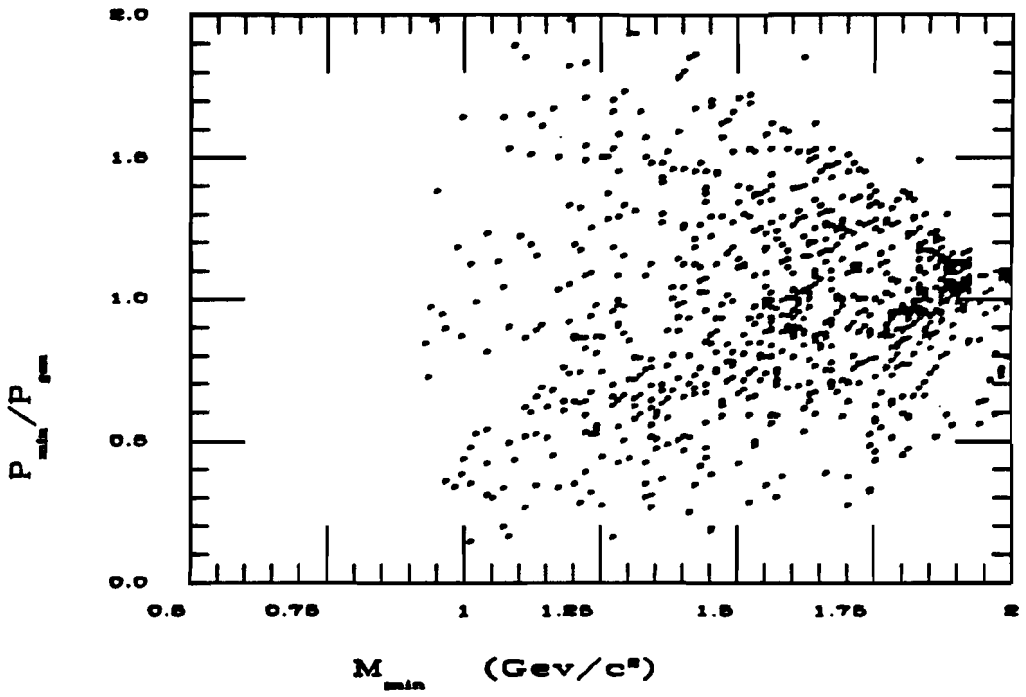

Figure 42: $P_{min}/P_{generated}$ versus M_{min} for two prong hadronic D^o decays.

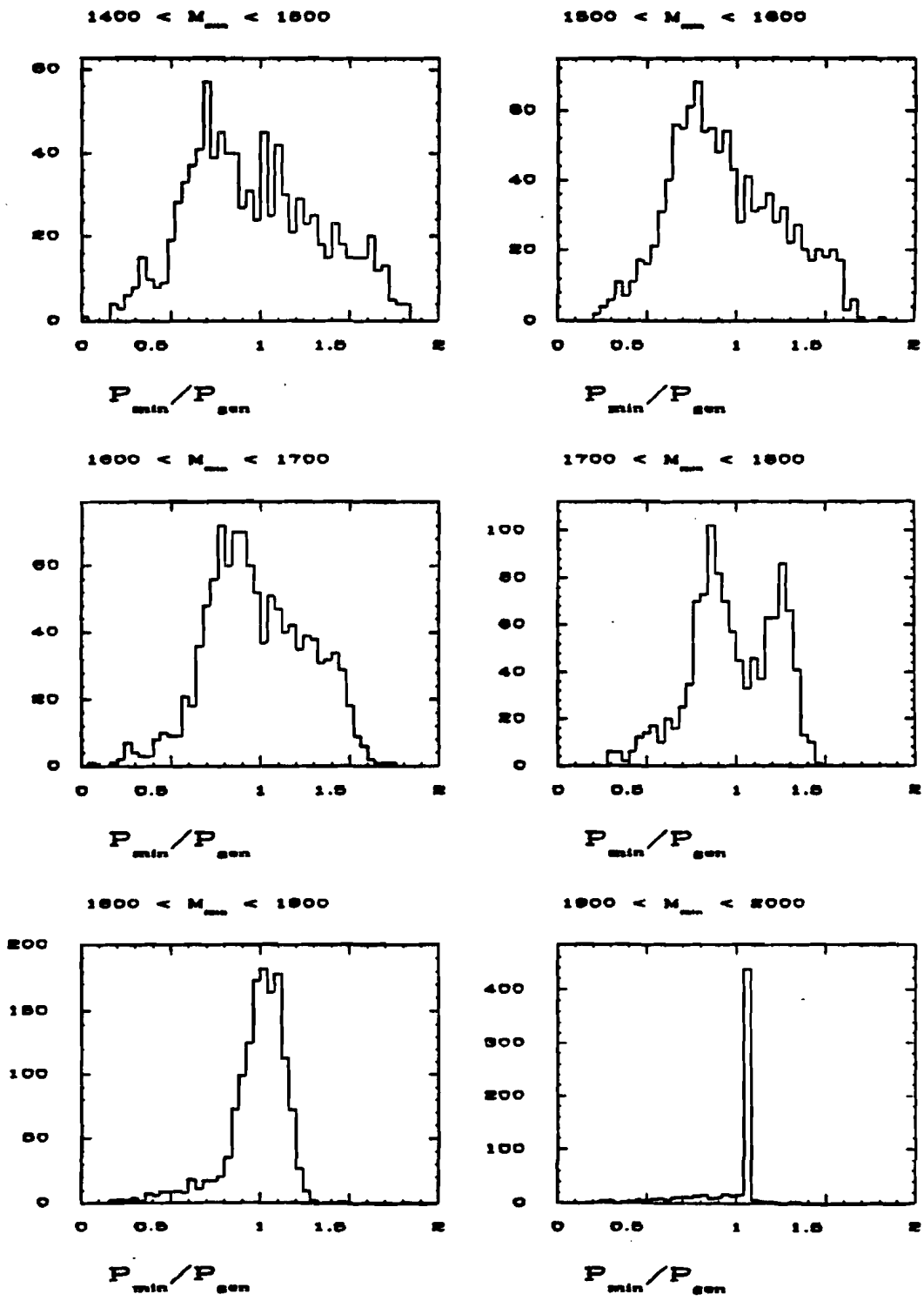

Figure 43: $P_{min}/P_{generated}$ projections $100MeV/c^2$ slices of M_{min} for two prong hadronic D^o decays.

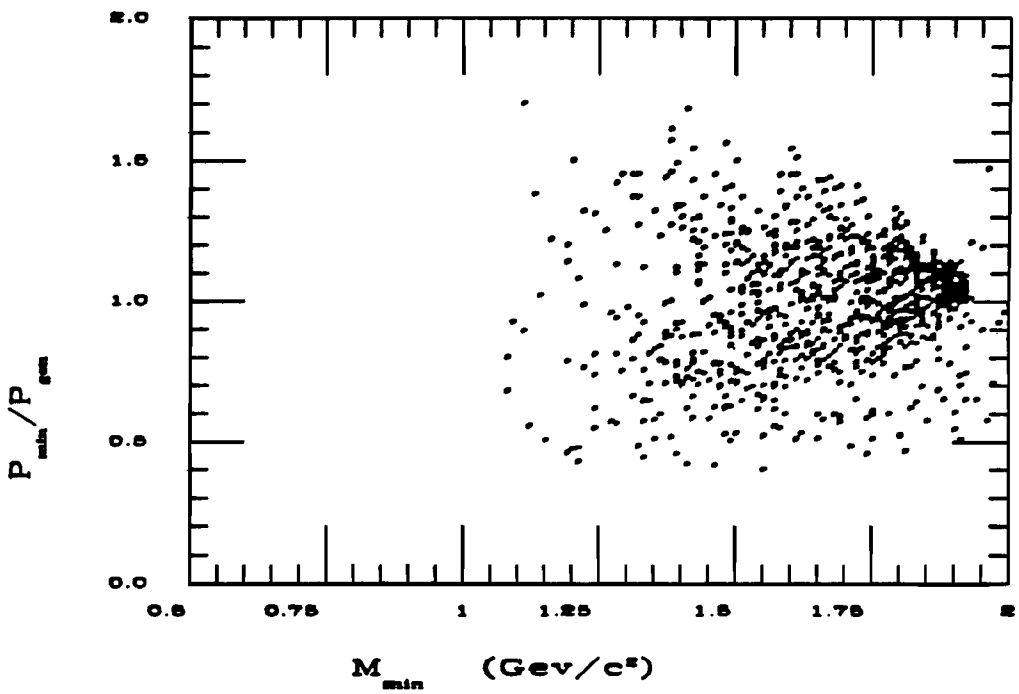

Figure 44: $P_{min}/P_{generated}$ versus M_{min} for three prong muonic D^+ decays.

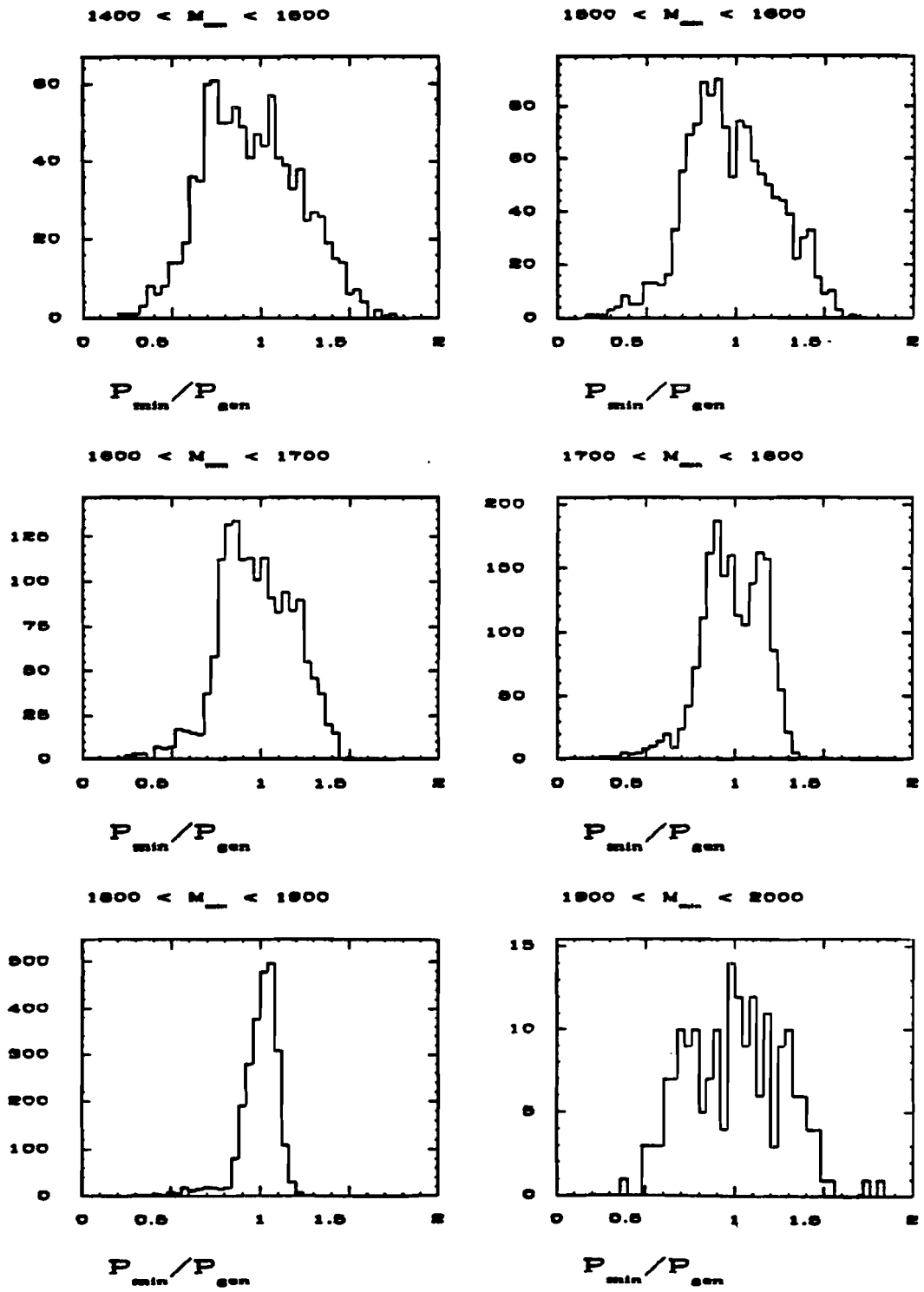

Figure 45: $P_{min}/P_{generated}$ projections in $100MeV/c^2$ slices of M_{min} for three prong muonic D^+ decays.

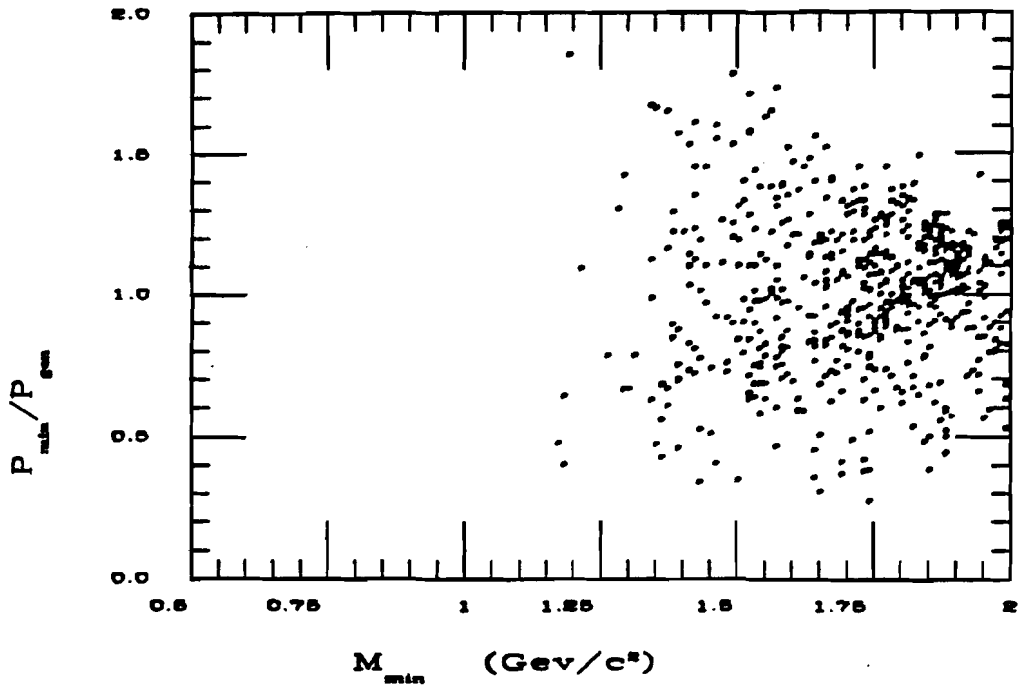

Figure 46: $P_{min}/P_{generated}$ versus M_{min} for three prong hadronic D^+ decays.

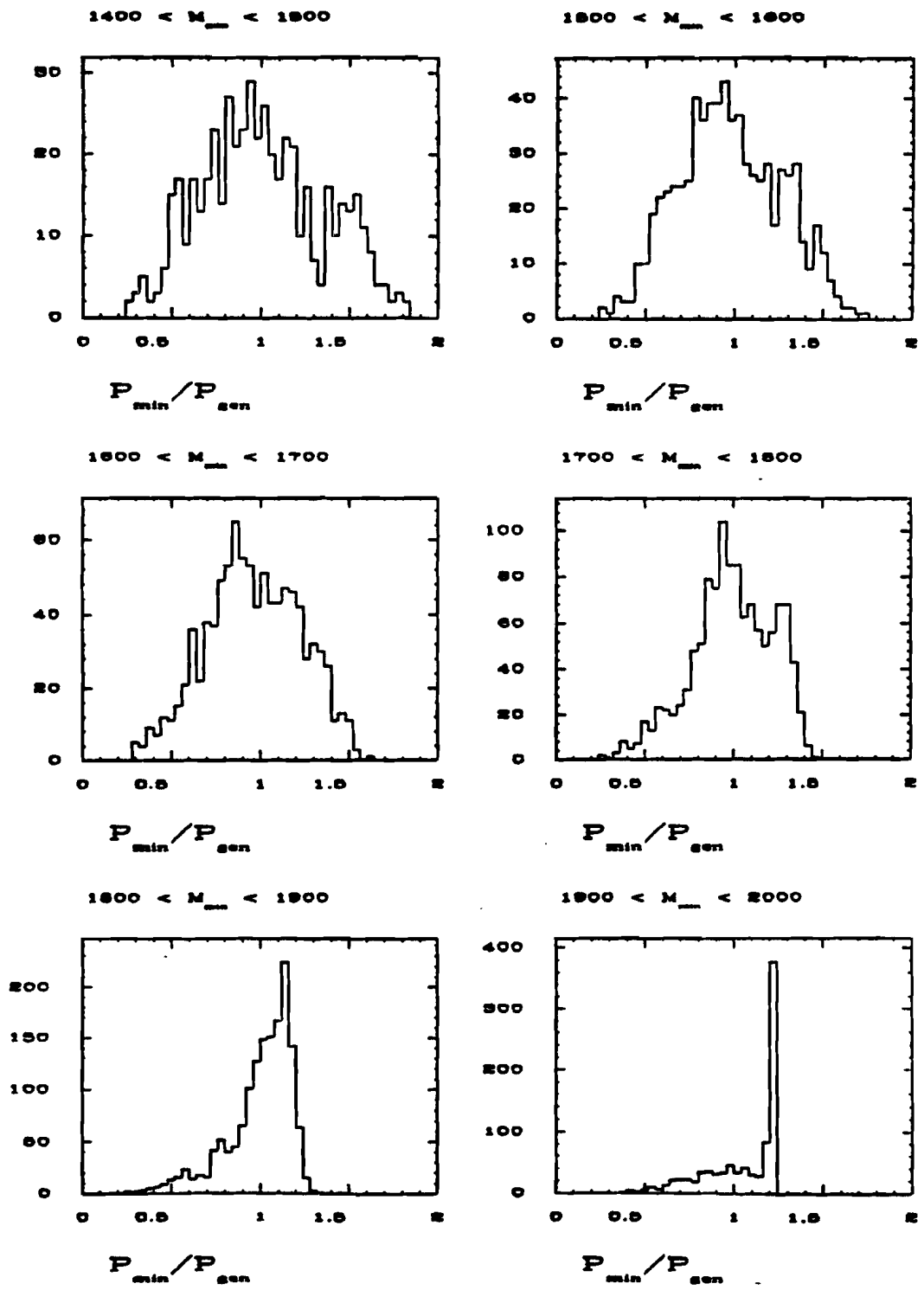

Figure 47: $P_{min}/P_{generated}$ projections in $100MeV/c^2$ slices of M_{min} for three prong hadronic D^+ decays.

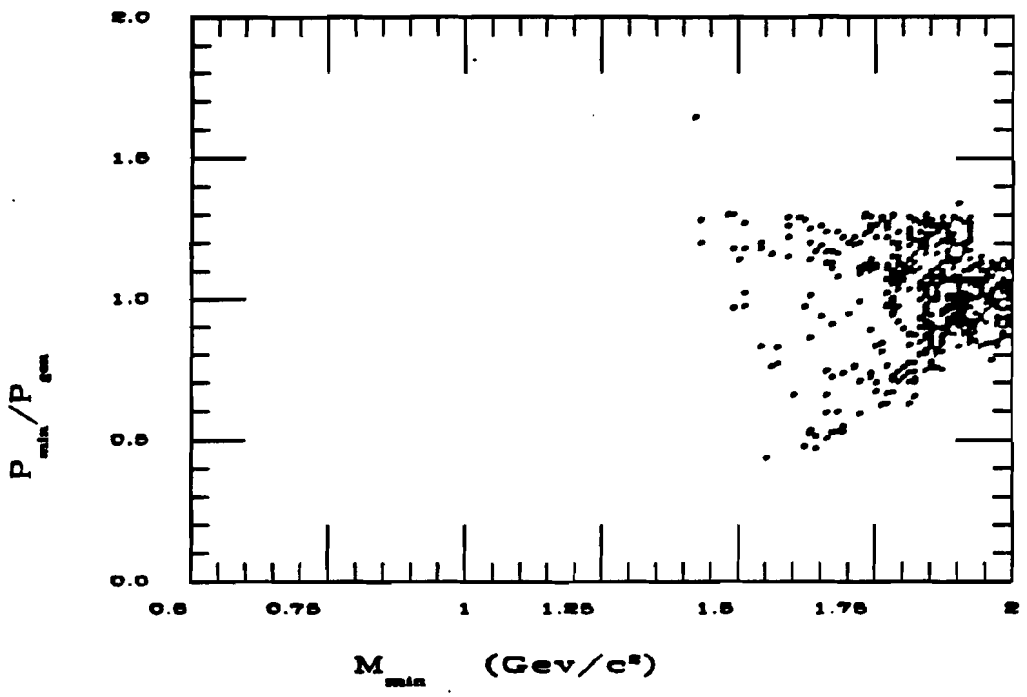

Figure 48: $P_{min}/P_{generated}$ versus M_{min} for four prong hadronic D^o decays.

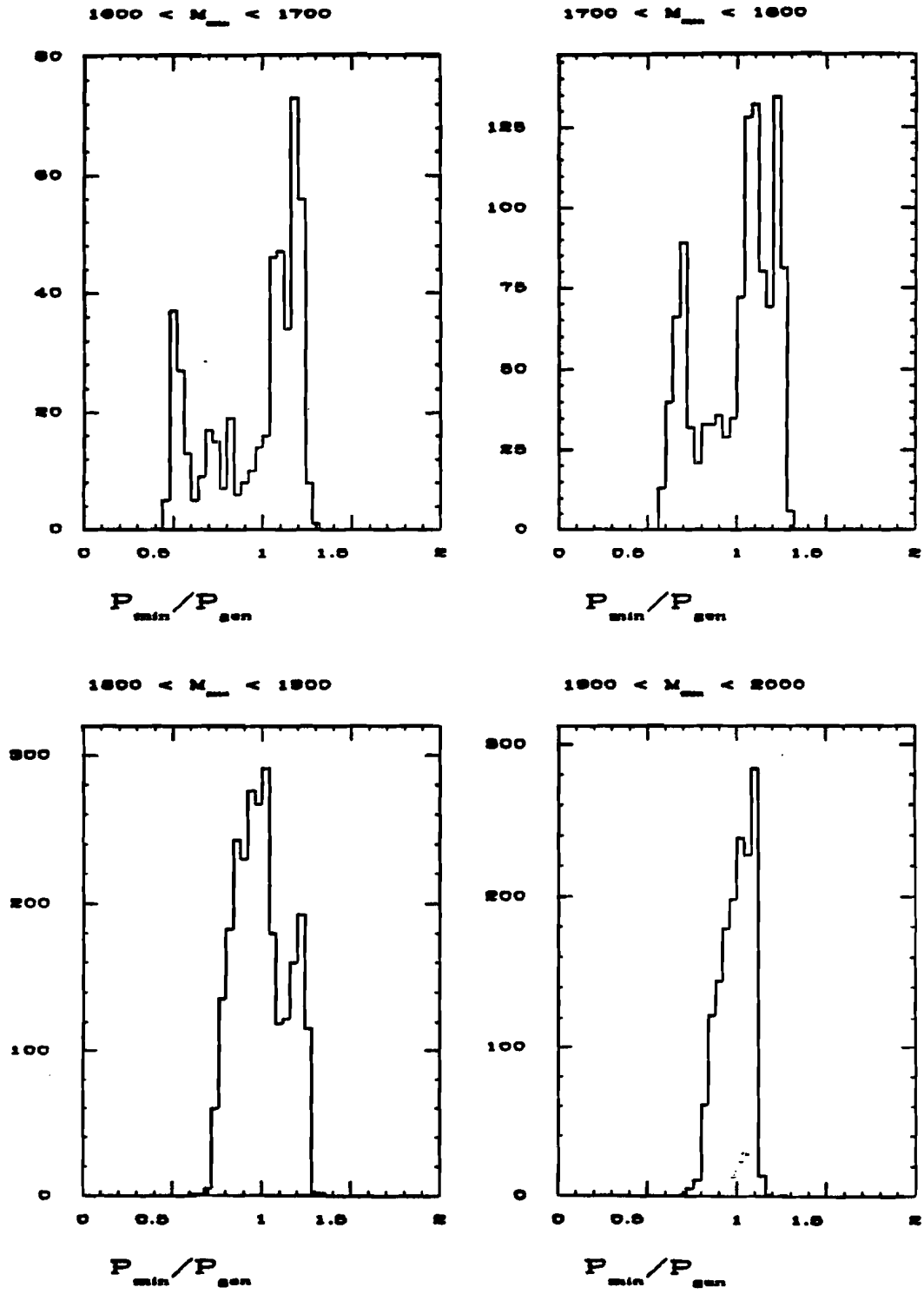

Figure 49: $P_{min}/P_{generated}$ projections in $100MeV/c^2$ slices of M_{min} for four prong hadronic D^o decays.

Chapter 7

Maximum Likelihood Technique and Efficiencies

7.1 Introduction

The non-gaussian resolution function for the charm parent momentum introduced in the preceding chapter must be incorporated into the fitting analysis. Maximum likelihood fitting provided a natural method of incorporating generic resolution functions into the fitting procedure. This chapter will describe the maximum likelihood fitting technique used in E653 analysis. The first section will present a short review of the method, and the following sections will be devoted to its use in this analysis.

7.2 Probabilistic Motivation

The maximum likelihood technique has been used in situations where due to low statistics least squares fitting was not applicable [23,59]. Since the technique relies on maximizing probabilities, incorporating a resolution function (or in other words a probability distribution) is straight forward.

The simplest situation for maximum likelihood fitting (Maxlike) is one where the resolution function is a δ function and the efficiency distribution is a constant. For this case, the probability of observing event i as a function of $f(x_i, n)$ is:

$$P_i(x_i, n) = N(n) f(x_i, n) \tag{44}$$

where x_i is the measured quantity and n is the parameter to be determined. The probability distribution must be properly normalized such that:

$$\int P_i(x_i, n) dx = 1 \tag{45}$$

The likelihood distribution for the set of $i = (1, 2, \ldots, m)$ events is

$$\mathcal{L}(n) = \prod_{i=1}^{m} P_i(x_i, n) \tag{46}$$

By maximizing $\mathcal{L}(n)$ with respect to n the value for the n that has the highest probability of describing the distribution is obtained.

7.2.1 Variable Efficiencies

The real world usually does not provide experimenters with flat (constant) efficiencies. The measured quantity x is defined to have efficiency $\epsilon(x)$. The efficiency $\epsilon(x)$ can be thought of as the relative probability of reconstructing the event at the measured value of x. Thus the total probability for the event is:

$$P(x_i, n) = N(n)\epsilon(x_i)f(x_i, n) \tag{47}$$

$$N(n) = (\int \epsilon(x)f(x, n)dx)^{-1} \tag{48}$$

Once the probability function and its normalization have been determined the MaxLike procedure for determining the value of n is the same as the case with uniform efficiencies. The probability distribution must be normalized and the efficiencies need to be well known for the entire range of x even though the events might be clustered in a small range of x. With the introduction of variable efficiency the integration usually has to be done numerically.

7.2.2 Resolution Functions

The measured variable x_i is measured with a known resolution, $R(x_i, x_g)$, where x_i is the measured value and x_g is the generated (true) value. $R(x_i, x_g)$ can have any functional shape (See Figure 50).

The measured quantity is x_i and it is the generated value x_g that is unknown, and

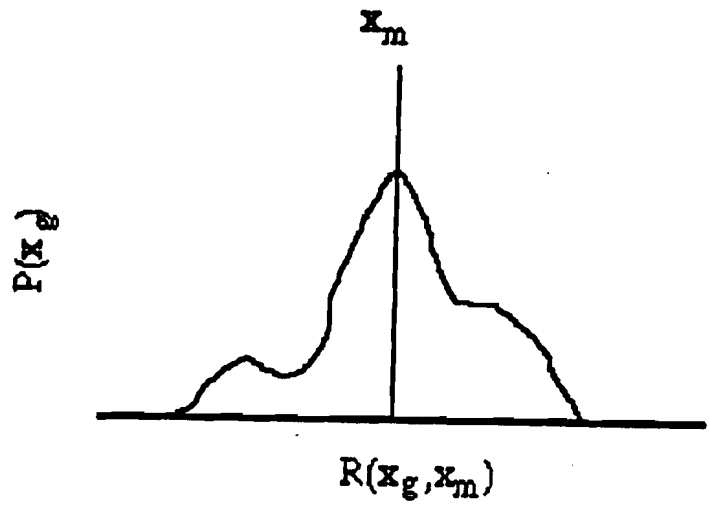

Figure 50: Generic resolution function $R(x_i, x_g)$ as function of x_g

$R(x_i, x_g)$ represents the probability that the generated value was x_g given the measured value of x_i. The probability for the event to have a measured value of x_i is:

$$P(x_i, n) = \int N(n)\epsilon(x_g)f(x_g, n)R(x_i, x_g)dx_g \tag{49}$$

$$N(n) = (\int\int \epsilon(x_g)f(x_g, n)R(x, x_g)dx_g dx)^{-1} \tag{50}$$

Note that the probability integral is over all *generated* values of x_g whereas the normalization integral is over both x_g and the measured variable x_i. This distinction is important since the measured variable (x_i) may be limited to a small range but the generated variable (x_g) can have all allowed values. The efficiencies must be determined for the full range of x_g.

7.2.3 Maximum Likelihood Implementation in E653

As described in the previous chapter the momentum estimation for the charm parent depends on the topology and visible characteristics of the decay. A decay dependent resolution function is also constructed for each decay. Thus the resolution function changes with each decay and forces the maximum likelihood normalization (Equation 50)to be calculated for each decay. Once the normalization has been determined the probability (eq. 49) for observing the decay is calculated and then this probability is combined with all the other probabilities in the event sample to form the maximum likelihood distribution (eq. 46).

All the elements to perform the maximum likelihood calculation have been described except for the efficiencies. The following sections describe the efficiency distributions used in the fitting procedure and how they were obtained.

7.3 Topological Efficiencies

The E653 charm decay sample was divided into distinct topological categories. These decay topologies had different momentum resolution functions due to the differing number of missing neutrals in the topologies. The efficiencies for reconstructing individual decays are also different for the different topologies. This is clearly the case for the muonic decays, since the muon daughter had to pass special scanning selection criteria that the hadronic daughters did not.

The efficiencies must also be determined as a function of the variable of interest. For

single charm production studies the traditional kinematic variables are X_f and P_t^2. These single charm efficiency distributions are then used to construct efficiency distributions for the charm pair.

7.3.1 Single Charm Efficiencies

The efficiencies for reconstructing charm decays were determined by using the GEANT Monte Carlo package to simulate the spectrometer performance. Events were generated at the hit level and were processed through the complete spectrometer reconstruction code. The emulsion efficiencies were assumed to be flat for this analysis.

Charm mesons were produced in uncorrelated pairs and were allowed to decay via the known branching ratios. The charm mesons were produced using the differential cross section parameterization:

$$\frac{d\sigma}{dX_f dP_t^2} \sim (1 - X_f)^n \cdot e^{-bP_t^2} \tag{51}$$

The user was allowed to define the n and b values used for charm generation. Correlated biases in the efficiencies were accounted for by requiring the P_t^2 distribution to reflect that seen in the data when determining the X_f efficiencies (and vis versa for the P_t^2 efficiencies). Complete details of the single charm efficiencies can found elsewhere [35].

The X_f efficiencies for muonic topologies in the emulsion are shown in Figure 51. and for hadronic decays in the emulsion X_f efficiencies are shown in Figure 52. The efficiency for the hadronic decays extend further into the the negative X_f region than the muonic decays due to the selection cuts placed on the muonic tracks. The efficiency for all

topologies peaks near the positive side of zero than falls rapidly zero in the negative X_f hemisphere. The loss of efficiency at negative X_f is due to the wide angle low momentum daughter tracks. The efficiencies also show a slight decline at $X_f > 0.5$. These fast forward particles will have the daughter tracks in the densely populated forward cone and will fail reconstruction due to pattern recognition failures in this region.

The P_t^2 efficiencies for the muonic topologies in the main emulsion block are shown if Figure 53. The slight dip in the muonic efficiencies at small P_t^2 is due to the charm selection cuts placed on the μ track. The hadronic topologies are shown in Figure 54. The P_t^2 efficiencies are relatively flat, because there were no selectio cuts applied to these decays.

The precision of the efficiencies was limited by three coherent sources: CPU hours, disk space and patience.

7.4 Charm Pair Efficiencies

Efficiencies for the charm pair distributions were determined by two different methods. For the fitted kinematic quantities, X_f and P_t^2, the efficiencies were calculated on an event by event basis, integrating the individual single charm efficiencies to obtain the overall efficiency for the charm pair.

For the pair X_f efficiencies the integration was as follows:

$$\epsilon(X_{fPAIR}) = \int_{-1}^{1}\int_{-1}^{1} N \cdot \epsilon(X_f(D)) \cdot \epsilon(X_f(\bar{D})) \cdot (1 - X_f(D))^n \cdot (1 - X_f(\bar{D}))^n dX_f(D) dX_f(\bar{D}) \tag{52}$$

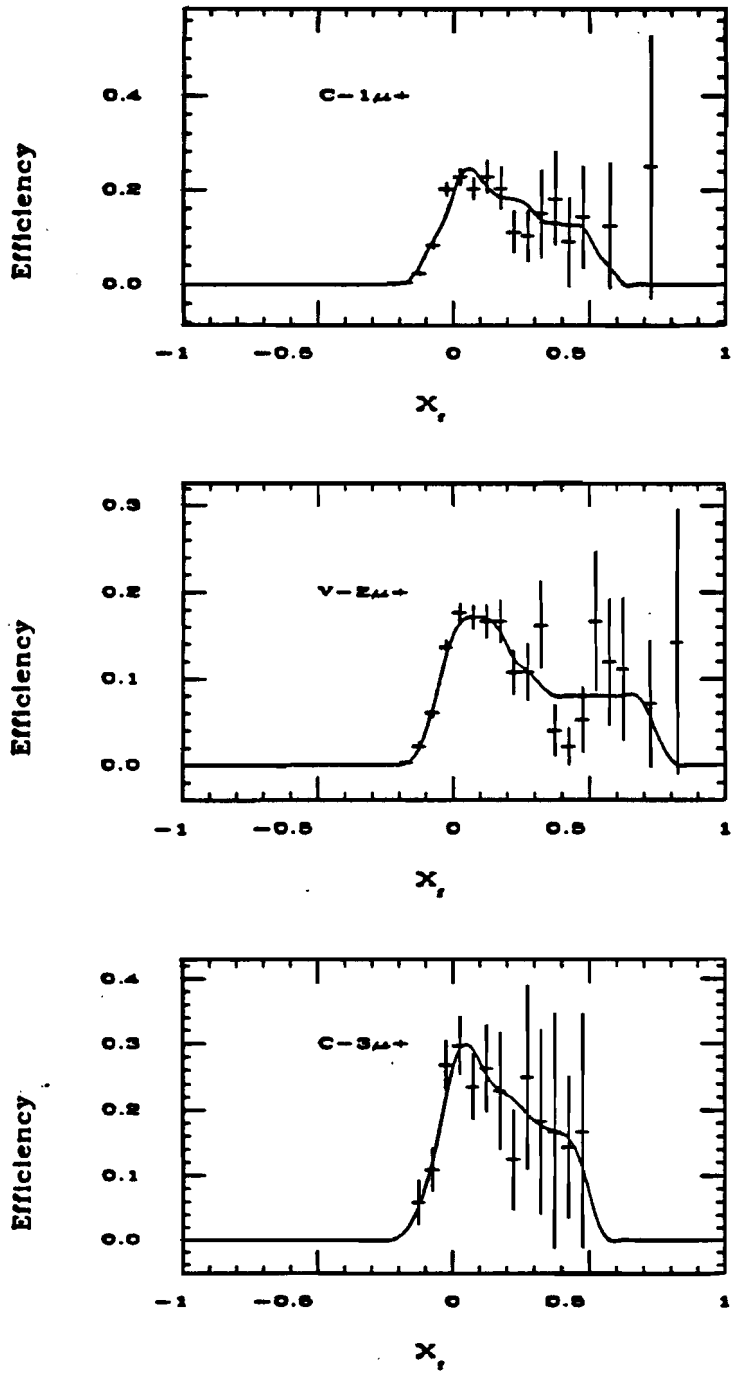

Figure 51: X_f efficiencies for muonic decays in the emulsion block.

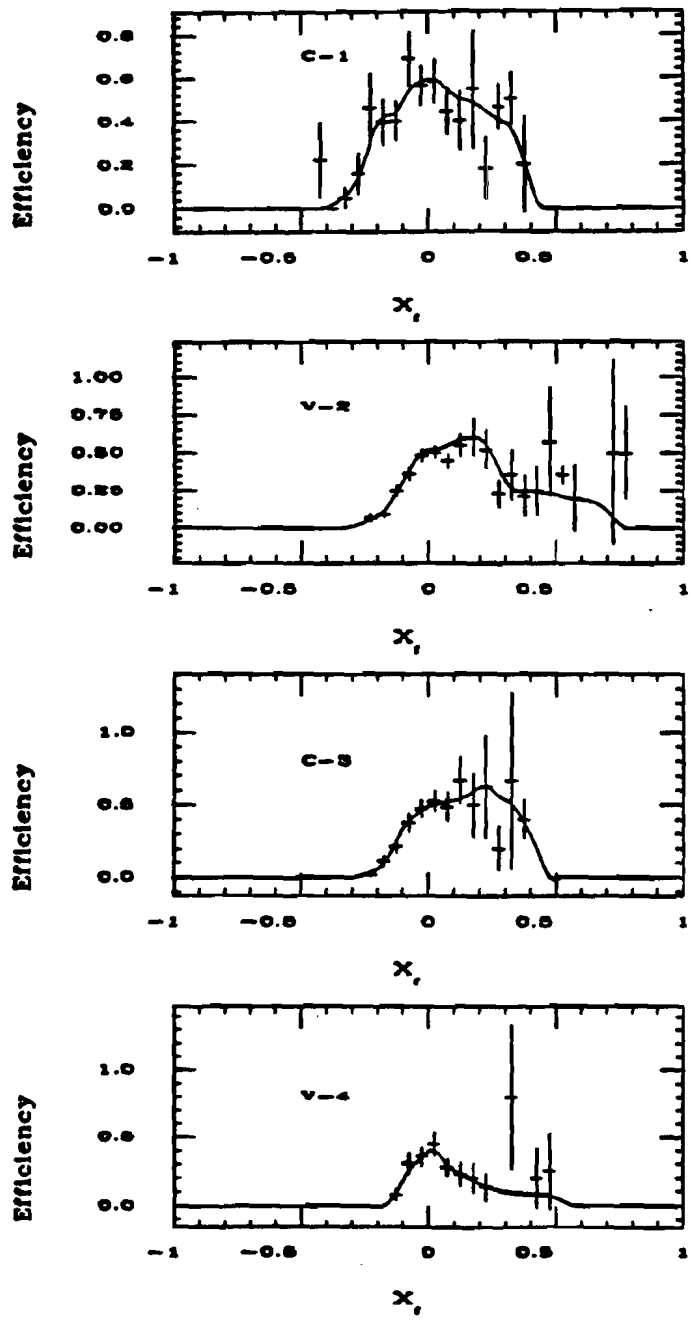

Figure 52: X_f efficiencies for hadronic decays in the emulsion block.

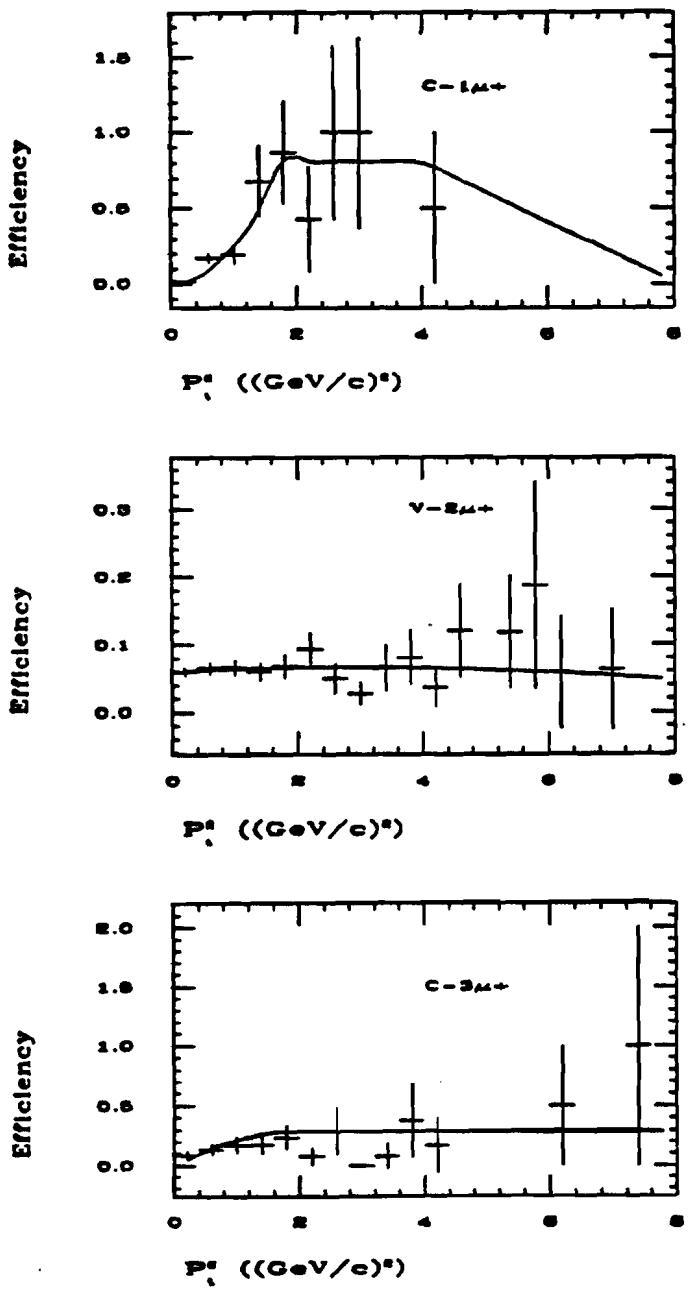

Figure 53: P_t^2 efficiencies for muonic decays in the emulsion block.

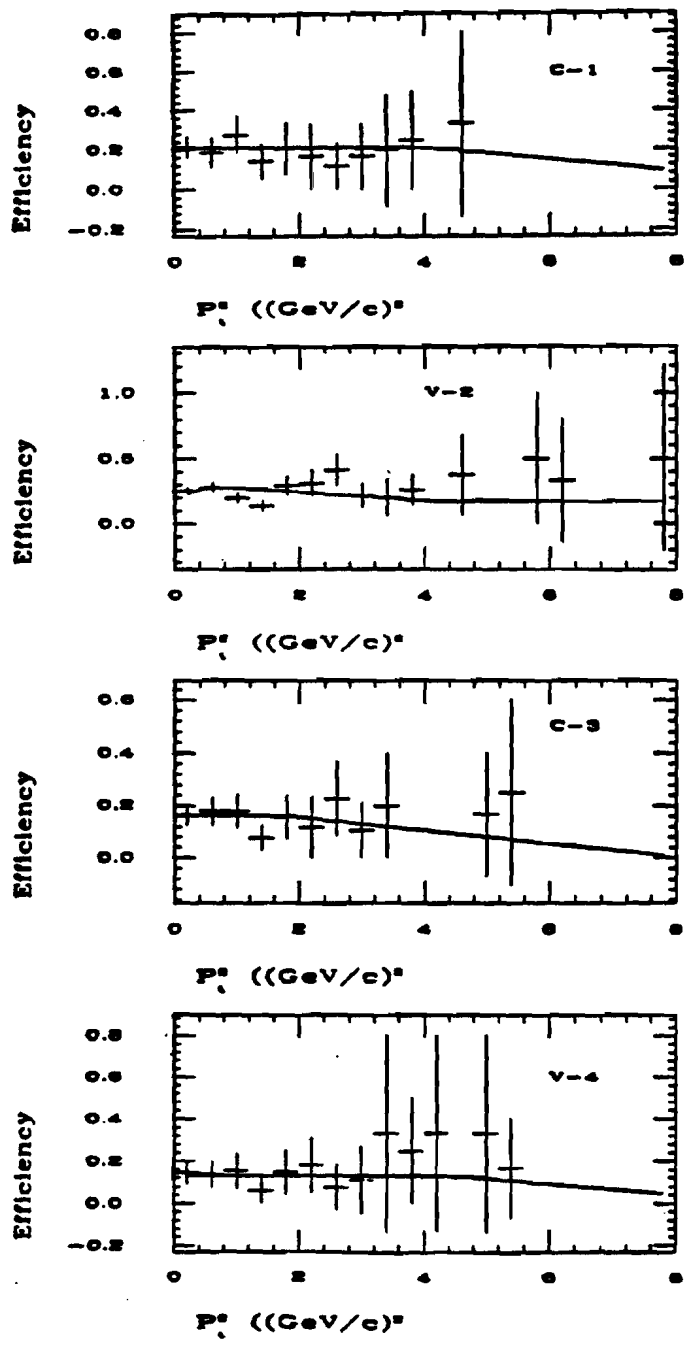

Figure 54: P_t^2 efficiencies for hadronic decays in the emulsion block.

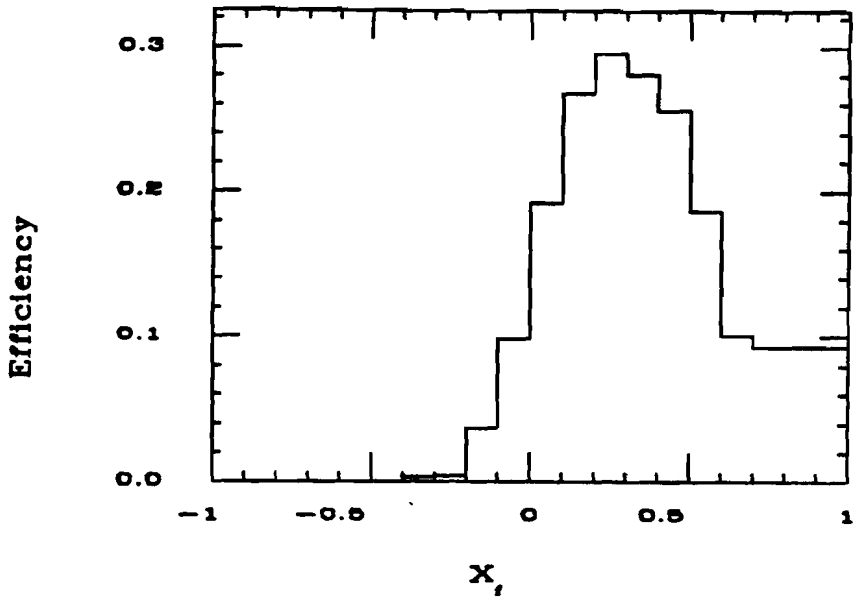

Figure 55: Average efficiency as a function of X_f for the 37 charm pairs.

with:

$$N^{-1} = \int_{-1}^{1}\int_{-1}^{1}(1 - X_f(D))^n \cdot (1 - X_f(\bar{D}))^n dX_f(D) dX_f(\bar{D}) \tag{53}$$

and:

$$X_{fPAIR} = f(X_f(D), X_f(\bar{D})) \tag{54}$$

The n value was set to the measured n from the single charm production studies [35]. The average efficiency distribution, weighted by charm pair topology, for all 37 charm pairs is shown in Figure 55. The charm pair X_f efficiency distribution is similar to that seen in the single charm distribution. The loss of efficiency for large X_f charm pairs is due to the daughter tracks occupying the densely populated forward cone of the event.

The same approach was used for the efficiency as a function of P_t^2.

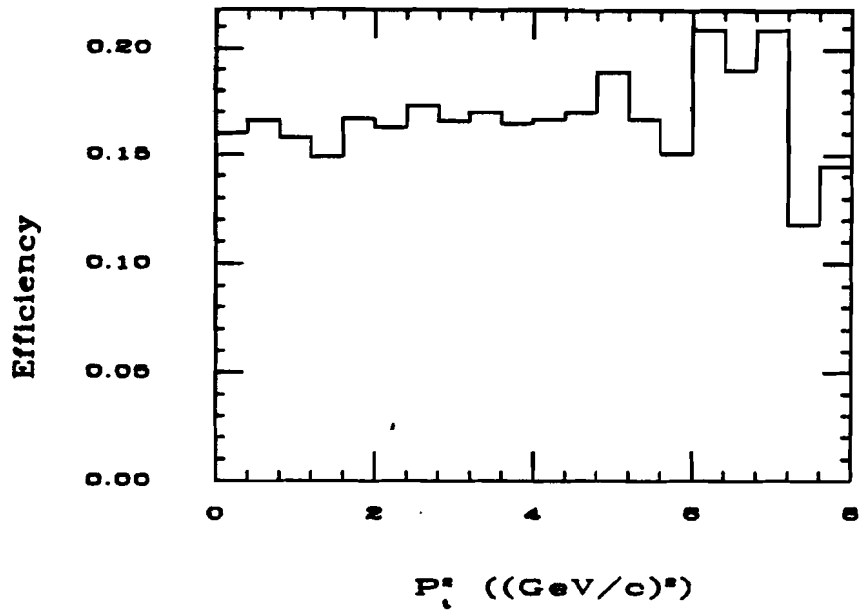

Figure 56: Average efficiency as a function of P_t^2 for the 37 charm pairs.

$$\epsilon(P^2_{tPAIR}) = \int_0^{P^2_{tmax}} \int_0^{P^2_{tmax}} N \cdot \epsilon(P_t^2(D)) \cdot \epsilon(P_t^2(\bar{D})) \cdot e^{-bP_t^2(D)} \cdot e^{-bP_t^2(\bar{D})} dP_t^2(D) dP_t^2(\bar{D}) \quad (55)$$

with:

$$N = \int_0^{P^2_{tmax}} \int_0^{P^2_{tmax}} e^{-bP_t^2(D)} \cdot e^{-bP_t^2(\bar{D})} dP_t^2(D) dP_t^2(\bar{D}) \quad (56)$$

and:

$$P^2_{tPAIR} = f(P_t^2(D), P_t^2(\bar{D})) \quad (57)$$

The value of b in the exponential was set to 1.0 $(\mathrm{GeV/c})^{-2}$ measured in the single charm distributions. The average efficiency as a function of P_t^2 is shown in Figure 56. The charm pair P_t^2 efficiency was flat for $P_t^2 < (6.0\ \mathrm{GeV/c})^2$.

For quantities that were exclusively charm pair distributions the efficiencies were

determined via Monte Carlo generated charm pairs. Individual charm mesons were generated with the appropriate differential cross section distribution. The production distributions were then *trimmed* with the known single charm reconstruction efficiencies in X_f and P_t^2. These uncorrelated accepted mesons were than used to form charm pair events. The flat Φ_t distribution of these uncorrelated pairs was trim to reproduce the Φ_t distribution seen in our data. Figure 57 shows the efficiency as a function of charm pair mass, averaged to reflect the topologies represented in the data. The same uncorrelated MC was used to obtain the rapidity gap efficiencies shown in Figure 58. The rapidity gap and charm pair mass efficiency distributions look simular because these two quantities are obtain from the same variables, X_f and P_t^2 of the individual charm. The efficiencies fall at large mass and rapidity gap because these events require a large difference in the individual X_f values and the magnitude of this gap (X_{fGAP}) is restricted by the individual charm X_f efficiency and production distribution. [1]

7.5 Validity of the Maximum Likelihood Technique

With the efficiencies understood the full maximum likelihood technique must be tested with Monte Carlo events to study any biases from the momentum estimator or efficiencies. The single charm studies are described in detail elsewhere [35]. Nichols compares the generated Monte Carlo value to the value determined via the maximum likelihood technique for the X_f and P_t^2 single charm differential cross section distributions. The

[1]The X_{fGAP} is defined as $X_{fGAP}(D\bar{D}) = |X_f(D) - X_f(\bar{D})|$. The charm pair mass and rapidity gap are strongly correlated to the X_{fGAP} and the efficiency distribution of the X_{fGAP} decreases at large X_{fGAP}.

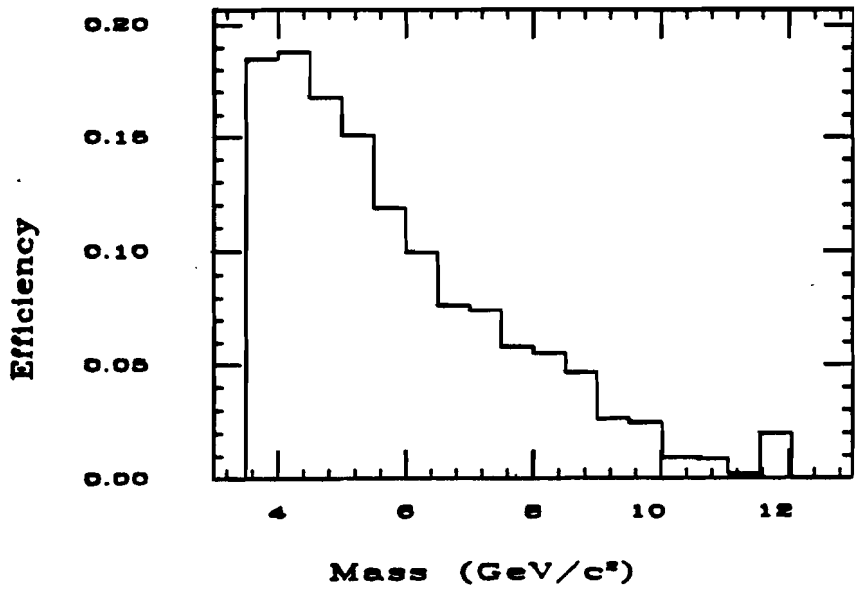

Figure 57: Average efficiency distribution as a function of charm pair mass.

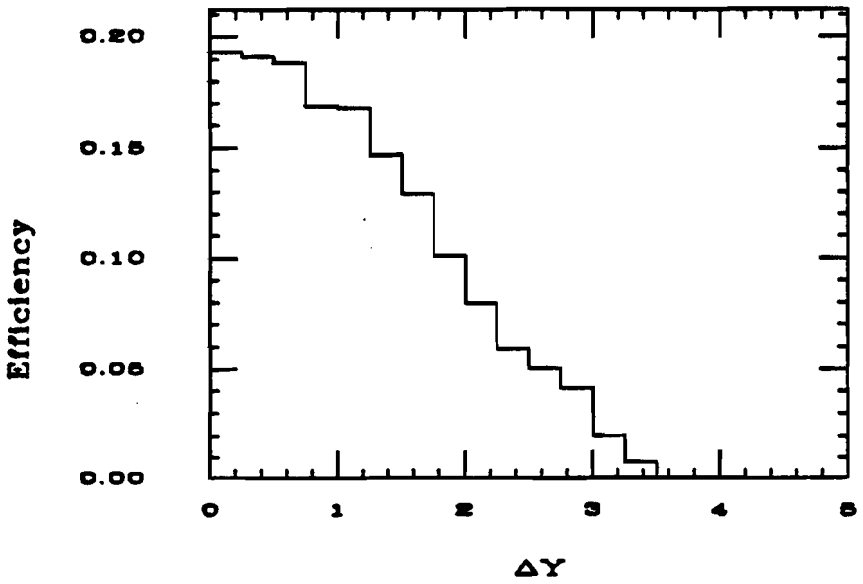

Figure 58: Average efficiency distribution as a function of charm pair rapidity gap.

comparison is quite good for the region around the values measured in the data n=10.0 and b=1.0 $(GeV/c)^{-2}$.

For the charm pair distributions the test is not as simple as comparing the input parameter to the output value since charm pairs are generated by combining individual charm mesons produced with a known production distribution. The generated production distribution for the charm pairs must also be determined by χ^2 fitting the generated distribution. The vector addition of the individual charm momentum, generated with an exponential distribution in P_t^2, does not return an exponential distribution for the pair P_t^2. It was observed that the introduction of the Φ_t distribution caused the P_t^2 distribution to become more non-exponential. For purposes of this test the correlated Φ_t distribution was removed to allow testing of the maximum likelihood technique on the charm pair distributions. The generated pair P_t^2 distribution with a flat Φ_t distribution did not return a good fit to a single exponential and this is refelected in the plot. The fact that the Monte Carlo single charm P_t^2 distributions return acceptable fits gives one confidence that the method works and can be trusted for the charm pair distributions. Figures 59 and 60 compare the generated Monte Carlo production parameters with the values returned by the maximum likelihood method. The fact that the fit for pairs generated with a flat X_f distribution did not return the proper n value can be attributed to the fact that the efficiencies at large X_f are not very well known.

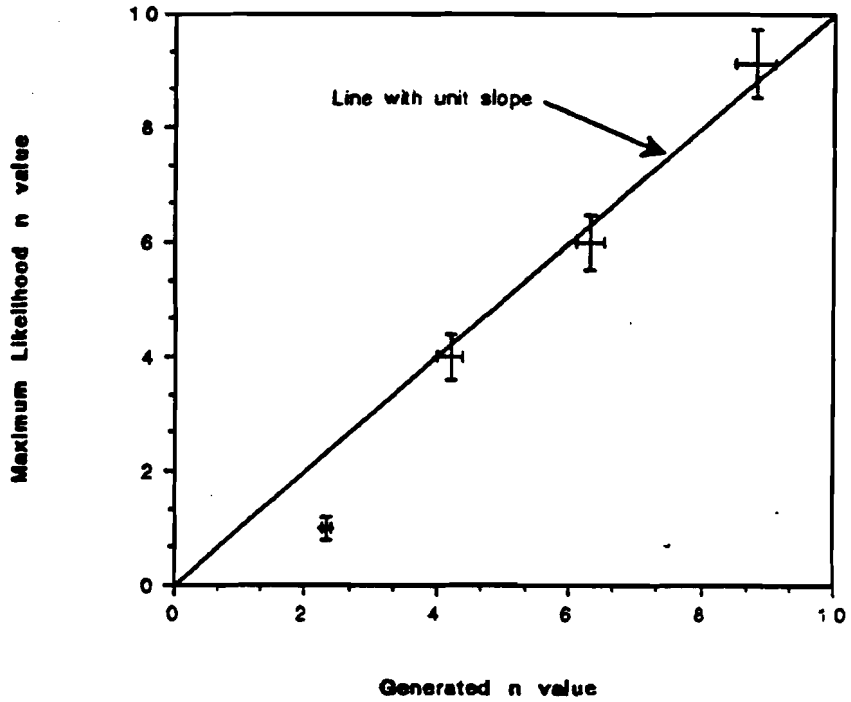

Figure 59: Comparison of the input Monte Carlo n value with that returned by the maximum likelihood method for charm pairs.

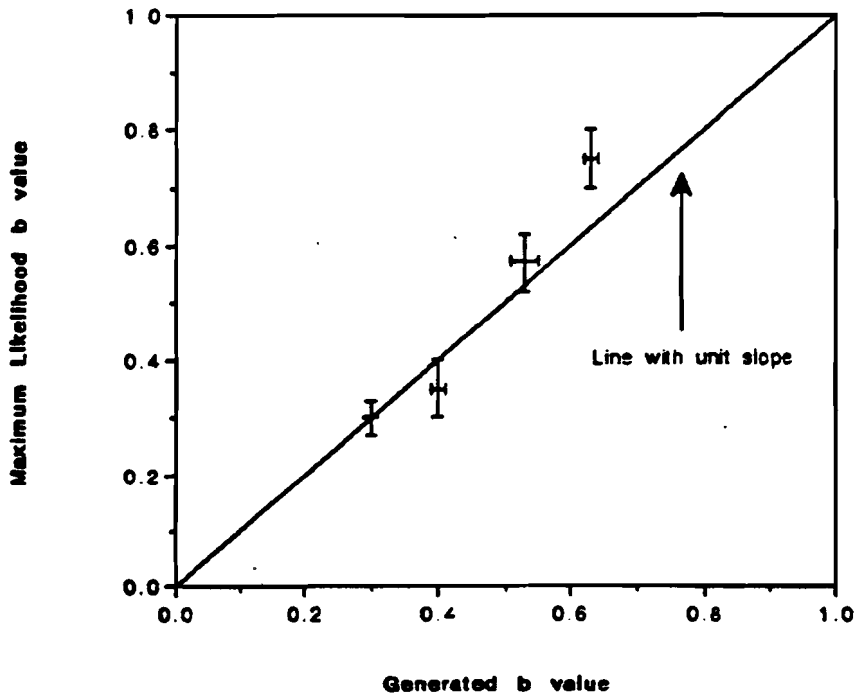

Figure 60: Comparison of the input Monte Carlo b value with that returned by the maximum likelihood method for charm pairs.

Chapter 8

Charm Pair Production and Correlation Results

8.1 Introduction

The study of charm pair production characteristics allows one to measure the kinematic quantities involved in charm production and to study production correlations within the charm pair system. The kinematic quantities of the charm pair reflect the kinematic distribution of the parton (gluon) momentum responsible for charm production. Previous experiments (LEBC-πP had 12 charm pairs and LEBC-PP had 17 pairs) were strongly limited by statistics and presented weighted distributions and their averages. The 37 charm pair events in this sample permit fits to be performed to the X_f and P_t^2 distributions of the charm pair system for the first time. In addition to fitting the differential pair cross section in X_f, P_t^2 and pair mass, the kinematic distributions are

compared to MC produced charm pairs. The averages for the measured quantities in the data are compared to those measured previously and with averages returned from the Monte Carlo generated charm pairs. A complete listing of the 37 charm pair events and the associated kinematic quantities can be found in Appendix B.

8.2 Charm Pair Monte Carlo

The data are compared to charm pairs produced by two different Monte Carlos, the LUND MC and a Φ_t correlated Monte Carlo developed by the author. The LUND MC generates charm pairs via the leading order production diagrams and is described in more detailed in Appendix A. The LUND MC uses only the leading order diagrams in the production process which account for less than a half of the cross section [9,12]. There are a number of user definable parameters in the LUND MC that allow the user to mold the charm pair distributions. With the large number of adjustable parameters and using only leading order production diagrams it is impossible to determine if agreement or disagreemant between the LUND MC and the data is just a fortuitous combination of input parameters or real physics. The LUND MC was used exhaustively by the LEBC collaboration in their charm pair analysis and the comparison of LUND MC to this data is done for completeness.

In addition to the LUND MC, the data is compared to an uncorrelated pair Monte Carlo. This Monte Carlo consisted of single charm particles generated using the measured differential production distributions in X_f and P_t^2 [35]. The two single charm particles

were then combined to form charm pairs. The azimuthal opening angle distribution, Φ_t, for these uncorrelated charm pairs was flat. The Φ_t distribution seen in our data and in the LEBC data was peaked at 180°. This Φ_t correlation was installed in the Monte Carlo, by "trimming" the Φ_t of the uncorrelated charm pairs. This "trimming" forced the charm pairs generated by this Monte Carlo to have the same Φ_t distribution that was observed in our data. This Monte Carlo will be referred to as the Φ_t *correlated Monte Carlo* throughout this section. It is important to emphasize that the correlation in Φ_t is the only correlation in the charm pair system installed in this Monte Carlo.

8.3 Pair X_f Distribution

Figure 61 shows the weighted X_f distribution for the charm pairs. The maximum likelihood fit to $(1 - X_f)^n$ yields $n = 5.0 \pm 1.5$, and this curve is represented by the solid line. Charm pairs generated with the Φ_t correlated MC yield the X_f distribution represented by the dashed histogram. A fit to the Φ_t correlated MC X_f distribution yields $n = 6.0 \pm 1.0$. The pair X_f distribution is indistinguishable from the distribution obtained from Φ_t correlated MC charm pairs. The X_f distribution for the charm pairs is uncorrelated at this level of statistics. The X_f distribution is also consistent with being symmetric about X_f=0.

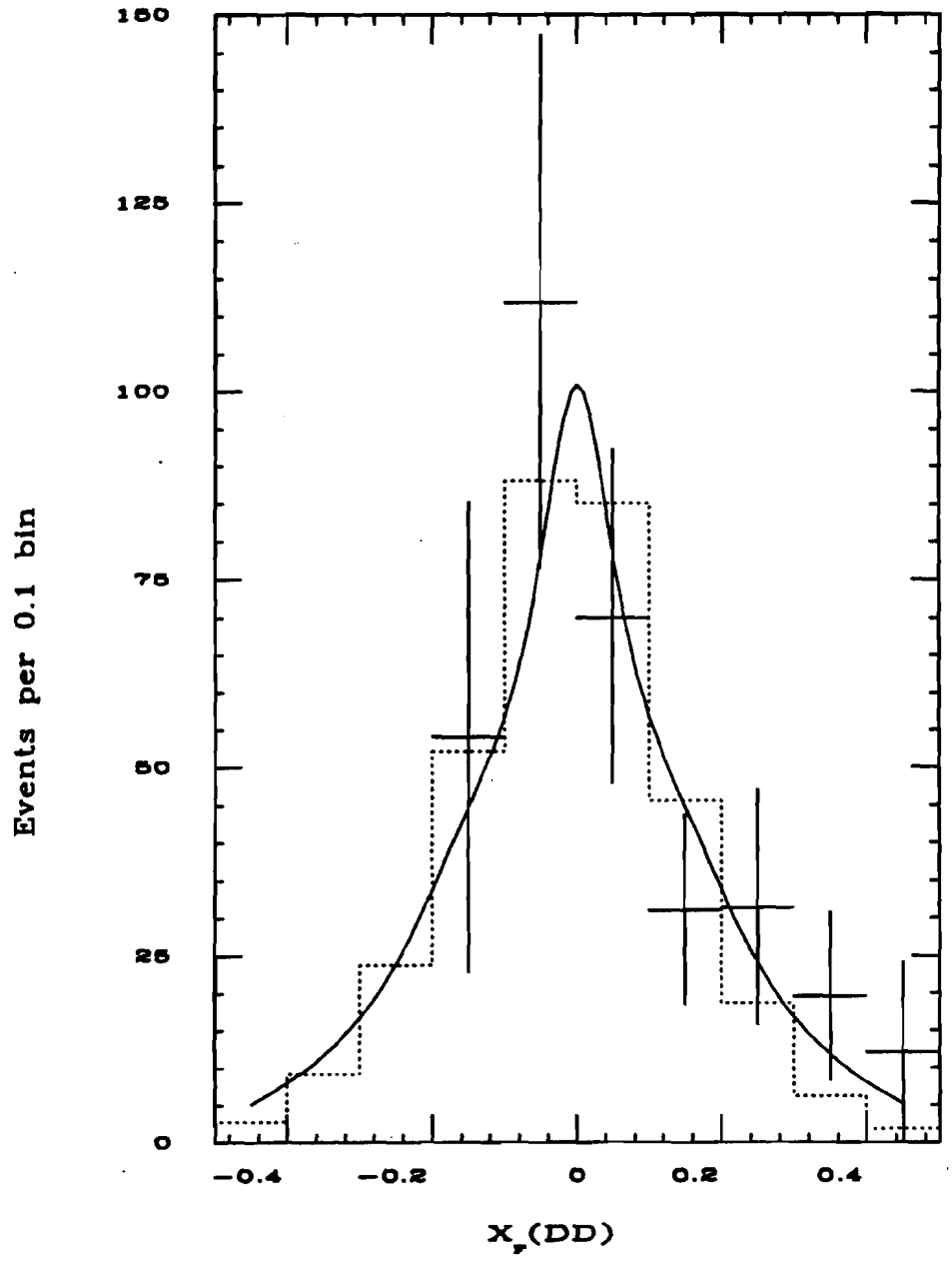

Figure 61: The X_f distribution for the 37 charm pairs. The solid line is the result of a maximum likelihood fit to $(1\text{-}X_f)^n$. The dashed histogram is from MC Φ_t correlated charm pairs.

8.4 Pair P_t^2 Distribution

The P_t^2 distribution for the charm pair was assumed to be represented by $e^{-bP_t^2}$ even though MC studies showed that correlations in the Φ_t distribution will affect the P_t^2 parameterization. Monte Carlo charm pairs generated uncorrelated kinematically but with the Φ_t angular correlation did not yield a pair P_t^2 distribution that could be represented by $e^{-bP_t^2}$. Figure 62 shows the weighted P_t^2 distribution for the 37 pairs and the solid line is the result of the fit which yielded $b = 0.65^{+0.10}_{-0.08}(GeV/c)^{-2}$. The dashed histogram is the P_t^2 distribution for MC Φ_t correlated charm pairs. The MC P_t^2 distribution does not agree with the data P_t^2 distribution at low and high P_t^2. The P_t^2 distribution shows evidence for a tail at large P_t^2. This tail could be from higher order charm production diagrams like $gg \rightarrow gq\bar{q}$ where the charm pair is produced with larger P_t^2 than the leading order 2→2 diagrams. A single exponential parameterization of the P_t^2 distribution is not valid for charm pairs with large P_t^2.

The average of the efficiency corrected P_t^2 distribution is 2.32±0.36 $(GeV/c)^2$. Figure 63 shows the $<P_t^2>$ versus s for this experiment and the LEBC-PP [51] measurement obtained at a lower value of s. In Drell-Yan di-lepton production the average P_t^2 is expected to rise linearly with s. The intercept at s=0 yields the average intrinsic k_t^2 of the partons involved in the process. Di-lepton studies measured the k_t^2 of quarks and similar measurements in charm pair analysis will measure the k_t^2 of the gluons inside the incident and target particle. Using the two measured points the intrinsic k_t^2 of the gluons involved in charm production is 0.70±0.70 $(GeV/c)^2$. This value is consistent with the value

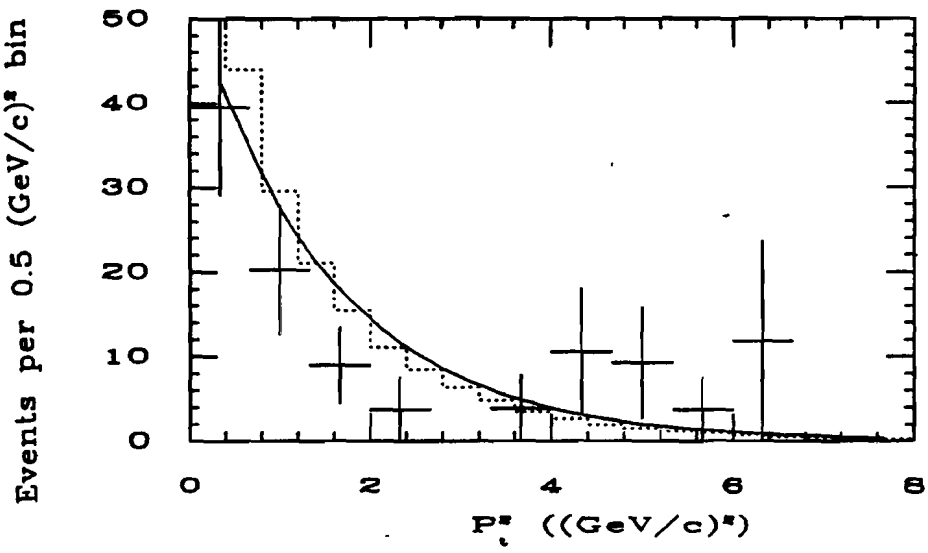

Figure 62: The weighted P_t^2 distribution for the charm pairs. The solid line is the result of a maximum likelihood fit to $e^{-bP_t^2}$. The dashed histogram is for Φ_t correlated charm pairs.

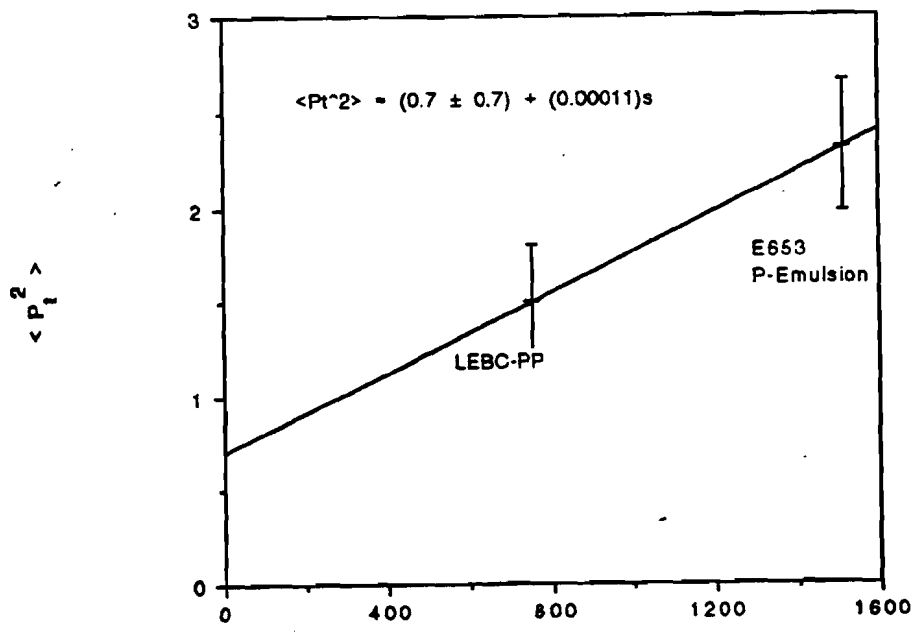

Figure 63: The $<P_t^2>$ versus s for E653 and LEBC-PP charm pairs. The curve is a least squares fit to $<P_t^2> = k_t^2 + s \cdot \text{constant}$.

measured in Drell-Yan di-lepton production [21].

8.5 Pair Azimuthal Opening Angle (Φ_t)

The azimuthal opening angle (Φ_t) of the charm pair is shown in Figure 64. The Φ_t distribution peaks at 180° - reflecting a back-to-back nature in charm production. The average of the distribution is $113.2^o \pm 9.0^o$. This value is consistent with those measured previously by LEBC (See Table 24).

8.6 Charm Pair Mass

The mass of the charm pair reflects the "q^2" of the production process. The weighted mass distribution is shown in Figure 65. The dashed histogram is for Φ_t correlated charm pairs. The solid line is the result of a maximum likelihood fit to $e^{-aM(D\bar{D})}$ without taking into account the mass resolution function. The fit yielded $a = 0.75 \pm 0.15$ $(\mathrm{GeV/c^2})^{-1}$. The parameterzation e^{-aM} was motivated by Drell-Yan di-lepton production. Di-lepton mass plots were done at constant di-lepton rapidity, due to the lack of statistics and relatively small range in rapidity for the charm pairs, all 37 charm pair events in this sample were used in the fit. By converting the exponential to $e^{-c\sqrt{\tau}}$ values for c obtained at different COM energies can be compared. It will be interesting to see how well this mass scaling holds between experiments and for large $\sqrt{\tau}$ or $M(D\bar{D})$.

The average of the weighted distribution is 4.94 ± 0.17 Ge v $/c^2$ which is slightly higher than for previous measurements. E653 with a higher COM energy has probed a higher

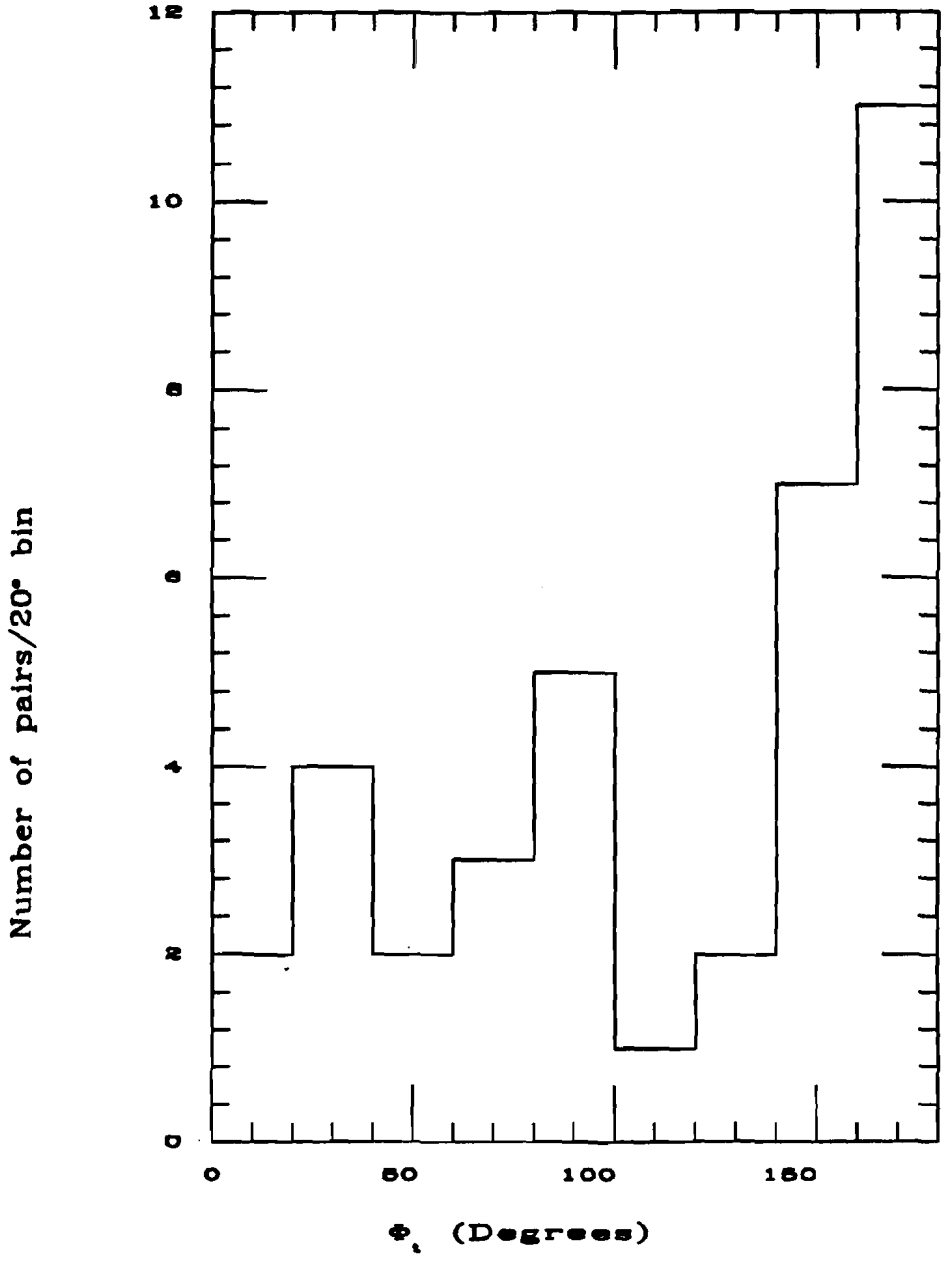

Figure 64: Φ_t (Azimuthal opening angle of the charm pair) distribution for the 37 charm pairs.

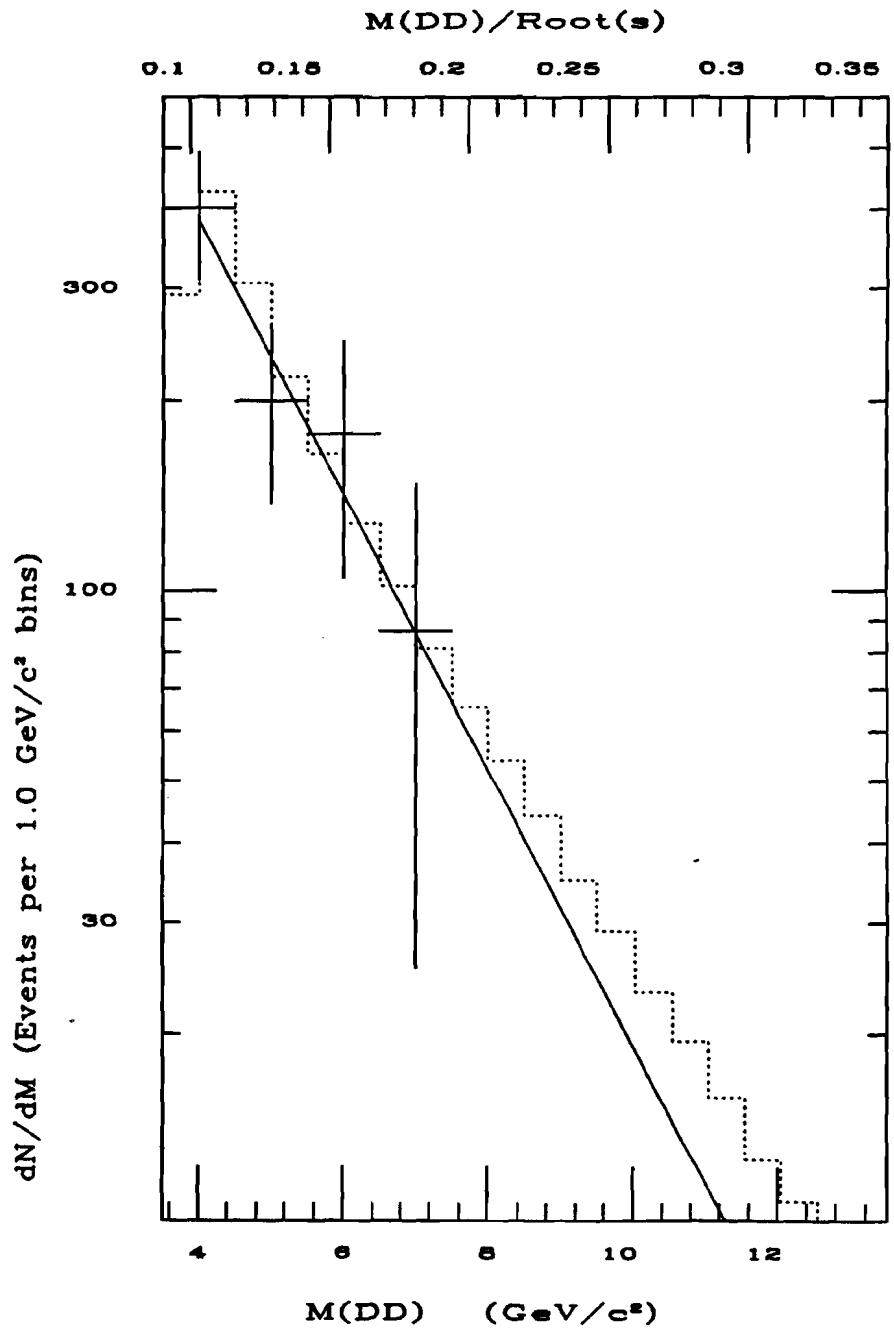

Figure 65: Charm pair mass distribution. The solid line is the result of a fit to e^{-aM}. The dotted histogram is the mass distribution obtained from the Φ_t correlated MC.

mass range than the LEBC data.

8.7 Charm Pair Rapidity Gap (ΔY)

The weighted rapidity gap distribution is shown in Figure 66. Monte Carlo Φ_t correlated charm pairs do not reproduce the ΔY distribution. The LEBC-πP charm pair ΔY distribution was slightly wider than that obtained from uncorrelated charm pairs [52]. The Φ_t correlated charm pairs have some momentum balance in the plane transverse to the beam direction due to the Φ_t correlation installed in the MC. Momentum balancing along the beam direction is not taken into account. By balancing momentum along the beam direction the rapidity gap would by broadened. Berger has pointed out that the shape of the rapidity gap depends distribution on whether the production was through $q\bar{q}$ annihilation or gg fusion, but performed the calculations only for beauty quarks [12].

8.8 Comparison to previous results

Comparison of the LEBC π-P and P-P charm pair production results with these results is shown in Table 24 [51,52]. Table 24 lists the weighted averages for the pair kinematic variables (X_f, P_t, Φ_t, mass and ΔY).

The averages of the Φ_t distributions for the three experiments agree quite well. All three averages are lower than the average returned by the Lund MC.

The average rapidity gap measured at $\sqrt{s}$=38.8 GeV has increased slightly compared to the LEBC-PP result at $\sqrt{s}$=27.4 GeV. The measurements agree within statistics. The

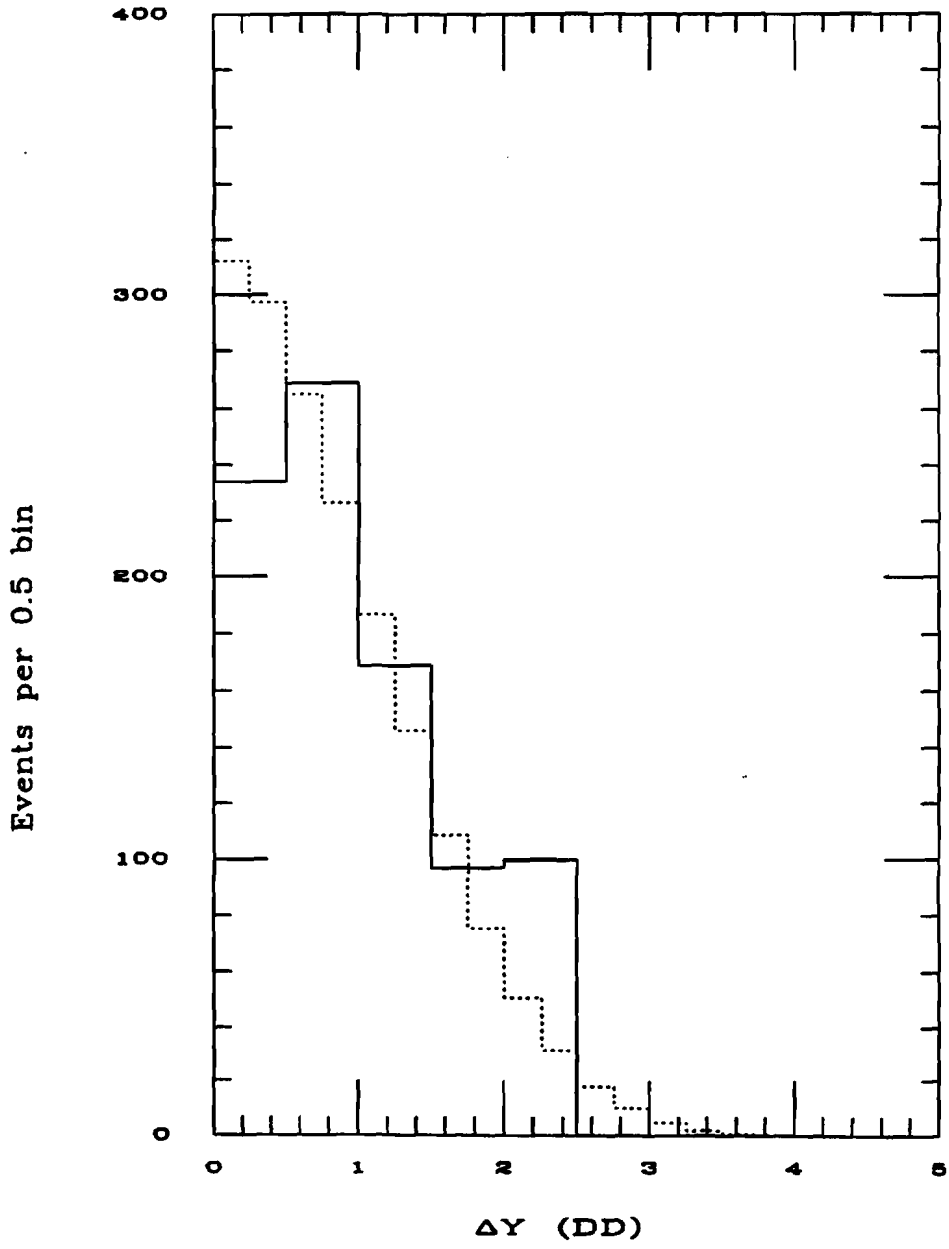

Figure 66: The rapidity gap distribution of the charm pairs. The solid histogram is for the data. The dashed histogram is for Φ_t correlated MC charm pairs.

Experiment	$\sqrt{s}$ GeV	Number of Events	$< M(D\bar{D}) >$ GeV/c^2	$< X_f(D\bar{D}) >$ ($X_f > 0$)	$< P_t^2(D\bar{D}) >$ (GeV/c)^2	$< \Delta Y >$	$< \Phi_t >$ Degrees
E653	38.8	37	4.94±0.17	0.172±0.022	2.32±0.36	1.00±0.11	113.2±9.0
P-Emulsion							
Φ_t			4.71	0.13	1.52	0.87	113.5
Correlated MC							
LUND			5.67	0.18	1.17	1.37	121
LEBC-PP	27.4	17	4.65±0.13	0.18±0.03	1.50±0.30	1.02±0.12	105±5
							105 events
LUND			4.82	0.19	0.88	0.98	119
LEBC-πP	26.0	12	4.50±0.16	0.25±0.07	1.65±0.40	0.80±0.14	115±8
							57 events
LUND			4.60	0.25	0.75	0.77	126

Table 24: Comparison of weighted average values measured in two previous charm pair experiments and the values presented in this thesis.

$<P_t^2>$ reported here is larger than for the LEBC-PP measurement and this can be attributed to a Drell-Yan like scaling of the average P_t^2 with s. The $<P_t^2>$ value returned from the LUND MC does not agree with any of the charm pair measurements.

The average $<X_f>$ measured at $\sqrt{s}$=38.8 GeV and 27.4 GeV agree remarkably well. This is especially surprising since the single charm production results from E653 and LEBC-PP do not agree [35,50].

The $< M >$ for the charm pairs is expected to rise with larger values of $\sqrt{s}$. This rise is seen when comparing the $< M >$ measured by the three charm pair experiments. Charm production at high $< M >$ or high q^2 can be more easily treated theoretically by using perturbative methods. A high statistics charm pair experiment would allow the study of charm production in the purely perturbative region (high charm pair mass) and connect to the non-perturbative region (low charm pair mass). E653 has insufficient statistics to do this analysis, however, the increase in $< M >$ gives one hope that such an experiment

is possible (E653-RUNII).

Chapter 9

Conclusions

A complete analysis of hadronic production of 37 charm pairs has been presented. The differential cross section for the charm pairs was fit to the following empirical formula:

$$\frac{d\sigma}{dX_f dP_t^2} \sim (1- \mid X_f \mid)^n e^{-bP_t^2} \tag{58}$$

and the values for n and b were determined to be:

- n= 5.0 ± 1.5
- b= $0.65^{+0.10}_{-0.08}$ (GeV/c)$^{-2}$

The X_f distribution for the charm pairs is consistent with the distribution obtained from MC Φ_t correlated generated charm pairs. The measured value of $<X_f>|_{X_f>0}$ was consistent with previously measured values done at lower $\sqrt{s}$. This is in contrast to single charm production distributions, which showed a much more central production at

$\sqrt{s}$=38.8 GeV than the distribution observed at $\sqrt{s}$=27.4 GeV. The n value measured for the pair X_f distribution is consistent with that obtained from the Φ_t correlated MC, which used single charm produced with the central production distribution measured in the data. The P_t^2 distribution for the charm pairs was seen to have a tail at high (P_t^2 > 3.0 (GeV/c))^2, that was not reproduced by the Monte Carlo. The high P_t^2 tail could be an indication of next to leading order two to three processes in charm production, $gg \rightarrow gq\bar{q}$. This could be confirmed by the presence of hadronic jets recoiling against the charm pair system. The data did not present enough statistics to search for such jets. The $<P_t^2>$ was consistent with the measured value from Drell-Yan di-lepton production with 800 GeV/c protons,$<P_t>$=1.61±0.16 GeV/c [64]. The $<P_t^2>$ from this experiment was compared to the previously measured value of the LEBC-PP experiment as a function of the center of mass energy squared. This comparison was motivated by the Drell-Yan model and allowed the $<k_t^2>$ of charm production to be measured [21]:

- $<k_t^2> \sim 0.70 \pm 0.70$ (GeV/c)^2.

This intrinsic $<k_t^2>$ measurement reflects the transverse momentum of the partons responsible for charm production and the transverse momentum associated with the fragmentation of the charm quarks into mesons. This value is in agreement with the $<k_t^2>$ used by LEBC in the LUND MC for consistency between the data and the MC. The LUND MC does not reproduce the same slope when the $<P_t^2>$ is represented by $<P_t^2> = <k_t^2> + C \cdot s$.

The charm pair mass distribution has a slightly higher <M($D\bar{D}$)> than the average pair mass measured at lower $\sqrt{s}$. This trend is important for future experiments that hope to explore the perturbative regime of charm production. The mass distribution was seen to fit an exponential distribution:

$$\frac{d\sigma}{dM} \sim e^{-aM} \tag{59}$$

with:

- a = 0.75±0.15 $(\mathrm{GeV/c^2})^{-1}$

or:

$$\frac{d\sigma}{d\sqrt{\tau}} \sim e^{-c\sqrt{\tau}} \tag{60}$$

with:

- c = 29.1±5.8.

This mass scaling will allow charm pair experiments at different energies to compare results. The LEBC-PP data is consistent with this result, within the limited statistics. The value is also consistent with that found in di-lepton production in proton-platinum interactions, c= 27.02±0.16 at $\sqrt{s}$=27.4 GeV [22]. The variable $\tau=\frac{M(D\bar{D})^2}{s}=x_a x_b$ allows one to study the momentum fraction, x_a and x_b, of the partons involved in the reaction. At this level of statistics the gluon distribution appears to be equivalent to that measured for the quarks in di-lepton production.

The azimuthal opening angle Φ_t peaks as expected at 180°. However the $< \Phi_t >$ is lower than expected from first order production diagrams (LUND). All three charm pair

production experiments have measured $< \Phi_t >$ to be lower than the LUND MC value. The Φ_t distribution is dependent on the production diagrams and the intrinsic k_t^2 of the partons responsible for charm production. The lower measured $< \Phi_t >$ would indicate either a larger intrinsic $<k_t^2>$ for the gluons involved in heavy quark production than that used in the LUND MC or contributions from the next to leading order preduction diagrams not installed in the LUND MC.

The statistics limited the strength of the analysis. The observation of charm pair mass and $<P_t^2>$ scaling will aid in future comparisons of charm pair data, if this scaling holds. The analogy to Drell-Yan di-lepton production provides some hope that charm pair physics will allow access to the structure functions and intrinsic transverse momentum of the partons (gluons) involved in the charm production process. To do such analysis one would need a large sample of charm pairs, the data from the second run of E653 should have an order of magnitude more charm pairs produced with an incident π beam. In addition the angular distributions center of mass of the charm pair with respect to the target or beam direction can be determined. These angular distributions will provide some insight as to the underlying diagrams responsible for charm production.

Appendix A

The Lund Monte Carlo

The LUND Monte Carlo (MC) is an all purpose high energy physics Monte Carlo simulation. The LUND MC allows the user to define the initial conditions, incident particles, experimental configuration (colliding beams or fixed target) and the reaction of interest (charm production). The LUND MC generates charm via the leading order diagrams and in light of the cross section calculation of Nason, Dawson and Ellis [9] the LUND MC results for charm production are not reliable.

For charm production the user has several switches and initial values that can be change to test their effect on charm production. The important switches are:

- Structure functions of the partons in the incident beam and target. The user can define his/her own structure functions or use one of the seven sets installed in the MC.

- Fragmentation functions used to from mesons and hadrons from the bare quarks.

- The intrinsic k_t distribution and width of the partons.

The LEBC-πP and LEBC-PP results were compared to the distributions generated by the LUND MC. The LEBC results agreed best with the LUND MC when the using the EHLQ set 1 structure functions [16], lund fragmentation and an intrinsic k_t^2 parameterized by:

$$\frac{dN}{dk_t^2} \sim e^{-\frac{k_t^2}{0.64 \ (GeV/c)^2}}. \tag{61}$$

The following set of histograms compares the distributions of the 37 charm pairs to those obtained by running the LUND MC in the same configuration used for the LEBC analysis, with the one exception that the intrinsic $<k_t^2>$ of the partons was set to 0.70 $(GeV/c)^2$. Figures 67 through 71 show good agreement between our data for the 37 charm pairs and the distributions from the LUND MC. The one possible difference is the tail in the P_t^2 distribution for the data. LEBC-PP data also was inconsistent with LUND MC at large P_t^2. However with error bars on their plots it hard to determine the statistical significance of their tail. The averages from these distributions were tabulated in Table 24.

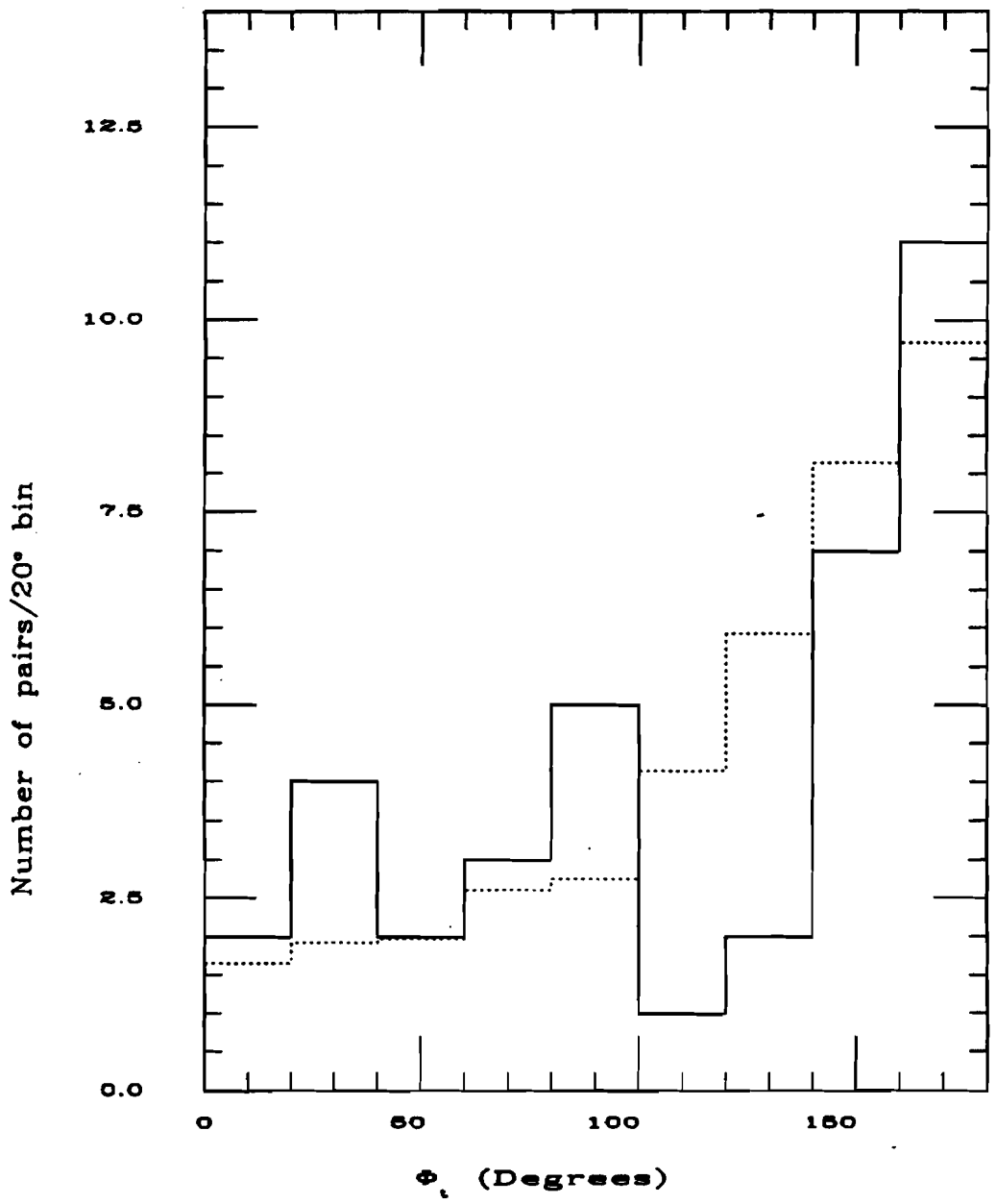

Figure 67: The Φ_t distribution for the 37 charm pairs (solid) and the LUND MC (dots).

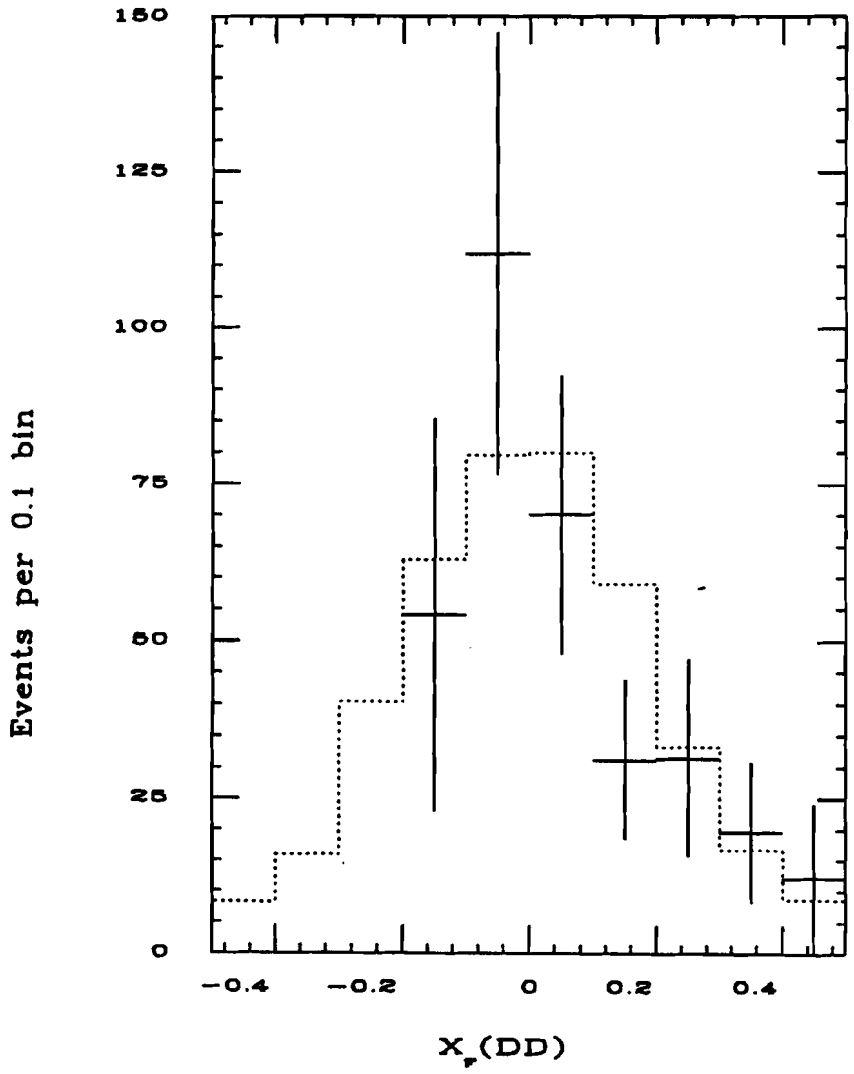

Figure 68: The weighted X_f distribution for the 37 charm pairs (solid) and the LUND MC (dots).

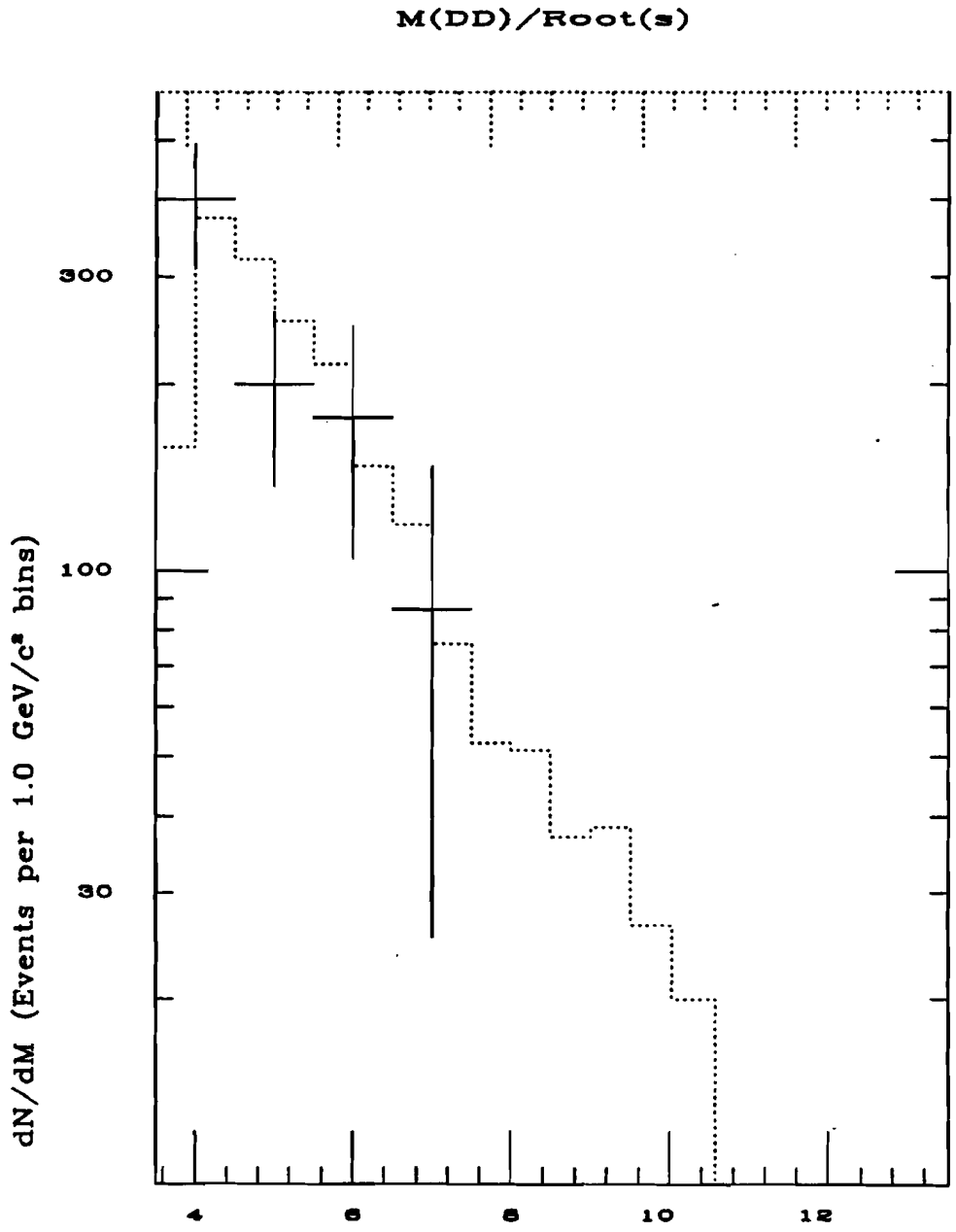

Figure 69: The weighted charm pair mass distribution. Data (solid). LUND MC (dots).

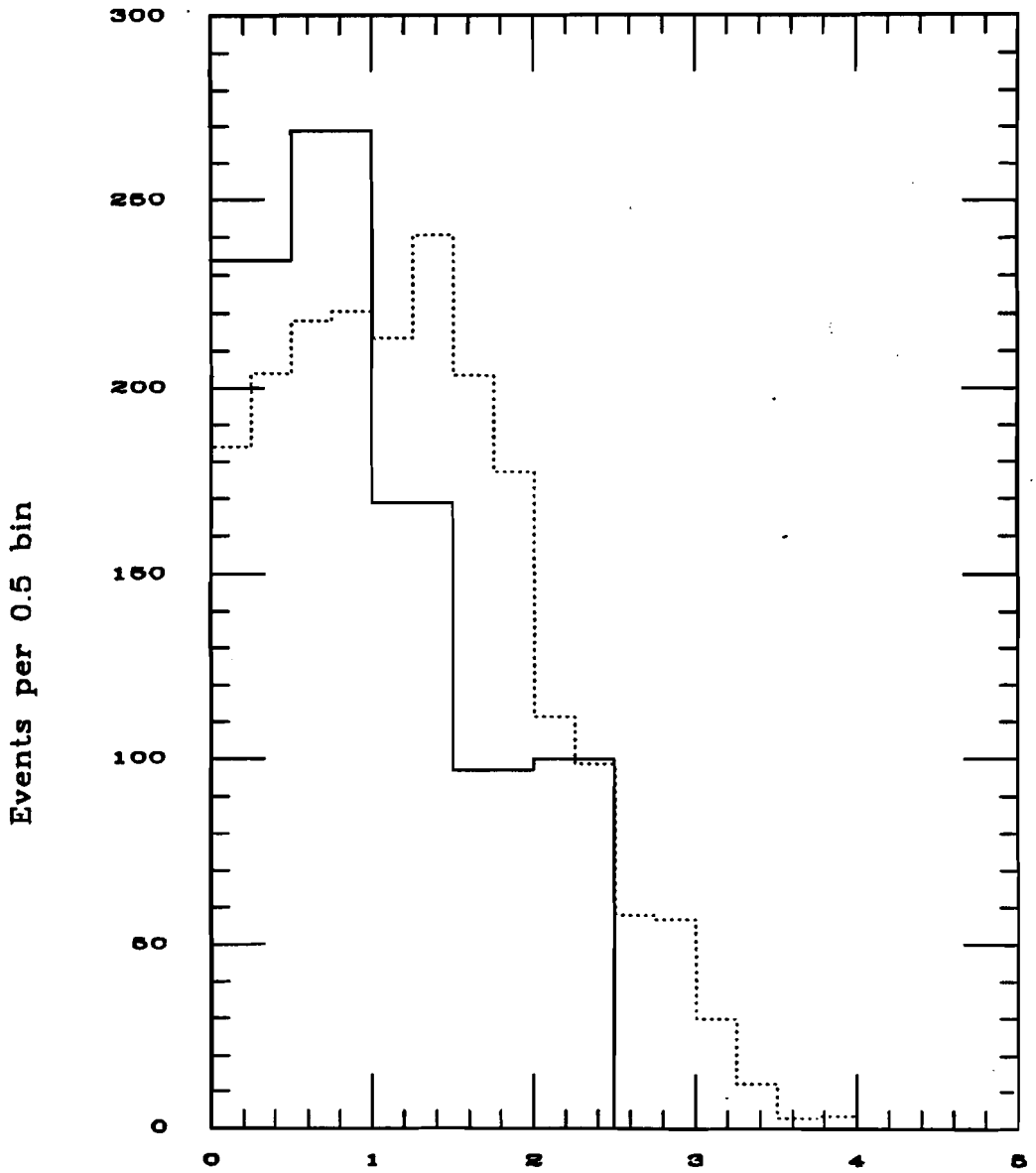

Figure 70: The weighted rapidity gap distribution for the 37 charm pairs (solid) and that obtained from the LUND MC (dots).

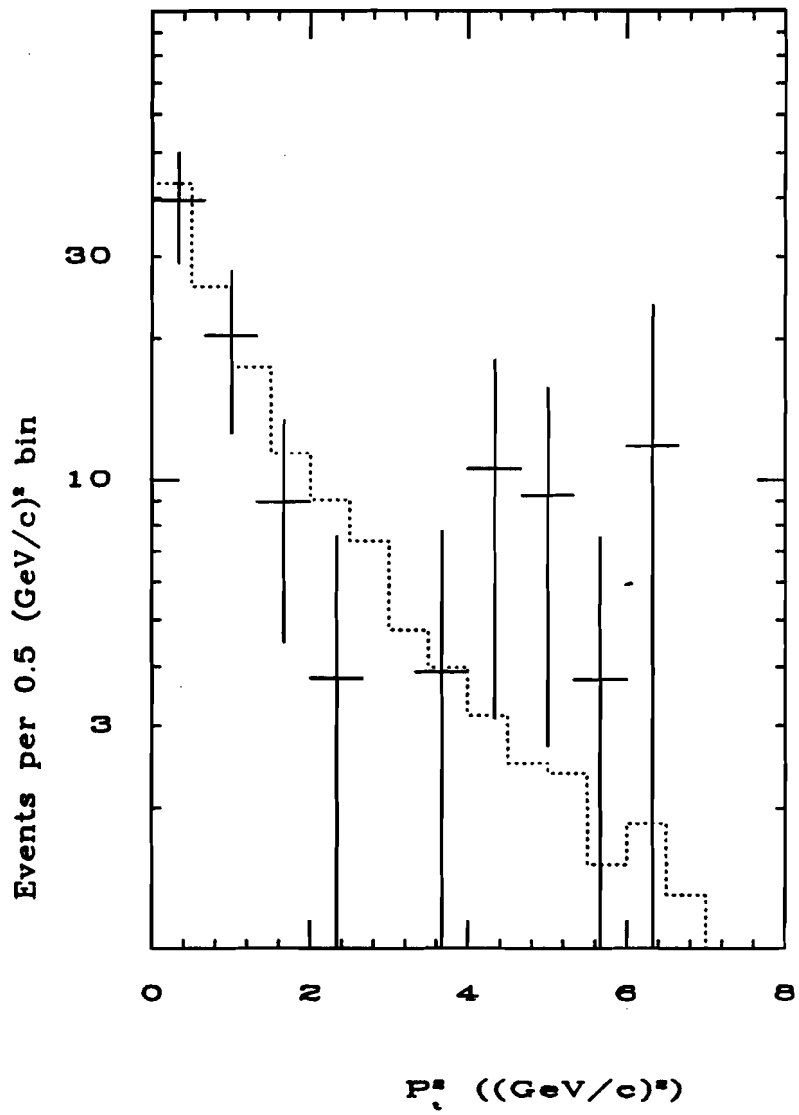

Figure 71: The weighted P_t^2 distribution for the 37 charm pairs (solid) and the LUND MC charm pairs (dots).

Appendix B

Event listings

The kinematic quantities for the 37 charm pair events are listed in the following table. The table is deciphered as follows: The first row is the accounting row. The first number is the running sum of pair events, it starts at one and ends at 37. The next number is the run number of the event and corresponds to the raw data tape number the event was recorded on. This run number is followed by the event number of the pair.

The next row contains the kinematic information on one of the charm that compose the charm pair. The first number is the decay topology:

- 3 → V-2
- 4 → V-2μ
- 5 → C-3
- 6 → C-3μ

- 7 → V-4.

The second number is the minimum parent mass of the vertex followed by its error (GeV/c2). The fourth and fifth numbers are the momentum estimate and "error" for the decay (GeV/c). The error is listed as a guide and one should remember that it is a non-gaussian error distribution. The sixth number is the X_f of the parent. The seventh number is the P_t^2 of parent and the eigth number is the rapidity, y.

The next row contains the same information for the second charm decay in the charm pair. The final row contains the charm pair quantities. The first number is the azimuthal opening angle of the pair, Φ_t(degrees). The pair mass is the second number in the row (GeV/c^2). The third number is the charm pair momentum (GeV/c). The forth is the X_f of the charm pair and the fifth number is P_t^2 of the charm pair (GeV/c^2). The sixth number is the $\mid \Delta Y \mid$ of the charm pair.

```
     1.0        1427.0        3490.0
  5.00000      1.93096      0.09856     87.13405     15.68413      0.06549      3.75843      4.17099
  4.00000      1.92359      0.01533    122.01445     31.72375      0.13036      1.95655      4.65092
 23.06048    3.99708  209.14452    0.19613   10.70512    0.47994

     2.0        1478.0         690.0
  5.00000      1.74464      0.02336     28.25097      6.21521     -0.04253      0.63327      3.32828
  4.00000      1.90725      0.10002    274.93817     65.98517      0.33921      0.90179      5.57169
 95.90720    6.89611  303.17853    0.30353    1.37947    2.24341

     3.0        1548.0        1093.0
  4.00000      1.45203      0.04262     35.41876     11.33401     -0.01964      0.76430      3.53834
  3.00000      1.69090      0.01291     27.60866      7.17825     -0.03782      0.25755      3.35335
 98.51592    3.89700   63.01903   -0.05751    0.89043    0.18499

     4.0        1588.0        2967.0
  5.00000      1.76203      0.05273    114.49224     20.60860      0.11341      3.20124      4.48412
  6.00000      1.51629      0.11534     59.82734     13.16201      0.00659      4.19734      3.76555
175.86241    5.69607  174.27077    0.12153    0.08643    0.71857

     5.0        1593.0        1341.0
  6.00000      1.63109      0.01477     69.81738     13.96348      0.05262      1.15259      4.17282
  3.00000      1.14330      0.06236    316.90582    101.40988      0.37024     14.52932      5.00623
 92.09747    5.67685  386.71194    0.42815   15.38224    0.83341

     6.0        1601.0         994.0
  3.00000      1.50767      0.23629     43.36339     13.00901      0.00255      0.73642      3.74383
  4.00000      1.88111      0.06767    174.57625     34.91525      0.20443      1.83839      5.02003
174.70398    5.25051  217.92645    0.20889    0.25765    1.27620

     7.0        1617.0         552.0
  3.00000      2.01921      0.10317     64.48354     12.89671      0.05081      0.20837      4.20744
  4.00000      1.71746      0.17298    242.45352     63.03793      0.29783      0.51050      5.49231
173.91173    4.74548  306.93451    0.35067    0.07026    1.28487

     8.0        1715.0         183.0
  4.00000      1.57187      0.02339     85.03851     27.21233      0.08194      0.57088      4.43714
  3.00000      1.79649      0.01383     14.33148      2.57967     -0.13016      0.48453      2.67075
 57.19571    5.52307   99.35789   -0.04877    1.62539    1.76638

     9.0        1743.0        3918.0
  3.00000      1.42502      0.17455     85.34445     27.31023      0.07385      1.92886      4.29611
  4.00000      1.62852      0.02251     37.98555     11.39566     -0.00142      0.01577      3.70542
140.95499    4.18078  123.32529    0.07261    1.67380    0.59070
```

Table 25: Event listings for the 37 charm pairs.

10.0	1759.0	2267.0					
4.00000	1.27194	0.05471	72.79432	26.20596	0.06552	0.11483	4.34143
7.00000	2.15961	0.01367	83.00803	1.66016	0.06973	1.96080	4.26543
177.16096	4.09512	155.79338	0.13550	1.12781	0.07600		
11.0	1764.0	2056.0					
7.00000	1.60810	0.07330	22.61984	8.59554	-0.05631	0.09730	3.17657
4.00000	1.40857	0.02543	49.59491	16.86227	0.02127	0.34313	3.92701
61.15745	4.04392	72.21342	-0.03508	0.61674	0.75044		
12.0	1793.0	3696.0					
3.00000	1.16207	0.09573	19.20057	6.14418	-0.08205	0.32367	2.98247
4.00000	1.34728	0.02562	158.10300	50.59296	0.18812	0.00674	5.13210
174.70876	6.22211	177.29578	0.10788	0.23743	2.14963		
13.0	1797.0	4749.0					
7.00000	1.82931	0.03855	56.34149	11.26830	0.02616	1.24379	3.94861
4.00000	1.15360	0.06777	52.51207	18.90435	0.01093	1.93524	3.80989
157.48933	4.47554	108.82554	0.03726	0.31259	0.13873		
14.0	1817.0	111.0					
6.00000	1.89743	0.06462	154.57170	30.91434	0.18006	0.96376	4.98846
7.00000	2.08734	0.01971	95.12917	5.70775	0.08656	2.48787	4.35536
67.14605	4.26493	249.69397	0.26736	4.65448	0.63309		
15.0	1852.0	4225.0					
4.00000	1.64300	0.07569	88.78966	26.63689	0.02067	11.62501	3.82170
5.00000	1.65622	0.00911	45.04368	9.90961	-0.00051	1.33337	3.71553
153.81055	5.58273	133.77509	0.02039	5.89351	0.10618		
16.0	1860.0	2048.0					
7.00000	1.74416	0.17750	40.16079	8.83537	0.00380	0.03090	3.75888
4.00000	1.32469	0.02290	43.24200	14.70228	0.00869	0.22032	3.80643
111.47408	3.77240	83.40100	0.01249	0.19081	0.04755		
17.0	1864.0	255.0					
5.00000	1.35189	0.24541	149.91859	41.97720	0.17512	0.56509	5.00486
6.00000	1.71829	0.03561	89.64539	16.13617	0.08294	1.59276	4.37723
167.29909	4.43837	239.55386	0.25907	0.30683	0.62763		
18.0	1864.0	2992.0					
3.00000	1.80846	0.09567	54.32148	9.77787	0.03295	0.13311	4.04632
4.00000	1.81510	0.02875	22.03082	3.08432	-0.07101	0.57511	3.08732
20.33675	4.22935	76.34605	-0.03818	1.22713	0.95900		

Table 26: Event listings for the 37 charm pairs continued from the previous page.

Table 27: Event listings for the 37 charm pairs continued from the previous page.

19.0	1890.0	4535.0					
4.00000	1.97935	0.03173	43.62052	11.34134	-0.03465	3.79812	3.47631
7.00000	1.89180	0.01332	39.83442	7.17020	-0.00936	0.94511	3.63481
15.40521	3.84602	83.44985	-0.04404	8.39628	0.15850		
20.0	1946.0	3428.0					
7.00000	1.64429	0.09159	141.44241	48.09042	0.15307	3.30989	4.68738
4.00000	1.68161	0.03736	172.42091	48.27786	0.20670	0.17200	5.19572
23.47703	4.10297	313.85889	0.36048	4.86604	0.50834		
21.0	2002.0	1266.0					
7.00000	2.15310	0.25266	13.92023	1.11362	-0.13058	0.36989	2.65668
4.00000	1.61335	0.05360	44.01796	14.08575	0.00487	0.67810	3.76577
179.01009	4.62620	57.91759	-0.12634	0.04647	1.10909		
22.0	2041.0	2966.0					
5.00000	2.27513	0.11011	82.31474	16.46295	0.04459	5.61987	3.99958
6.00000	1.84925	0.01519	46.97463	3.75797	0.01841	0.10212	3.90538
56.85925	4.19483	129.27946	0.06315	6.55013	0.09420		
23.0	2044.0	4147.0					
3.00000	1.25786	0.00625	16.40056	4.92017	-0.09356	0.01648	2.86804
6.00000	1.74032	0.02341	106.27325	17.00372	0.11600	0.16096	4.71330
73.76344	5.48332	122.67339	0.02268	0.20624	1.84526		
24.0	2058.0	2408.0					
5.00000	1.99630	0.15818	35.30770	6.35538	-0.01305	0.30985	3.59192
4.00000	1.73466	0.01853	32.89956	7.89589	-0.04988	2.11479	3.32616
39.15942	4.09227	68.18661	-0.06304	2.16712	0.26576		
25.0	2059.0	4569.0					
4.00000	1.75257	0.02990	61.72466	13.57943	0.03540	1.41598	4.02191
3.00000	1.62288	0.02522	20.69181	5.79371	-0.14490	3.09731	2.78142
152.20175	5.64963	82.33492	-0.11086	0.80849	1.24048		
26.0	2081.0	60.0					
5.00000	1.58747	0.20903	66.53959	15.96951	0.05159	0.54937	4.19454
4.00000	1.53971	0.04102	50.97038	16.31052	0.02559	0.20530	3.97274
149.69292	3.92799	117.50457	0.07727	0.17480	0.22180		
27.0	2103.0	1889.0					
4.00000	1.16193	0.03786	57.25332	20.61119	0.02638	1.41949	3.94639
3.00000	1.58068	0.02795	78.65269	23.59581	0.06779	1.15360	4.29178
123.97546	4.29946	135.89049	0.09447	1.14282	0.34538		

```
     28.0        2108.0        1636.0
  4.00000      1.70516      0.03364     28.92048      7.51932     -0.04987      1.16963      3.29018
  3.00000      1.96442      0.11185    198.37790     35.70802      0.22815      4.91801      4.91961
167.31583    6.68696  227.26886    0.18208    1.40812    1.62942

     29.0        2110.0        2432.0
  3.00000      1.85959      0.02549     20.94759      2.51371     -0.07652      0.53809      3.04166
  4.00000      1.84218      0.02990     77.44447      7.74445      0.07156      0.32188      4.37532
166.87434    4.86038   98.37738   -0.00501    0.04935    1.33366

     30.0        2113.0          21.0
  5.00000      1.51082      0.12462     56.79272     14.76611      0.02618      1.33952      3.94658
  4.00000      2.10139      0.13743    230.69127     55.36589      0.26159      9.46247      4.85402
 10.65471    4.76509  287.48267    0.28949   17.79963    0.90744

     31.0        2113.0        1715.0
  3.00000      1.27963      0.03822     25.15836      7.54751     -0.07486      1.51132      3.11545
  4.00000      1.61629      0.00722     46.12259     13.83678      0.01740      0.03184      3.89701
123.81406    4.27310   71.25967   -0.05761    1.29892    0.78156

     32.0        2132.0        3632.0
  5.00000      1.56977      0.01418     50.57167     12.13720     -0.02034      4.43909      3.58191
  4.00000      1.41185      0.02708     99.41072     33.79964      0.10641      0.09310      4.65598
151.46968    5.04699  149.94934    0.08673    3.40283    1.07407

     33.0        2250.0         423.0
  4.00000      1.80002      0.03440     15.62780      2.50045     -0.10760      0.23266      2.78987
  3.00000      1.38666      0.03144     63.17276     20.21528      0.02981      2.40044      3.95343
 20.22398    4.68678   78.79971   -0.07823    4.03560    1.16356

     34.0        2250.0        3759.0
  5.00000      1.41475      0.01742     31.96967      7.67272     -0.02717      0.54028      3.46320
  4.00000      1.46139      0.04053    119.21696     35.76508      0.13242      0.59216      4.77226
153.76848    4.90312  151.17607    0.10597    0.11769    1.30906

     35.0        2282.0        4153.0
  6.00000      1.71205      0.04597     38.94454      7.01002     -0.01897      1.45919      3.55719
  3.00000      1.72791      0.04417     26.60236      6.38457     -0.11354      3.79272      2.98209
 92.62807    4.60366   65.49523   -0.13318    5.03669    0.57510

     36.0        2324.0        3025.0
  4.00000      1.68205      0.07126     32.88001      9.20640     -0.03690      1.31842      3.40254
  4.00000      2.08161      0.06139     24.31193      6.32110     -0.05298      0.30913      3.21962
174.22079    4.11022   57.16865   -0.09005    0.35734    0.18292

     37.0        2333.0        4839.0
  3.00000      1.12986      0.01674     53.75445     16.12634      0.03056      0.26174      4.01829
  6.00000      1.82286      0.01438     47.69790      3.81583     -0.00530      2.33723      3.67788
161.83765    4.27970  101.43089    0.02534    1.11271    0.34041
```

Table 28: Event listings for the 37 charm pairs continued from the previous page.

Aw Mama can this really be the end...[65]

Bibliography

[1] G. Arnison *et.al.*, Phys. Lett. **122B** 103 (1983).

[2] M. Banner *et.al.*, Phys. Lett. **122B** 476 (1983).

[3] F. Abe *et.al.*, Phys. Rev. Lett. **63** 720 (1989).

[4] G.S. Abrams *et.al.*, Phys. Rev. Lett. **63** 724 (1989).

[5] D.H. Perkins. *Introduction to High Energy Physics*, Addison-Wesley Publishing Company, pg. 15 (1982).

[6] D. Decamp *et.al.*, Phys. Lett. **235B** 399 (1990).

[7] B. Aveda *et.al.*, Phys. Lett. **237B** 136 (1990).

[8] F. Abe *et.al.*, Phys. Rev. Lett. **64** 142 (1990).

[9] P.Nason,S.Dawson and R.K. Ellis., Nuclear Physics **B303** 607 (1988).

[10] S.J. Brodsky, J.F. Gunion and D.E. Soper, Phys. Rev. D. **36** 2710 (1988)

[11] J.C. Collins, D.E. Soper and G. Sterman, Nuclear Physics **B263** 37 (1986).

[12] E.L. Berger, Phys. Rev. **D37** 1810 (1988).

[13] E.L. Berger, *Heavy Flavor Production.* Proceedings of the Advanced Workshop on QCD Hard Processes, St. Croix (1988).

[14] E.L. Berger, *Heavy Quark Production in Hadron Collisions.* Proceedings of the XXII Rencontre de Moriond, Les Arcs, France (1987).

[15] D.W. Duke and J.F. Owens, Phys. Rev. **D30** 49 (1984).

[16] E. Eichen *et. al.*, Rev. Mod. Phys. **56** 667 (1984).

[17] J.P. Rutherford, *Hadronic Production of Real and Virual Phons.* Proceedings of the 1985 International Symposium on Lepton and Photon Interactions at High Energies, Kyoto, Japan (1985).

[18] S. Faciano *et.al.*, Z. Phys. C **31** 513 (1986).

[19] S.D. Drell and T.M. Yan, Phys. Rev. Lett. **25** 316 (1970).

[20] I.R. Kenyon, Rep. Prog. Phys. **45** 1261 (1982).

[21] B. Cox and P.K. Malhotra, Phys. Rev D **29** 63 (1984).

[22] D.M. Kaplan *et. al.*, Phys. Rev. Lett. **40** 435 (1978).

[23] J. Orear, UCRL-8417, Aug. 13 1958. *Notes on Statistice for Physicists.*

[24] D.B. Gibaut, *A Study of the Hadro-Production and Weak Decay of Charm Particles in 360 Gev/c π^- and 400 GeV/c pp Interactions* Ph.D. Thesis, Oxford University, (1986).

[25] J. Kirkby, *Review of e^+e^- Reactions in the Energy Range of 3 to 9 GeV.* Proceedings of the 1979 Lepton Photon Conference, Fermilab (1979).

[26] R.M. Edelstein *et. al.*. *The Lead–Liquid Argon Calorimeter for FNAL E653.* Proceedings of the IEEE Conference on Nuclear Science, Washington, D.C. Oct. 1988.

[27] N. Stanton *et.al.*, *Design and Performance of Large Multisampling Drift Chambers for Fermilab Experiment 653.* Proceedings of the XXIII International Conference on High Energy Physics (1986).

[28] James M. Dunlea, *A Study of the X_f and P_t Distributions in the Production of $D^{\pm}$ Charmed Mesons.* Ph.D. Thesis, Ohio State University (1987).

[29] A. Mokhtarani, *Production Characteristics of Neutral and Charged D Mesons in 800 Gev p-Emulsion Interactions* Ph.D. Thesis, University of California at Davis (1988).

[30] G. A. Oleynik, *Inclusive Charged D Meson Production Cross Section Measurements in 800 GeV p-Emulsion Interactions.* Ph.D. Thesis, Ohio State University (1987).

[31] Y-L, Zhang, *A Study of $D^{*\pm}$ Hadro–Production and D^o Semi-Leptonic Decay.* Ph.D. Thesis, Carnegie Mellon University (1989).

[32] T.S. Jaffery, *Resistive Plastic, Proportional Tube, Gas Hadron Calorimeter.* M.S. Thesis, The University of Oklahoma, (1988).

[33] V. Paolone, *Semi–Leptonic Charged D Meson Decays in 800 GeV p–Emulsion Interactions* Ph.D. Thesis, University of California at Davis (1990).

[34] S. Aoki, M.S. Thesis, University of Nagoya (1986).

[35] W. Nichols,Ph.D. Thesis, Carnegie Mellon University (1990)

[36] Kodama *et.al.*, Nucl. Instr. & Meth. **A289** 146 (1990)

[37] D.G. Hitlin, CalTech Pre-print CALT-68-1473 (Nov. 1987) *Weak Decays of Charmed Quarks and τ Leptons.*

[38] M. Aguilar-Benitez *et. al.*, *Particle Properties Data Booklet* (April 1988).

[39] S.P.K. Tavernier, Rep. Prog. Phys. **50** 1439 (1987).

[40] A. Kernan and G.VanDalen, Physics Reports **106** 297 (1984)

[41] P. Weilhammer, CERN-EP/88-08 (Jan. 1988). *Review of Recent Experimental Results on Hadroproduction of Heavy Quarks.*

[42] M.E. Duffy *et. al.*, Phys. Rev. Lett. **55** 1816 (1985).

[43] H. Cobbaert *et. al.*, Phys. Lett. **191B** 456 (1987).

[44] H. Cobbaert *et.al.*, Phys. Lett. **206B** 546 (1988).

[45] M.D. Sokoloff *et. al.*, Phys. Rev. Lett. **57** 3003 (1986).

[46] L. Leuking, Proceedings of the XVth Recontres de Moriond, Les Arcs, France. (1990).

[47] S. Barlag *et. al.*, Z. Phys. C **39** 451 (1988).

[48] R.P. Feynman, Phys. Rev. Lett. **23** 1415 (1969).

[49] R. Ammar *et. al.* Phys. Rev. Lett. **61** 2185 (1988).

[50] M. Aguilar–Benitez *et. al.*, Physics Letters **189B** 476 (1987).

[51] M. Aguilar–Benitez *et. al.*, Z. Phys. C **40** 321 (1988).

[52] M. Aguilar–Benitez *et. al.*, Physics Letters **164B** 404 (1985).

[53] M. Aguilar–Benitez *et. al.*, Physics Letters **161B** 404 (1985).

[54] M. Aguilar–Benitez *et. al.*, Z. Phys. C **36** 559 (1987).

[55] M.E. Duffy *et. al.*, Phys. Rev. Lett. **55** 1816 (1985).

[56] H. Cobbaert *et. al.*, Phys. Lett. **191B** 456 (1987).

[57] H. Cobbaert *et. al.*, Phys. Lett. **206B** 546 (1988).

[58] M.I. Adamovich *et. al.* International Symposium on Heavy Quark Physics, Cornell University, Ithaca,N.Y. (1989).

[59] L.Lyons and D.H. Saxon, Oxford pre-print OUNP-89-1 (1988). *Techniques for the Study of the Lifetimes of Short-Lived Particles.*

[60] J.M. Izen, Slac Pre-print SLAC-PUB-4753 (1988). *Semi Leptonic Charm Decay.* Present at the 1988 Meeting of the Divison of Particles and Fields of the American Physical Society, Storrs, Conn.

[61] J.D. Bjorken, *Mass of Charm and Strange Baryons* (1986)

[62] K. Kodama *et. al. Measurement of the Relative Branching Fraction* $\Gamma(D^o \rightarrow K\mu\nu)/\Gamma(D^o \rightarrow \mu X)$ to be published.

[63] N. Ushida, *et. al.* E653 proposal (1981)

[64] T. Yoshida *et. al.*, Phys. Rev. D **39** 3516 (1989)

[65] B. Dylan **Blonde on Blonde** *Stuck Inside a Mobile with the Memphis Blues Again* (1968).